

---

**Tomographic Imaging: Reconstruction and  
Qualitative Evaluation**

by

Paola Bonetto

Theses Series

**DISI-TH-2001-01**

---

DISI, Università di Genova

v. Dodecaneso 35, 16146 Genova, Italy

<http://www.disi.unige.it/>

**Università degli Studi di Genova**

**Dipartimento di Informatica e  
Scienze dell'Informazione**

**Dottorato di Ricerca in Informatica**

**Ph.D. Thesis in Computer Science**

**Tomographic Imaging: Reconstruction and  
Qualitative Evaluation**

by

Paola Bonetto

December, 2000

**Dottorato di Ricerca in Informatica  
Dipartimento di Informatica e Scienze dell'Informazione  
Università degli Studi di Genova**

DISI, Università di Genova  
via Dodecaneso 35  
I-16146 Genova, Italy  
<http://www.disi.unige.it/>

**Ph.D. Thesis in Computer Science**

Submitted by Paola Bonetto  
Dipartimento di Informatica e Scienze dell'Informazione  
Università di Genova  
[bonetto@disi.unige.it](mailto:bonetto@disi.unige.it)

Date of submission: December 2000

Title: Tomographic Imaging: Reconstruction and Qualitative Evaluation

Advisor: Prof. Mario Bertero  
Dipartimento di Informatica e Scienze dell'Informazione  
Università di Genova  
[bertero@disi.unige.it](mailto:bertero@disi.unige.it)

Ext. Reviewers: Andreas Formiconi  
Dipartimento di Patofisiologia  
Università di Firenze  
[arf@unifi.it](mailto:arf@unifi.it)

Vittorio Murino  
Dipartimento Scientifico e Tecnologico  
Università di Verona  
[murino@sci.univr.it](mailto:murino@sci.univr.it)



Dipartimento di Informatica e Scienze dell'Informazione  
Università degli Studi di Genova

# **Tomographic Imaging: Reconstruction and Qualitative Evaluation**

A dissertation submitted in partial satisfaction  
of the requirements for the degree  
Doctor of Philosophy in Computer Science

by

Paola Bonetto

Supervisor: Prof. Mario Bertero

December 2000

DISI Technical Report 2001-01

## Abstract

Recent advances in medical imaging have permitted to gain deep insight into the structure and the anatomy of organisms as well as into the biological processes and events within human and animal bodies as they occur in vivo. For this reason, medical imaging technologies have rapidly become an essential support for scientific research and, nowadays, represent a fundamental clinical tool for diagnosis, therapy planning, and surgery.

This thesis focuses on tomography. The aim is to investigate the problem of reconstruction without isolating it from the context which tomography belongs to – a medical environment – but rather by specifically targeting the two major interests and requirements imposed by the clinical reality and the current status of medicine: low waiting times for obtaining an image of the organ being scanned and high quality of the images themselves, possibly considering the particular clinical use and the type of information that is being sought.

The first requisite - low computational time - is addressed by developing an efficient mathematical model for the process of data acquisition performed by the tomograph. Reconstruction algorithms can then be used on this model, in order to invert the data acquired by the scanner and quickly compute an accurate estimate of the object being imaged.

The model we propose for SPECT devices is accurate because it compensates for collimator blur. The compensation is fully performed on the transaxial planes and is only approximated in the axial direction. Such an approximation, while not significantly degrading the quality of the reconstructions with respect to fully 3D models, substantially reduces the computational burden of the reconstruction process: we have been able to prove that the total computational cost of an iterative

algorithm on our approximation is in the same order of magnitude of one customized on a 2D projection model, in which no axial collimator blur is considered at all.

In order to perform some numerical tests and validate the accuracy of our formulation, we have customized the model to a state-of-the-art neuro-SPECT scanner, which is supplied with a three-segmented parallel beam collimator. Several reconstruction algorithms based on this customization as well as on “standard” 2D and 3D ones are compared, both in terms of timing requirements and quality of the results.

As concerns the second requisite - high quality of the reconstructions - we have investigated some qualitative methods to evaluate the images. Such methods are based on the idea of simulating clinically relevant tasks, in order to test whether a given reconstruction algorithm produces results that are significant, reliable, and useful from a medical point of view.

We have considered a binary task of lesion detection. More specifically, we have restricted our attention to the case of small tumoral abnormalities in PET images computed by a MAP (Maximum A Posteriori) reconstruction algorithm. With reference to this task definition, we have performed the lesion detection study with both computer and human observers.

The computer observer study was based on the Channelized Hotelling Observer (CHO). We have derived a closed form for expressing its statistics, which is based on a theoretical approximation for the mean and covariance of MAP reconstructions. By applying our model to 2D MAP images, we have been able to show a significant correspondence between our theoretical results and the results obtained by a Monte Carlo study associated with the traditional CHO. The accuracy and low computational cost of our approximation has allowed us to analyze the observer performance over a wide range of operating conditions and parameter settings for the MAP reconstruction algorithm.

The goal of the human observer study was to compare the performance of the MAP and FBP algorithms: the two methods were thus applied to the same set of data under different conditions, namely 2D and 3D, with and without attenuation correction. The images were analyzed by four observers who did not have any previous experience on this task and were supposedly not biased in favor of one approach over the other. The observer evaluations were then analyzed by both an ROC and an LROC study. The results, beyond evidencing the superiority of the MAP approach with respect to the FBP one for the task of lesion detection, also gave us interesting feedback about the general performance of the MAP method and helped us in identifying the direction to take for further optimization of the algorithm.

## Foreword

Over four years ago, right before entering the Ph.D. program, my advisor Prof. Mario Bertero asked me if I was interested in Medical Imaging. I said “Yes, absolutely!”. But, honestly, apart from the fact that I was somehow attracted by both the words “image” and “medical”, I did not know. I intended to take my time and think over that question.

Soon, I realized that that question actually implied another, more “high level” one: “Are you really interested in doing research?” and, more precisely: “Why?”.

It took me all four years of the Ph.D. program to come to the answer. This answer is probably my greatest achievement as a Ph.D. student...

As often happens, I had known that answer for a long time, but I simply had to stumble into it from a different direction. The first time I consciously ‘met’ that answer was in High School, during a class of German Literature. I remember very clearly how my professor, Dr. Schäfer, standing right in front of me and pointing his finger directly to me as if there were just the two of us in the classroom, slowly, very slowly, read the following passage by Gotthold Ephraim Lessing<sup>1</sup>, scanning every single word in a full, severe and solemn tone (but without hiding a provocative, self-satisfied smile under his Bavarian moustache):

*Wenn Gott in seiner Rechten alle Wahrheit, und in seiner Linken den einzigen immer regen **Trieb nach Wahrheit**, obschon mit dem Zusatze, mich immer und ewig zu irren, verschlossen hielte, und spräche zu mir: wähle! Ich fiele ihm mit Demut in seine Linke, und sagte: Vater gib! die reine Wahrheit ist ja doch nur für dich allein!*<sup>2</sup>

It is this *longing* for the answer, the effort that I’ve put towards it for four years - even though, a priori, I might not have reached anything - that I’ve learned to like about doing research.

---

<sup>1</sup> Letter to Hauptpastor Goetze

<sup>2</sup> If God held in its right the entire Truth, and in its left the only always living **strife towards the Truth**, although on the condition always to be mistaken, and spoke to me: choose! I would fall with humility into his left one and say: Father, give! The pure Truth is only for you alone!

My subliminal goal in this thesis, is to share these feelings with whomever attempts to read this manuscript and, in particular, to give my friends and relatives who are not directly involved in research issues the chance to taste what I've learned. I'd like to provide them the opportunity to sneak into one of the many (scientific) problems that are hidden behind everyday reality's façade and that are usually not accessible to the non experts because encoded into a to them inaccessible language.

For this reason, I have inserted an overview section at the beginning of each of the two parts into which this work is organized: these sections are written in a descriptive way and do not require any specific mathematical or medical background to be understood. They are meant to present the issues to which I have devoted four years of my professional life: although they do not directly discuss the solutions and the results I have obtained, I hope that, beside providing an introduction to the following sections, they also achieve my personal goal of arousing the reader's curiosity and having him perceive what I mean by "longing for the answer" and "strife towards the Truth".

While writing these sections, I most of all had my parents in mind since, not only they hardly know what direction has taken the education they have provided to me ever since they decided to enroll me in the *Kindergarten der Deutschen Schule Genua*, but they do not even have the slightest idea of what has led me to take this way. In this sense, these overviews are a sort of dedication to my mother and my father.

I am grateful to my advisor Professor Mario Bertero: he has introduced me to research and to the area of Medical Imaging and he has guided me through the difficult transition from “being a student” to “being a researcher”. This guidance includes a patient and generous understanding on his behalf about my...escaping for over two years and searching for my own way: the experience in the States has been extremely formative and important to me, both from the educational point of view and a personal one. Hence, I have very much at heart to express him my gratitude and my recognition.

Dr. Richard Leahy has been supervising me during the past two years that I have spent as a visiting scholar at the University of Southern California in Los Angeles. He has directed my research with immeasurable care and competence, always anticipating the right advice and encouragement, constantly providing new and stimulating ideas and suggestions that opened up my perspective and vastly added to my knowledge.

Even more than a supervisor he has been to me an example in focusing and well balancing the multitude of aspects that are involved in order to have...”things work out”: being constantly updated and maintaining the right pace to advance towards a goal; keeping high interest, curiosity and confidence as well as providing enthusiasm and motivation in many different ways, up to taking care of the most concrete and material needs as a comfortable working environment and good (social!) communication among co-workers.

A special thanks to Melanie and Cyrus.

Melanie, for her transparency and sincerity, for her constant “researching” and seeking for a deep significance and her struggle to improve upon herself. Her friendship and example mean a lot to me.

Cyrus, for his generosity and for the enthusiasm and the optimism he puts into all he does. And, of course, for his valuable corrections to my English as well as for reading through this entire thesis!

Several other people added vastly to my experience both as a student and researcher and as a ...visiting fellow in a foreign country: each and everyone of them has contributed in its own way to enrich me as a person and has provided me with wonderful memories that I will be always glad to recall and, possibly,...to update! Even though I refrain from mentioning here their names, I heartily thank all of them.

And I truly thank Dr. Schäfer, of course...

# Table of contents

<b>ABSTRACT</b>	<b>2</b>
<b>FOREWORD</b>	<b>5</b>
<b>TABLE OF CONTENTS</b>	<b>8</b>
<b>LIST OF FIGURES</b>	<b>10</b>
<b>1. INTRODUCTION</b>	<b>12</b>
<b>2. IMAGE RECONSTRUCTION</b>	<b>19</b>
<b>2.1. OVERVIEW</b>	<b>19</b>
2.1.1. TOMOGRAPHY	19
2.1.2. DATA ACQUISITION	22
2.1.3. THE PROBLEM OF RECONSTRUCTION	27
<b>2.2. DETERMINISTIC FRAMEWORK</b>	<b>32</b>
2.2.1. FILTERED BACK-PROJECTION	34
<b>2.3. THE 2D+1 MODEL</b>	<b>38</b>
2.3.1. THE SHIFT VARIANT RESPONSE FUNCTION	39
2.3.2. THE DISCRETE CASE	45
2.3.3. THE 2D+1 APPROXIMATION OF THE 3D PROJECTION MODEL	51

2.3.4.	ITERATIVE RECONSTRUCTION	55
2.3.5.	SIMULATIONS AND RESULTS	64
<b>2.4.</b>	<b>STATISTICAL FRAMEWORK</b>	<b>84</b>
2.4.1.	MAXIMUM A POSTERIORI	89
<b>3. IMAGE QUALITY ASSESSMENT</b>		<b>98</b>
<hr/>		
<b>3.1.</b>	<b>OVERVIEW</b>	<b>98</b>
3.1.1.	METHODS TO EVALUATE IMAGE QUALITY	98
3.1.2.	OBSERVERS	106
3.1.3.	PERFORMANCE INDICES	110
<b>3.2.</b>	<b>COMPUTER OBSERVERS</b>	<b>115</b>
3.2.1.	THE CHANNELIZED HOTELLING OBSERVER	118
3.2.2.	SIMULATIONS	122
3.2.3.	A THEORETICAL APPROXIMATION FOR THE CHO STATISTICS	130
3.2.4.	SIMULATIONS	135
<b>3.3.</b>	<b>HUMAN OBSERVERS</b>	<b>145</b>
3.3.1.	THE STUDY	146
3.3.2.	RESULTS AND DISCUSSION	153
<b>CONCLUSION</b>		<b>172</b>
<hr/>		
<b>APPENDIX</b>		<b>175</b>
<hr/>		
<b>REFERENCES</b>		<b>181</b>
<hr/>		

# List of figures

<b>Figure 1: Tomographic devices</b>	<b>20</b>
<b>Figure 2: Difference between Transmission and Emission Computed Tomography</b>	<b>21</b>
<b>Figure 3: Projection of a disk and of a point-like source in 2D as it occurs in SPECT</b>	<b>23</b>
<b>Figure 4: Emission of two photons along the same line in PET and of a single photon in SPECT</b>	<b>24</b>
<b>Figure 5: In SPECT, photons that are not travelling towards the detector...</b>	<b>25</b>
<b>Figure 6: Schematic of an axial cross section through a 2D and a 3D PET scanner</b>	<b>26</b>
<b>Figure 8: Forward Projection of a disk-like source</b>	<b>28</b>
<b>Figure 9: Back Projection</b>	<b>29</b>
<b>Figure 10: 1D projection of a 2D object</b>	<b>33</b>
<b>Figure 11: Illustration of the Fourier Slice Theorem</b>	<b>37</b>
<b>Figure 12: Photons entering a single collimator in the 2D and in the 3D case</b>	<b>40</b>
<b>Figure 13: Bell shape and space variance of the PSF in the 2D and in the 3D</b>	<b>41</b>
<b>Figure 14: Axial shift variance of a point source; The truncation of 2D projections...</b>	<b>42</b>
<b>Figure 15: Definition of the geometrical variables for the Radon Transform</b>	<b>43</b>
<b>Figure 16: Object and Data space</b>	<b>47</b>
<b>Figure 17: Projection of a point-like source with the 3D, 2D and 2D+1 models</b>	<b>52</b>
<b>Figure 18: 3D and 2D projection of a disk of uniform activity</b>	<b>67</b>
<b>Figure 19: Plot of the 13 weights <math>a_1</math> (<math>-6 = 1 = +6</math>) used by the 2D+1 projector</b>	<b>68</b>
<b>Figure 20: Projection of a 56 pixel off-axis voxel</b>	<b>70</b>
<b>Figure 21: Plot of the percentage projection and projection-backprojection error</b>	<b>72</b>
<b>Figure 22: A transaxial section of the phantom is compared with...</b>	<b>77</b>
<b>Figure 23: A sagittal and the respective coronal view of the phantom and...</b>	<b>78</b>
<b>Figure 24: Plot of the RE (in %) of the reconstructions</b>	<b>80</b>
<b>Figure 25: Plot of the RE values (in %) relative to five concentric isocount regions</b>	<b>82</b>
<b>Figure 26: A schematic view of the basic steps involved in the process of image formation</b>	<b>99</b>
<b>Figure 27: Examples of physical phantoms</b>	<b>102</b>
<b>Figure 28: Resolution and Contrast recovery</b>	<b>103</b>
<b>Figure 29: Examples of PET images for a lung study</b>	<b>106</b>
<b>Figure 30: Partitioning of the image set</b>	<b>111</b>
<b>Figure 31: Graphical representation of the concept underlying the definition of ROC curve</b>	<b>113</b>
<b>Figure 32: The main linear observer statistics as defined by the form of matrix K</b>	<b>116</b>
<b>Figure 33: Transformation of an image into the channel space</b>	<b>120</b>

<b>Figure 34: Profiles of three DOG and SQR channels respectively</b>	<b>121</b>
<b>Figure 35: Data set generation for the Monte Carlo study to test the CHO performance</b>	<b>123</b>
<b>Figure 36: AUC values of the CHO with SQR channels</b>	<b>125</b>
<b>Figure 37: AUC values computed by the CHO with DOG channels</b>	<b>126</b>
<b>Figure 38: Plot of the image distribution in the channel space</b>	<b>127</b>
<b>Figure 39: Distribution of the AUC values computed on 150 sets of 100 reconstructions each</b>	<b>129</b>
<b>Figure 40: AUC values as a function of set cardinality</b>	<b>130</b>
<b>Figure 41: The transaxial plane chest phantom used in the simulations</b>	<b>136</b>
<b>Figure 42: The 2D slice of the Hoffman phantom [Hof90] used in the simulations</b>	<b>137</b>
<b>Figure 43: AUC values for the channelized Hotelling observer</b>	<b>140</b>
<b>Figure 44: Surface and contour plot of the channelized Hotelling observer as a function of...</b>	<b>141</b>
<b>Figure 45: Surface and contour plot of the channelized Hotelling observer as a function of...</b>	<b>142</b>
<b>Figure 46: The graphical interface used by the readers for image presentation and evaluation...</b>	<b>150</b>
<b>Figure 47: The graphical interface used by the readers for image presentation and evaluation...</b>	<b>151</b>
<b>Figure 48: Scheme of the pairwise comparisons of the study and the respective results</b>	<b>154</b>
<b>Figure 49: 2D FBP reconstruction without attenuation correction of TN data</b>	<b>160</b>
<b>Figure 50: 2D MAP reconstruction of the same TN data of Figure 49</b>	<b>161</b>
<b>Figure 52: ROC and the LROC curves for MAP and...</b>	<b>165</b>
<b>Figure 53: The complexity of 2D and 3D PET devices has an exponential growth</b>	<b>175</b>
<b>Figure 54: The power of PC processors in terms of MIPS has a linear growth</b>	<b>175</b>
<b>Figure 55: The Graphical User Interface to the MAP reconstruction program</b>	<b>180</b>

# 1. Introduction

Medical Imaging has experienced exciting advances in recent years. New imaging methods can now reflect anatomy, dynamic body functions, and internal biologic changes as they occur in vivo. Advances in imaging and image processing therefore play an expanding role in diagnosis, surgical and radio-therapy: by providing new and better ways to extract information about our bodies, they give medical personnel access to much greater insight into the patient's conditions.

Among the many different imaging modalities, in this thesis, we will consider PET and SPECT, which both belong to the more general class of *Tomography*: tomographic techniques produce an image of the signal (that in this case consists of photons) contained in a slice across the human body. This is in some respects equivalent to cutting off the anatomy above and below the slice that is being visualized.

SPECT and PET both are *nuclear medicine modalities*, in which a radiopharmaceutical is injected into the human body: by detecting the gamma rays emitted in the radioactive decay of the isotope the spatial distribution of the pharmaceutical can be mapped into an image. Modalities in which the radiation source is located within the body are referred to as *emission modes* (ECT, Emission Computed Tomography). In contrast, in *transmission modes* (TCT, Transmission Computed Tomography) the source is external to the patient. Because both SPECT and PET are emission modalities, they are sometimes together referred to as ECAT, Emission Computerized Axial Tomography.

Once data have been acquired it needs to be inverted, or reconstructed, into an image. Further processing can give medical personnel greater insight into functional and anatomical information by emphasizing, measuring, or visualizing important features.

The ultimate goal, the medical interpretation and use of the image, can be the most diverse: comparison of pre- and post- intervention images is useful for treatment verification and growth monitoring or for temporal estimations, e.g., of blood flow; 3D visualization can help at the task of bone modeling and movement estimation as well as in the study of tissue elasticity and, of course, simulation of surgical operations; statistical analysis can provide information about asymmetries in the brain or other organs, for studies concerning controls and schizophrenics, but also diversities between different categories of the population [Heu94, Hol92, Sch94]. For each specific task one or the other imaging technique can turn out to be more suitable and provide better results.

Much of the recent interest in medical imaging is related to the mathematical problems underlying the processes that occur between the moment in which the raw data has been collected by the device and the image is displayed and "used": such problems include reconstruction methods for producing images from raw data, equations that link measurements to quantities of interest, algorithms relative to the processing of the reconstructions, like segmentation, registration of multimodality images and, lastly, data visualization.

In this work, we investigate two such problems, related respectively to two different but mutually dependent phases of the image's "life process": image reconstruction, that is, producing an image from the projections, and lesion detection, as a tool for assessing the quality of the image itself.

As far as image reconstruction is concerned, we restrict our attention to the case of tomographic imaging. In fact, while the final images of different techniques may bear similarities to each other, the technologies involved and, consequently, the mathematical or statistical models used to reconstruct them are rather different, as they reflect the diversities in medical usefulness. A detailed look at various devices with associated mathematical models and algorithms can be found in [Mat96].

From a mathematical point of view, the models that describe this problem are based on an integral equation called *Radon Transform* and the solution corresponds to inverting this formula. Because of the impossibility of giving an exact solution to such problems, special inversion algorithms have to be developed that calculate approximations of the object yielding only estimates of the ideal image (see [Ber98] for an introduction to inverse problems in imaging, or [Her80] for a detailed survey of various tomographic reconstruction methods).

The first major contribution of this thesis concerns a particular SPECT device for brain imaging located at the San Martino Hospital in Genova, Italy: a suitable projector model is formulated and applied to different inversion algorithms, including CG (Coniugate Gradient), EM (Expectation Maximisation) and OS-EM (Ordered Subset EM): we thus obtain various quite accurate and fast reconstruction methods. These have been implemented and their performance compared and the “best” among them is now used on a daily basis by the clinicians of our department.

The second goal of this thesis is to compare the performance of different reconstruction algorithms applied to PET scans. Research has always aimed at increasing the quality of the reconstructions in order to provide more precise information to medical staff. However, “image quality” has been defined in terms of either subjective appearance or generic image characteristics, such as sharpness and contrast – criteria that might not necessarily be consistent with the medical

requirements and that might not reflect the accuracy and reliability of the information that the images provide, or the ease with which they are interpreted by the clinical personnel. A more direct and objective way to measure image quality is in terms of performance in executing clinically relevant tasks. Visual detection and classification, that are among the most important medical diagnostic modalities, can, for instance, be simulated with the specific purpose of measuring how well they can be performed and, thus, obtaining feedback about the quality of the image and the accuracy of the underlying reconstruction algorithm.

Here, we compare the quality of reconstructions of the same data obtained by different schemes, by performing a clinical task oriented study that addresses one of the main uses of PET, namely, the detection of abnormalities in scans of patients with suspected tumors.

These kinds of studies are usually performed by physicians or others who are somewhat familiar with interpreting medical data. However, in order to obtain reliable and statistically significant results, a very large number of images has to be analyzed, which turns out to be an extremely time consuming and expensive task. For this reason, some steps have already been taken towards automating this process: human observers could possibly be replaced by *computer observers*, i.e. models that reliably reproduce and check human performance in investigating the images, which, in our case, would mean detecting known malignancies.

Mathematically, computer observers for the task of lesion detection are discriminant functions to mimic the frequency selectivity of the human visual system. Various models have already been proposed, but, as shown in [Bur95] and [Cha97], they are still unsatisfactory for clinical use and more elaborate models have to be formulated.

An important issue related to both human and computer observers is measuring their performance, because this quantizes, in terms of one or more numerical indices, the quality of the reconstructions. Furthermore, this represents a convenient way to compare the results of a computer with human observer studies and guarantee that the former reproduces and matches well enough with the latter.

In the case of lesion detection, the task of the observer is a binary one - either a lesion is or is not detected. Therefore, results of these studies can be analyzed by using ROC (Receiver Operating Characteristic) curves, which are by far the most commonly used tool for evaluating diagnostic tests [Met86, Met89, Car97].

In this thesis, we present both a computer and a human observer study: the first aims at investigating the problem of a reliable and computationally cheap replacement of human observers at the task of lesion detection. We have considered the Channelized Hotelling Observer (CHO) because this has been shown to perform well with respect to humans. The major characteristic of this model is that it features a set of frequency selective filters that somehow reflect similar properties of the human visual system. We propose a method that drastically reduces the time complexity associated with the computation of the CHO statistic. It is based on a mathematical approximation for the mean and covariance of images reconstructed by a Maximum A Posteriori (MAP) algorithm. Simulations show that the results obtained by our scheme are comparable with those obtained by the “traditional” CHO that, however, required highly time consuming Monte Carlo studies. Hence, based on these conclusions, we have been able to approximate the CHO statistic over an extremely large range of conditions and settings, both related to the reconstruction algorithm and to properties of the lesions. The time required to perform such a study by means of the traditional CHO Observer would reach beyond the limits of feasibility.

The purpose of the human observer study was to test the performance of the MAP reconstruction algorithm compared to other standard algorithms at the task of lesion detection. In fact, the MAP scheme has been developed with the goal of reducing noise, which is the major obstacle in problems of lesion detection [Mum96, Qi98a, Qi98b]. The study was performed on real clinical whole body data and consisted in detecting and locating both benign and malign abnormalities in the lungs. The images were obtained from the data by a MAP algorithm and different variants of FBP (with and without attenuation correction, 2D vs 3D acquisition and reconstruction). We were able to show that, overall, the MAP approach outperforms the FBP one. However, while it features high sensibility – i.e. it is reliable when excluding the presence of a disease if reporting negative results – it does not show as much a high specificity (the reliability with which the presence of a lesion is confirmed when reporting positive answers): steps to improve the algorithm should be taken according to these lines.

The structure of this dissertation reflects that of the project: the first part is devoted to the problem of Image Reconstruction. The two major approaches – deterministic and statistic - are introduced, and algorithms are presented for each of them. Regarding the deterministic framework the Filtered BackProjection (FBP) is described, for this is the most commonly used method in clinical environments and, thus, it represents the reference scheme when considering different reconstruction methods. A major focus is on a projection model, the  $2D+1$ , that we have developed for a specific SPECT scanner, and that we used in conjunction with different inversion algorithms to find a solution of the reconstruction problem. A final section is devoted to the statistical framework: the MAP (Maximum A Posteriori) method is described because this is the one on which the following studies are based.

The second part of the dissertation deals with the problem of qualitative image assessment. As above, the two major approaches – computer and human observers – are introduced and methods and examples are described for each of them: the first section deals with the CHO Computer Observer and the approximation we have developed, whereas the following section is devoted to Human Observers. A description of the simulations that we have performed for each case is also included: these analyses are based on the MAP algorithm mentioned above, and the FBP approach is also considered as the reference method on which comparisons between different reconstruction approaches are based.

## 2. Image reconstruction

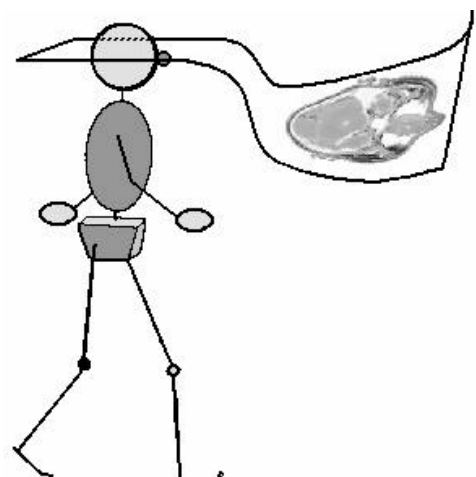
This chapter is devoted to the problem of image reconstruction. An overview of the topic is given in the first section: here, any mathematical aspect and technical detail is omitted and the description is kept on general terms in order to provide an easily understandable background, also accessible to the non expert reader.

The following sections deal with the two major approaches to the problem of reconstruction, namely, a deterministic and a statistical one, For each case a particular method is presented. We also introduce the 2D+1 model that we have developed for a specific SPECT device, and describe the related simulations and experimental studies that have been performed.

### 2.1. Overview

#### 2.1.1. Tomography

The term tomography is derived from Greek (*tomos*, section and *graphia*, -graphy): it refers to the class of devices that produce two dimensional cross-sectional images of three dimensional objects, i.e. images of a slice across a certain depth within a body. This form of imaging is in some respects equivalent to cutting off the anatomy immediately above and below the slice.



## Imaging methods

The different tomographic devices can be divided into two global categories: anatomical and functional. The former depicts primarily *morphology*, and includes X-ray, CAT or CT (Computed (Axial) Tomography), MRI (Magnetic Resonance Imaging), and US (Ultrasound). The latter depicts primarily information on the *metabolism* of the underlying anatomy, and includes fMRI (functional MRI) SPECT (Single Photon Emission Computed Tomography) and PET (Positron Emission Tomography). These kinds of imaging methods represent an important aid in evaluating the appropriateness and efficacy of therapies, as has been for Parkinson's and Alzheimer's diseases, and in investigating the basis of major medical and social health problems including the mental disorders of depression, schizophrenia, osteoporosis, arteriosclerosis, drug abuse, and craving.



Figure 1: Tomographic devices. a) the CERASPECT used at the San Martino Hospital in Genova, Italy, for brain scans. b) the MicroPET scanner for small animals located at the Crump Institute, University of California at Los Angeles.

## Instrumentation

The modalities we will consider in this thesis are PET and SPECT, which both belong to the nuclear medicine imaging modalities. Here, a radiopharmaceutical tracer – i.e. a harmless chemical tracer, often targeted for a particular organ - is injected into the human (or animal) body: by decaying, its isotopes emit gamma rays that are subsequently detected by the device; these data needs to be appropriately processed, so that the spatial distribution of the pharmaceutical tracer can be mapped into an image.

PET and SPECT belong to the class of *ECT (Emission Computed Tomography)* devices, in which the radiation source is located within the body (Figure 2). The photons emitted by the radionuclide that labels the injected compounds are attenuated by the amount of material between the source itself and the detector; location and intensity of the source, and attenuation between source and body edge are unknown. In contrast, in TCT (Transmission Computed Tomography, e.g. X-ray radiography) the source is external to the patient and, hence, its location is known. TCT and ECT have different objectives and therefore use different instruments and mathematical methods for processing the data: while ECT describes the location and intensity of sources of emitted photons, TCT seeks to determine the distribution of a linear attenuation constant.

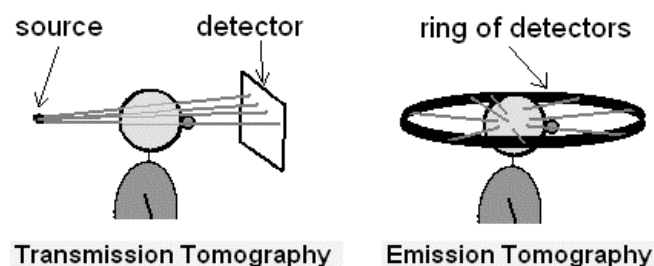


Figure 2: Difference between Transmission and Emission Computed Tomography.

## **Clinical use**

One of the major topics of interest in the area of ECT imaging is the exploration of the activity of the brain when it is challenged with sensory stimulation or mental processing tasks. For instance, the use of PET and SPECT showing the location in the brain of increases in blood volume and blood oxygenation during brain activation, and the to study the quantitative changes in metabolism while processing specific tasks (e.g. verbal, motion, visual) are main topics.

PET technology is also becoming a popular and reliable tool for the detection of small cancer lesions. The concentration of the short-lived radioactive blood sugar-type molecules that are injected into the patient's body and that mingle with different tissues varies by how readily the molecules are taken up by cells. Tumors need an extremely high amounts of sugar, in the form of glucose, to keep up with their fast growth and, thus, show up as abnormally high spots – an accumulation of radiopharmaceutical - on a PET scan.

In contrast, CAT scans use X-rays instead of photons and, thus, although they reach finer resolution levels than even the latest generation of PET scanners, they can not detect metabolic differences between healthy cells and cancerous cells that might signal the presence of small tumors.

### **2.1.2. Data acquisition**

The term *reconstruction* refers to the processing of the data acquired by the tomographic device, in order to reconstruct an image representing a specific slice of the body being analyzed. To understand how this can be performed, it is necessary to describe the way data is acquired and stored.

## Method

As already mentioned above, the body or organ to be imaged is injected by a radiopharmaceutical tracer that emits gamma rays randomly in all directions. These rays are collected by detectors that are part of the imaging device – more specifically, they are part of an instrument called *gamma camera*. The detectors may be arranged on a ring, in the center of which lies the organ, or on (a pair of) planes or ring segments that rotate around the body. In either case, the camera collects data at several interval angles so that values collected at each angle correspond to the number of gamma counts detected in one specific direction.

A set of counts corresponding to a single angle is called a *projection*, whereas the set of all values, that is, the matrix of the counts relative to all interval angles is referred to as the *sinogram*. These concepts are pictured in Figure 3 for the case of a SPECT device.

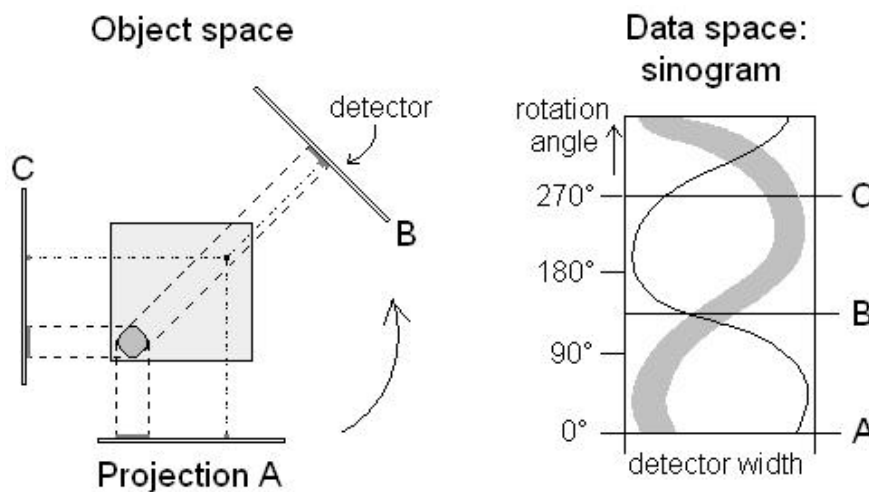


Figure 3: Projection of a disk and of a point-like source in 2D as it occurs in SPECT. Because of the rotation of the camera around the field of view during data acquisition and because both shapes are located off center, the set of projections over all angles stored in the sinogram features two sinusoidal curves.

## PET and SPECT

The major difference between PET and SPECT relies on the different tracers that are used: radionuclides used for PET imaging emit a positron which, when annihilated by electrons of the medium, produces two photons traveling along the same line, but in opposite directions, while those used for SPECT emit a single photon (Figure 4).

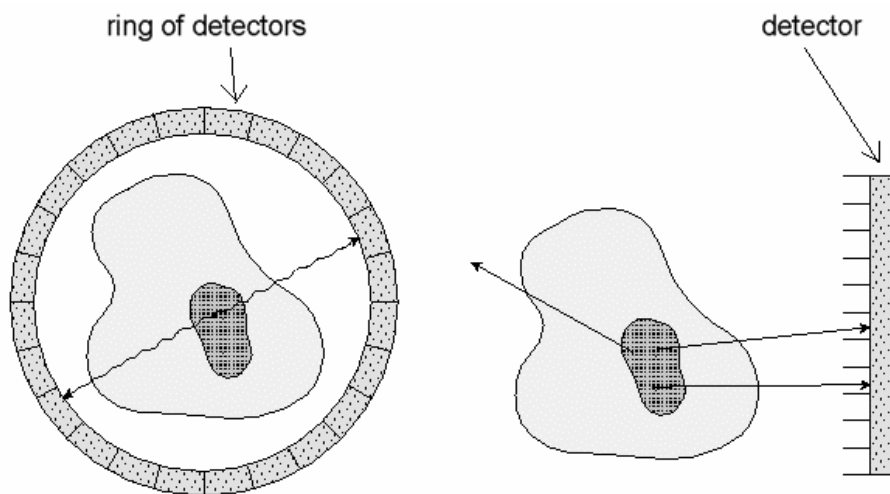


Figure 4: Emission of two photons along the same line in PET (left) and of a single photon in SPECT (right).

Thus, PET devices have each detector operating in coincidence with other detectors across from it: when two photons are recorded simultaneously by a pair of detectors, the collision that gave rise to them must have occurred somewhere along the line connecting the detectors. The total number of such events measured by a pair of detectors will be proportional to the total number of emissions that occurred along the line joining the detectors, and thus to the tracer density there. By surrounding the patient with a ring of detectors – along with the associated photon-coincidence electronics – a PET system can simultaneously measure the projection of the distribution along the many lines between all pairs of detectors.

Because only a single photon is emitted from the radionuclides, in SPECT collimation is not naturally achieved and a special lens known as a collimator is used to allow only those gamma rays to enter that are perpendicular to the plane of the camera. The total number of photons collected at a single element in the camera is proportional to the total number of radioactive nuclei, and hence tracer density, integrated along the line normal to the camera. By rotating the camera around the patient and collecting data at different angles of view, a complete set of parallel projections of the tracer distribution can be measured. The use of a collimator results in a tremendous decrease in detection efficiency as compared to PET. The resulting useful resolution (about 7mm) for SPECT is inferior to PET resolutions by a factor of 2 or 3.

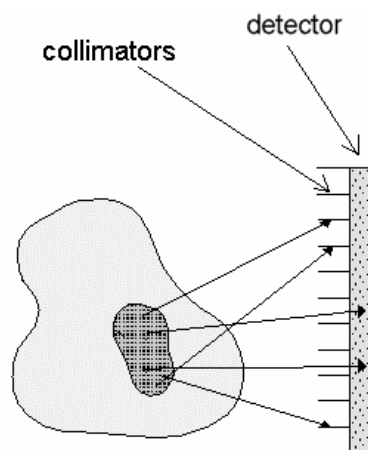


Figure 5: In SPECT, photons that are not travelling towards the detector on an orthogonal direction to it are stopped by the collimators.

### **2D vs. 3D acquisition modality**

Modern tomographic devices are usually equipped with multiple rings of detectors, so that data can be simultaneously acquired for different planes.

In SPECT imaging, because of the effect of the collimators, photons are collected simultaneously, yet separately by each single ring.

In contrast, multiple ring PET devices can operate in either 2D or 3D modality. In the first case, the rings are separated by the *septa* that stop pairs of photons traveling between rings: the coincidence events are collected only between pairs of detectors in the same ring. For each angle, the data are sets of unidimensional projections related to individual bidimensional slices of the organ: the image can be reconstructed as a pile of 2D sections.

In 3D modality PET devices operate with retracted septa. Thus, also coincidence photons traveling between planes can be detected. For each angle, the data consists of bidimensional projections related to the entire 3D organ as a whole. As they are not separated, the full 3D source distribution must be reconstructed all at once: the reconstruction problem must be treated in 3D.

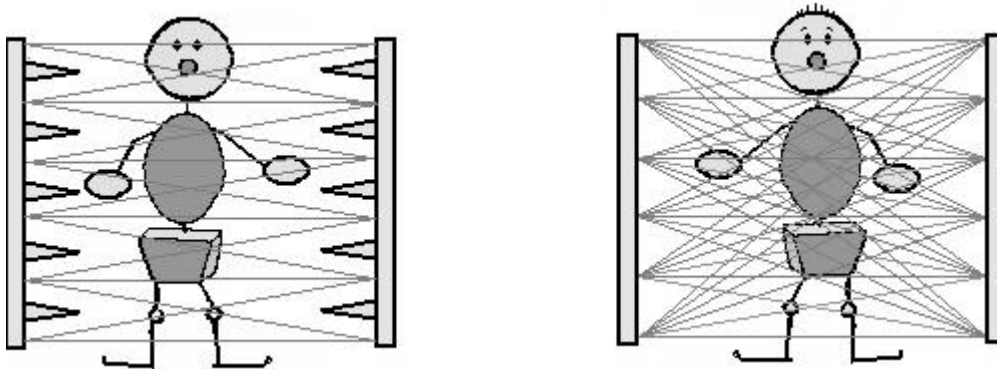


Figure 6: Schematic of an axial cross section through a 2D (left) and a 3D (right) PET scanner. The septa in the 2D scanner stop out-of-plane photons, while the 3D scanner detects these events as additional data.

In summary, the process of data acquisition is a transition from the *object space* – namely, the 3D reality of the body or organ to be imaged – into the *data space*, i.e. the projections of the object detected by the device as a matrix of counts and collected into a single data entity known as a sinogram. The reconstruction process implemented by a computer algorithm is a transition from the data space into the image space, i.e. into a software representation of the initial object.

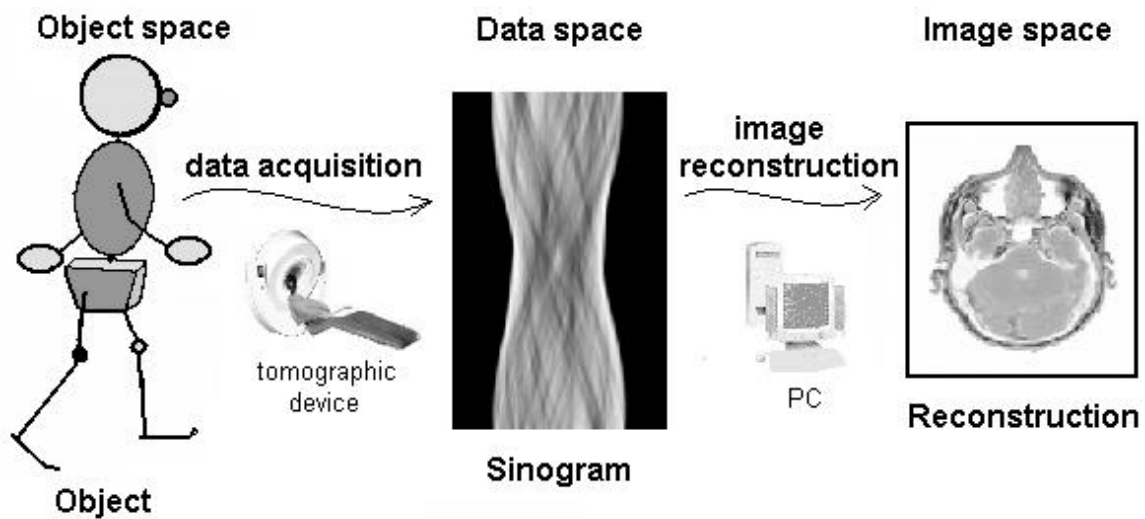


Figure 7: The process of data acquisition and image formation

In the 2D case, the problem is to reconstruct 2D sections of the object from a set of 1D projections at given angles. Similarly, in the 3D case, the problem consists of reconstructing a 3D object from a set of 2D projections at given angles.

### 2.1.3. The problem of reconstruction

#### Backprojection

A basic concept related to image reconstruction is the *backprojecton* of the data. Backprojection can be roughly thought of as the inversion of the process involved during image formation, when the anatomy of the object is projected onto the gamma camera of the scanner. While the projection itself takes place physically within the device and involves a physical object injected with a tracer, the backprojection is a “virtual” process, normally performed by software computations that invert the data into the image space leading to an estimate of the organ that has been scanned.

The process of forward and back projecting the data can be best described by means of an example. For simplicity, let's consider the 2D case, in which a single plane of the organ is involved. Suppose that the object to be reconstructed consists of a single point source – in terms of image, this can be thought of as a single pixel. The projections will have a “peak” shape, with the peak in a varying position along the projection line, depending on the projection angle.

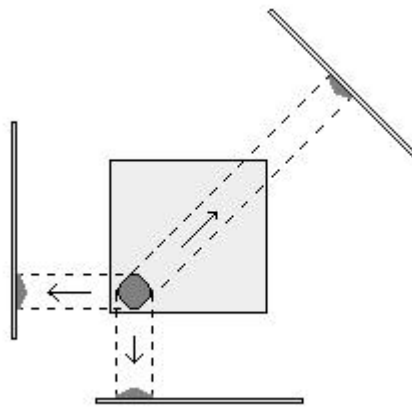


Figure 8: Forward Projection of a disk-like source. A projection is shown for three different angles.

During backprojection, each measured projection value is “spread back”, i.e. added to every grid location of the reconstructed source distribution that is viewed by the corresponding detector element. In the case of a point source that gave rise to “peak” shaped projections, each single peak (corresponding to single projection angles) is “spread back” into the image space in the form of a line passing through the location of the initial point source. By combining all backprojections relative to all angles, an estimate of the initial object is obtained: the spot where all lines intersect corresponds to the location of the initial point source.

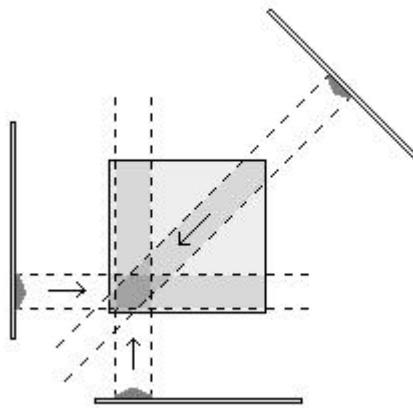


Figure 9: Back Projection. The data collected for a disk-like source (see Figure 8) are projected back into the image space. The process is shown for three different angles.

It is to be noted, however, that the result of a single backprojection over all angles does usually not represent an acceptable reconstruction of the image and cannot be taken as “the final” solution. The reasons for this, along with physical descriptions and mathematical models, are largely discussed in the literature (see for instance [Ber98, Her79, Her80]) and will be summarized in later chapters of this thesis. For the purpose of this introductory overview, it is sufficient to consider that current reconstruction algorithms involve further processing besides a single backprojection, both in the data and in the image space; they are often based on filtering procedures or iterative repeating of both back and forward projection steps.

### **Approaches to reconstruction**

The large variety of reconstruction methods can be approximately grouped into two general approaches: deterministic and probabilistic.

In the *deterministic approach*, the object to be reconstructed is assumed to be deterministic, i.e. it is supposed to lead to exactly the same data when scanned at different times.

The solution can be found by direct inversion of the image transform, or, alternatively, by iterating towards it in a progressive way, for instance by repeatedly minimizing an appropriately defined error. In such an iterative approach, one could start for instance with an estimate of the object to be reconstructed, which may be a uniform image; then simulate (by software computations) the process of projection, as it is performed by the imaging device; compare the result with the data obtained by the device itself and thus compute an error. By repeating these steps sequentially, it is possible to approach the solution as the result of an iterative procedure, whereby a new estimate of the object is calculated at each iteration by back-projecting the error term and subtracting it from the current estimate. The iterations are carried out until the error converges to a minimal value, which corresponds to *choosing the solution as the one, among all estimates that minimizes the error.*

In the *probabilistic approach*, the projection data are assumed to be affected by variation or noise, which might be due to the random nature of the radioactive decay of the isotopes of the tracer. This means that each set of projection measurements is different every time, even for a given, fixed object.

In the probabilistic framework, the estimate of the object is found by maximizing a certain probability of interest. For instance, the solution could be defined as *the estimate, among all possible estimates of the object, that maximizes the probability that its projection equals the data obtained by the device.* Also in the statistical approach, iterative methods can be used to compute the result.

In some cases, additional information about the source is available. For example, one might know some statistical properties of the noise, or some features of the anatomy to be represented as an image, or the nature of the tracer distribution. In the probabilistic framework, this kind of *a priori* information can be included in the formulation of the problem and can help improve the reliability of the solution,

making it less sensitive to perturbations in the data. Probabilistic reconstruction methods that take *a priori* information into account are called *Bayesian methods*.

In the remainder of this chapter, we will gain deeper insight into a few reconstruction algorithms: we will derive their mathematical formulation and discuss their use and performance, including some examples and case studies. The following schemes will be considered:

The **Filtered BackProjection (FBP)** can be seen as the reference algorithm because of its simple mathematical formulation and its straightforward implementation. It is currently the most popular algorithm in clinical environments, due to its low computational costs.

The **2D+1** method represents one of the major contributions of this thesis. It was developed for the CERASPECT at the San Martino Hospital in Genova, Italy. Its main feature is that it approximates 3D reconstructions with a computational cost (both temporal and spatial) equivalent to that of a 2D method.

As is the case of FBP, the 2D+1 scheme belongs to the deterministic framework.

The **Maximum a Posteriori (MAP)** is a Bayesian method that allows us to model the physical and statistical properties of both the observed data and the detection process. Its mathematical formulation will be derived for the case of PET data.

In the second part of the thesis, we will evaluate the performance of this method through qualitative studies based on one of the currently major clinical uses of PET images: hot tumor lesion detection.

## Deterministic framework

In this section, we will first provide some preliminary notation used throughout the thesis, along with a basic mathematical formulation that models the process of data acquisition and image formation from a deterministic point of view. Then, we will describe two techniques of reconstruction that belong to a deterministic class of algorithms, in that they do not take into account the random nature of the noise contained in the data.

### Mathematical forward projection model

The basic problem of tomography is to reconstruct a 3D image (respectively 2D section) from a set of 2D (respectively 1D) projections at given angles. Thus, we first need to mathematically express the relationship between the emission source and the data.

Let us denote by  $f$  the 3D source of intensity to be reconstructed and by  $f(z)$  its  $z$ -th bidimensional plane<sup>3</sup>. Vector  $g$  represents the data; more precisely,  $g(\Phi, \bullet, z)$  is the 1D projection line at angle  $\Phi$  on plane  $z$ , and  $g(\Phi, s, z)$  is the line integral of the image intensity  $f(z)$  along a line  $l$  that is at distance  $s$  from the origin and at angle  $\Phi$  off the  $x$ -axis:

$$g(\Phi, s, z) = \int_l f(x, y, z) dl \quad (1)$$

These concepts are graphically represented in Figure 10.

---

<sup>3</sup> For notational convenience, in this section - describing a deterministic context -  $f$  and  $g$  denote deterministic quantities, whereas in the rest of the thesis they will be treated as random quantities.

As all points  $(x,y)$  on this line satisfy the equation

$$s = x \cos(\Phi) + y \sin(\Phi) \quad (2)$$

$g(\Phi, s, z)$  can be rewritten as

$$g(\Phi, s, z) = \iint f(x, y, z) \delta(s - x \cos(\Phi) - y \sin(\Phi)) dx dy \quad (3)$$

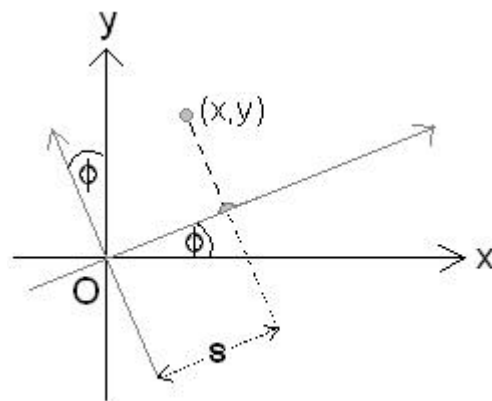


Figure 10: 1D projection of a 2D object.

The collection of  $g(\Phi, s, z)$  at all angles is termed the *Radon Transform* of image  $f(x, y, z)$  and the solution of equation (3) is unique for a given  $f$ . It has been given in a number of mathematically equivalent forms, the first of which was due to Radon [Rad17]. In two dimensions the Radon Transform is identical to the X-ray Transform [Sol76].

Note that, due to the cylindrical symmetry of the sampling geometry and to the consequent translational invariance along the  $z$  direction, the above double integral is independent of the axial variable  $z$ , and, thus, the mapping of the object to the data is done in a “plane by plane” way; the 3D model of equation (3) can equivalently be thought of as a stacking up of 2D mappings performed on every single transaxial plane:

$$g(\Phi, s) = \iint f(x, y) \delta(s - x \cos(\Phi) - y \sin(\Phi)) dx dy \quad (4)$$

When developing a model for the mapping of the object space into the data space, there are several fundamental issues that have to be considered, such as the system response, the geometric response of the collimators in the case of SPECT imaging, the scatter of photons and the attenuation factors due to the attenuating tissues of the organ that is being examined. Therefore, many variants and extensions of the Radon Transform kernel have been proposed – like the Blurred Radon Transform [Boc99] or the Attenuated Radon Transform [Gul96] – to derive a suitable model that takes into account the features of the actual experimental conditions and the requirements of the particular working context, in addition to numerical aspects involved in the inversion of the Radon Transform [Bud77, Kne89, Tow92].

## **Filtered Back-Projection**

Now that the basic mathematical notation has been introduced, we can move on to elucidate the idea that lies behind one of the most popular schemes for the reconstruction of tomographic images: the Filtered Back-Projection (FBP). For notational simplicity, we will restrict the attention to the bidimensional case only.

The forward projection model of equation (4) can be written in its discrete form as

$$\mathbf{g}_{Fs} = \sum_{ij} A_{Fs,ij} \mathbf{f}_{ij} \quad (5)$$

where  $\mathbf{g}_{Fs}$  represents the projection measurements,  $A_{\Phi_s,ij}$  are the elements of the forward transformation matrix  $\mathbf{A}_{\Phi_s}$  that maps the object space into the data space and  $\mathbf{f}_{ij}$  are the pixels into which the image space  $\mathbf{f}$  is discretized.

On one hand, the reconstruction problem naturally involves inverting matrix  $\mathbf{A}$  to obtain an estimate  $\hat{\mathbf{f}}$  of the original source distribution  $\mathbf{f}$ , i.e.:

$$\hat{\mathbf{f}} = \mathbf{A}^{-1} \mathbf{g} \quad (6)$$

However, the forward transformation matrixes are usually singular: for a given set of projections  $\mathbf{g}$  there may be many or no solutions, and the inverse  $\mathbf{A}^{-1}$  may not exist at all.

On the other hand, the reconstruction can also be naturally viewed as an inversion, in the sense of “the opposite process”, of the forward projection: each measured projection value is added to every grid location of the reconstructed source distribution that is viewed by that detector element. Mathematically this can be expressed in summation form as

$$\hat{\mathbf{f}}_{ij} = \sum_{sF} A_{sF,ij}^{-1} \mathbf{g}_{sF} \quad (7)$$

and in vector form as

$$\hat{\mathbf{f}} = \mathbf{A}^T \mathbf{g} \quad (8)$$

where  $\mathbf{A}^T$  is the transpose of matrix  $\mathbf{A}$  and, of course,  $\mathbf{A}^T \neq \mathbf{A}^{-1}$ .

It is interesting to note that, while the Radon transform integrates over all points in a straight line, the backprojection, as expressed by equation (8), integrates over all straight lines through a point. This (combined with the fact that the projection angles used are inevitably finite in number) is the reason why the estimate  $\hat{f}$  obtained by the back-projection procedure alone is a star-like blurring of the original distribution  $f$ . To correct the blurring, the data are usually filtered with a ramp function in the frequency domain before being back-projected. The ramp filter can also be modified by being rolled at high frequencies, in order to avoid excessive amplification of the high frequencies values, where signal-to-noise is low.

The final two-step scheme, namely low-pass filtering followed by backprojection of the data, is known as *Filtered BackProjection (FBP)*. It originated from work in a number of fields, including radio astronomy [Brac67] and electron microscopy [Ram71]. A similar approach, modified to incorporate divergent as opposed to parallel projections, is also used in X-ray computer-assisted tomography [Her71, Her77, Pet77]. In PET, it is currently the most commonly used method in clinics and, therefore, it will be taken here as the reference method with which to compare the more sophisticated techniques that we will describe later in this thesis.

Before concluding, it is worth mentioning that the FBP is often introduced from a different point of view, namely, by considering the underlying relationship between the Radon and the Fourier Transforms: the Fourier Slice Theorem is the basic result that is used in FBP as well as other practical inversion methods [Kak88]. It states that the 1D Fourier Transform of the parallel projection at angle  $\phi$  is equal to the 2D Fourier transform evaluated along the line through the origin in the direction  $\phi + \pi$ . These concepts are illustrated in Figure 11 and a mathematical discussion can be found for instance in [Ber98] and [Lea99CT].

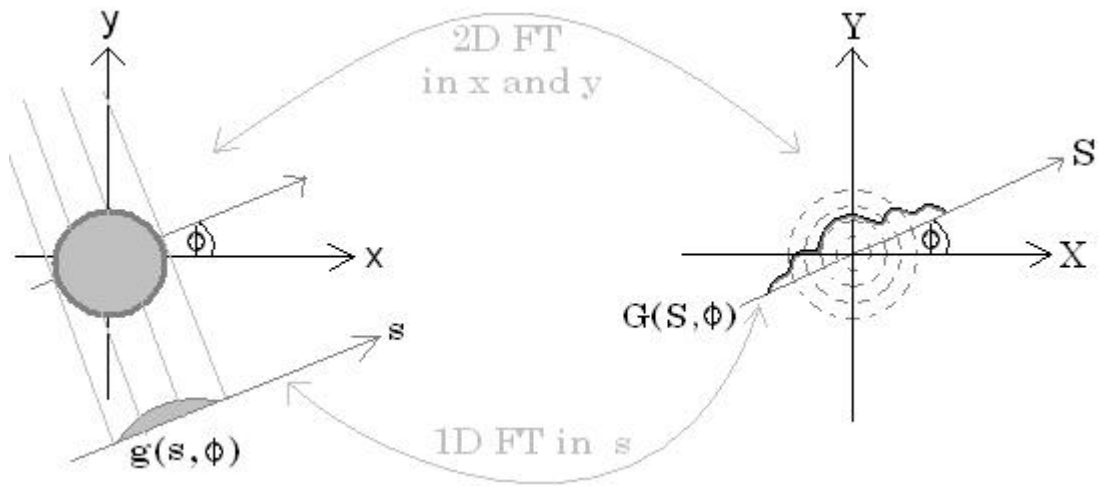


Figure 11: Illustration of the Fourier Slice Theorem. The 2D image on the left is projected at angle  $\phi$  to produce the 1D projection  $g(s, \phi)$ . The 1D Fourier Transform  $G(S, \phi)$  of this projection is equal to the 2D image Fourier Transform  $F(X, Y)$  along the radial line at angle  $\phi$ .

## The 2D+1 model

The straightforwardness and simplicity of the FBP approach described above comes at the cost of poor modeling of the imaging system: in addition to the fact that there is no explicit modeling of noise and other degrading factors, such as scatter and attenuation, the line-integral on which the scheme is based is only approximate. The kernel used for the filtering is the same for all projection values, i.e. it is *shift-invariant*: any translation of the tracer distribution results in a corresponding translation of the projection data. Due to the sensitivity variations within a Line Of Response (LOR) and to differing LOR cross sections<sup>4</sup>, shift-invariance is only approximately satisfied.

These limitations of the FBP are addressed in this section. A more sophisticated model will be derived for the specific case of SPECT data that accounts for collimation blur [Boc99]. The method will be first developed for the bidimensional case and then extended to the 3D. In the latter case, an approximation will be presented that exploits the cylindrical symmetry of the sampling geometry and the consequent invariance along the  $z$  direction, thus leading to a model with a spatial complexity is equivalent to that of a 2D one. Finally, we will show how different reconstruction algorithms can take advantage of the approximated formulation,

---

<sup>4</sup> Most multiple ring PET devices are equipped with septa, to function in 2D mode, that allow not only radiation lying on a plane to reach the detectors, but also radiation that moves between two adjacent rings. LORs within the same plane are called direct plane LORs, whereas LORs between adjacent rings are referred to as cross plane LORs. The angle between the two kind of LORs is small and can be ignored: the cross plane LORs are treated as if they were actually parallel to the plane and lied in a transverse plane located between the two adjacent ones. Thus, a PET tomograph equipped with  $n$  rings of detectors can virtually acquire  $2n-1$  sinograms i.e.  $n$  direct and  $n-1$  cross plane. Such a discussion does not apply to the case of SPECT imaging since here collimators already stop those photons that are not traveling orthogonally to the acquisition plane.

achieving high image quality with the computational complexity in the order of standard 2D algorithms.

## **The shift variant response function**

### **Rationale**

The main issue addressed in this work is the resolution of gamma rays collimation, a typical problem in SPECT<sup>5</sup>.

The geometrical parameters characterizing a collimator are the result of a trade-off between spatial resolution and sensitivity. The purpose of the collimator is to allow only that radiation to reach the detectors, that is perpendicular to the detectors themselves. In this way, during the data inversion process, the emission location of all photons hitting a given element of the camera can be assumed to be somewhere on the line orthogonal to the camera bin. However, in order to allow a statistically sufficient number of counts to be collected, the geometry of the collimator is such that in practice not only a single straight beam, but a cone of photons (a fan on each single projection plane) will enter the camera, with a tolerance that is usually of about 5° (Figure 12).

---

<sup>5</sup> In the context of the deterministic approaches we will neglect the effects of attenuation and scatter that occur during data acquisition. These can be compensated by preprocessing of the data and/or postprocessing of the reconstruction.

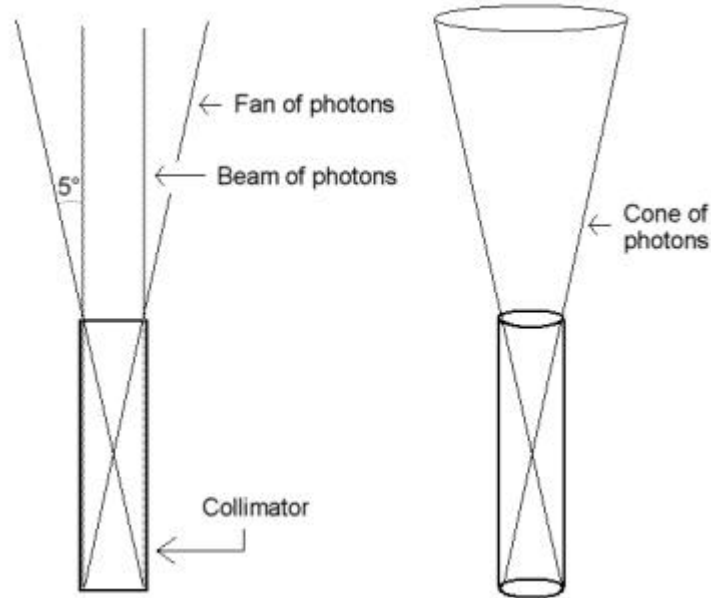


Figure 12: Photons entering a single collimator in the 2D (left) and in the 3D case (right).

From a mathematical point of view, this is best represented by the so called *Point Spread Function* (PSF). The PSF describes the projection of a point source on the Gamma camera; alternatively, it can also be seen as the probability that a photon emitted at a given point source hits some detector element of the camera. The PSF has a bell shape, with a width that varies as a function of the point source location on the transaxial plane. The width variation can be assumed to be continuous with respect to the movement of the source in the field of view – discontinuities, that might be due to geometrical details of the collimator, such as hole shape and hole array structure, can be neglected for the purpose of this discussion. The concept of space variance of the PSF, with respect to a transaxial plane, is depicted in Figure 13.

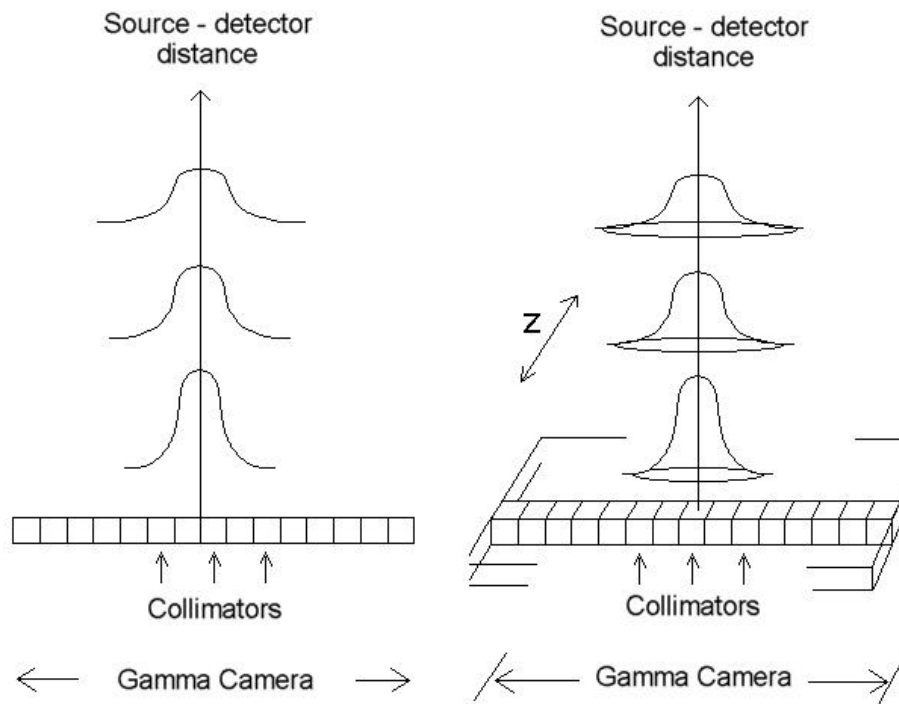


Figure 13: Bell shape and space variance of the PSF in the 2D (left) and in the 3D (right).

By contrast, due to the cylindrical symmetry of the camera, the width variation of the PSF does not depend on the axial coordinate of the source location, but only on its  $(x,y)$  position: in other words, it is axially shift-invariant<sup>6</sup>.

---

<sup>6</sup> Since the second part of this thesis will deal with PET imaging, rather than SPECT, we add here a note about the axial shift variance in the case of PET: when the  $z$  extent of the object exceeds the  $z$  extent of the detector matrix, the three-dimensional data set acquired by a multiring PET tomograph (with retracted septa, in order to also acquire cross plane LORs) does not satisfy the condition of shift invariance; this can be seen by considering a single point concentration of tracer: when the point is located at the axial center of the tomograph, more pairs of annihilation photons are detected than when the same point is axially displaced to one of the outer slices (Figure 14a). Thus, the same tracer concentration «appears» to be greater when imaged at the center of the field of view than when imaged at the edge. The greater the number of ring difference the multiring PET scanner can work with, the more enhanced this effect results (Figure 14b).

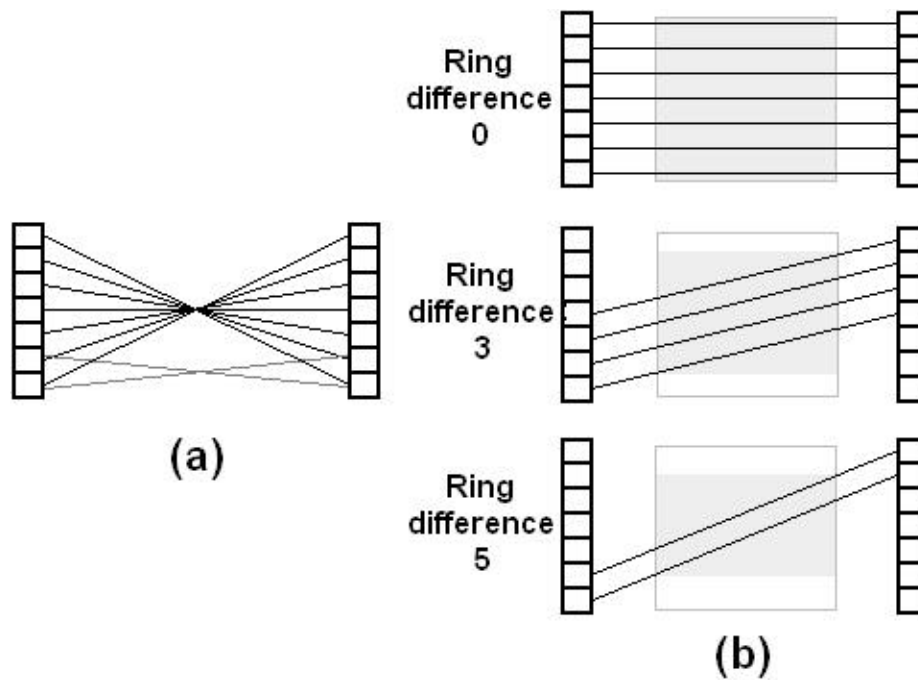


Figure 14: a) Axial shift variance of a point source in the case of PET imaging; b) The truncation of 2D projections with increasing ring difference.

### The 3D continuous Blurred Radon Transform

In mathematical terms the Point Spread Function is reliably well modeled by a Gaussian function with Full Width at Half Maximum (FWHM) varying with the distance of the source from the camera. Thus, we can rewrite the Radon Transform introduced in section 0, by replacing the kernel with a suitable PSF that accounts for collimator blur. Hence, Eq.(3), that we report here for convenience,

$$g(\Phi, s, z) = \iint f(x, y, z) \delta(s - x \cos(\Phi) - y \sin(\Phi)) dx dy$$

becomes

$$g(\Phi, s, z) = \iiint_{3D} f(x, y, z') E(s - x \cos(\Phi) - y \sin(\Phi), -x \sin(\Phi) + y \cos(\Phi), z - z') dx dy dz'$$

to which we will refer as the *3D Blurred Radon Transform*. To simplify the notation, we define  $\mathbf{x} = (x, y)$ ,  $\mathbf{q} = (\cos\Phi, \sin\Phi)$ , from which follows  $\hat{\mathbf{q}} = (-\sin\Phi, \cos\Phi)$ , and  $t = \mathbf{x} \cdot \hat{\mathbf{q}}$  which represents the distance between the source and the detector. Thus, we can write the equation above as

$$g(\Phi, s, z) = \iiint_{3D} f(\mathbf{x}, z') E(s - \mathbf{x} \cdot \mathbf{q}, x \cdot \hat{\mathbf{q}}, z - z') d\mathbf{x} dz' \quad (9)$$

Figure 10 is reposed here in an “updated version” (Figure 15), which includes the notation just introduced, in order to better illustrate the geometrical meaning of these definitions.

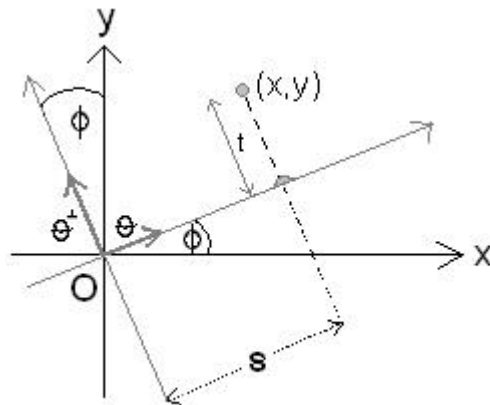


Figure 15: Definition of the geometrical variables for the Radon Transform.

There are three fundamental differences between the integration kernel of the “standard” 3D Radon Transform (3) and its blurred version counterpart (9):

It is no longer an impulse function

It is a function of two variables,  $s$  and  $z$ , on the projection plane

It also depends on the source-detector distance  $t$ .

## The 2D continuous Blurred Radon Transform

In section 0, it was pointed out that, due to the independence of the Radon Transform integral on the variable  $z$ , equation (3) describes at the same time both a 3D and a 2D model. The simpler formula, referring to a single plane and given by equation (4), could be trivially derived; viceversa, the 3D case could be obtained from the 2D one by simply stacking up all bidimensional planes.

In the context of the Blurred Radon Transform, the 2D and the 3D models differ from each other. As a matter of fact, a 2D version cannot by definition include components along the  $z$  direction, so that the axial collimator blur modeled in the 3D will necessarily have to be neglected in the 2D formulation; only the blurring occurring on individual transaxial planes can be considered. As a result, a stacking up of 2D planes will not be equivalent to a full 3D Blurred Radon Transform, or, viceversa, the fully 3D data cannot be separated into a set of parallel contiguous and independent 2D slices.

The mathematical expression we will hereafter refer to with the term *2D Blurred Radon Transform* is

$$g(\Phi, s, z) = \iint_{2D} f(\mathbf{x}, z) E(s - \mathbf{x} \cdot \mathbf{q}, \mathbf{x} \cdot \mathbf{q}^\perp) d\mathbf{x} \quad (10)$$

from which the expression for a single plane can be obtained as:

$$g(\Phi, s) = \iint_{2D} f(\mathbf{x}) E(s - \mathbf{x} \cdot \mathbf{q}, \mathbf{x} \cdot \mathbf{q}^\perp) d\mathbf{x} \quad (11)$$

The Radon Transform kernels introduced so far are summarized in Table 1.

The choice between 2D and a fully 3D Blurred Radon Transform presents a tradeoff between resolution and computational complexity: the inversion of equation (10) involves less computational burden than the 3D version [For97]. However, the spatial extent of  $E(s, t, z)$  along the variable  $z$  is comparable to the extent in the

variable  $s$ . Consequently, the 2D form ignores valuable information that, in the contrary, is well modeled by the 3D Transform.

	3D	2D (both for multiple or single plane)
“Standard” Radon Transform	$d(s - \mathbf{x} \cdot \mathbf{q})$ (3)	$d(s - \mathbf{x} \cdot \mathbf{q})$ (3)
Blurred Radon Transform	$E_{3D}(s - \mathbf{x} \cdot \mathbf{q}, \mathbf{x} \cdot \mathbf{q}^\perp, z)$ (9)	$E_{2D}(s - \mathbf{x} \cdot \mathbf{q}, \mathbf{x} \cdot \mathbf{q}^\perp)$ (10), (11)

Table 1: Kernels used for different versions of the continuous Radon Transform, both in the 2D and in the 3D case. The numbers below each expression refer to the equations that define the projection models.

## The discrete case

In this section, we first introduce a convenient notation for the data and object and then revise the expressions described above by rewriting them in their discrete version. Some basic issues involved in the sampling of SPECT data are also discussed.

### Data space

SPECT data are intrinsically discrete:  $L$  sinograms are measured, where  $L$  is the number of planes. Each sinogram consists of  $M$  projections, each of which is related to one of  $M$  projection angles  $\Phi_m$ . Finally, each projection is sampled at  $K$  equally-spaced sample points, which can be mapped to the structure of the collimator array. According to these considerations, the set of parallel, discrete projections relative to each single angle can be seen as discrete radiography of the

three-dimensional object, registered on the detector surface. For simplicity, the radiography (respectively the detector surface) is usually partitioned into square pixels, rather than generically rectangular ones.

In order to avoid a too heavy notation, we will use the following block representation for the data<sup>7</sup>:

$$[g] = \begin{pmatrix} \mathbf{g}_1 \\ \vdots \\ \mathbf{g}_L \end{pmatrix} \quad (12)$$

Here  $[g]$  is the stack of the  $L$  data slices  $\mathbf{g}_1, \dots, \mathbf{g}_L$  of dimension  $K \times M$  each, i.e. of all sinograms. The single vectors  $\mathbf{g}_l$  are themselves composed by elements  $g_{mk,l}$ , that represent the number of photons collected by the detector with index  $(k,l)$ , when positioned at angle  $\Phi_m$ ; these elements are the samples of the continuous values  $g(\Phi_m, s, z)$  to which they are related by

$$g_{mk,l} = \int_{-\infty}^{+\infty} \int_{-\infty}^{+\infty} g(\Phi_m, s, z) \chi\left(\frac{s_k - s}{\Delta s}\right) \chi\left(\frac{z - z_l}{\Delta z}\right) ds dz \quad (13)$$

$m = 1, \dots, M; k = 1, \dots, K; l = 1, \dots, L$

where  $\chi$  is the characteristic function on  $(-1/2, 1/2)$  and  $\Delta s$  and  $\Delta z$  are the dimensions of an elementary picture element.

### Object space

In a similar way as done for the data, we can also provide a discrete representation of the unknown source distribution. The object space can be thought of as a cube consisting of  $N_x N_y N_z$  elementary volumes of dimension  $(\Delta x, \Delta y, \Delta z)$ : each of the  $N_x N_y$  matrixes represents a slice of the object of thickness  $\Delta z$ , cut perpendicularly to the tomographic axis. In block notation, the object is expressed as

---

<sup>7</sup> We will also omit the subscripts “2D”, “3D” and “2D+1” underneath the data symbol  $g$ , unless the nature of the model can not be inferred from the context.

$$[f] = \begin{pmatrix} \mathbf{f}_1 \\ \vdots \\ \mathbf{f}_{L'} \end{pmatrix} \quad (14)$$

where  $[f]$  is the stack of all  $L'$  object slices  $\mathbf{f}_1, \dots, \mathbf{f}_{L'}$  of dimension  $N \times N$  each. The single vectors  $\mathbf{f}_{l'}$  are themselves composed of elements  $f_{ij,l'}$  that represent the number of photons emitted at voxel  $(i, j, l')$ ; these elements are the samples of the continuous values  $f(x, y, z)$  to which they are related by

$$f_{ij,l'} = \int_{-\infty}^{\infty} \int_{-\infty}^{\infty} \int_{-\infty}^{\infty} f(x, y, z) \chi\left(\frac{x_i - x}{\Delta x}\right) \chi\left(\frac{y_j - y}{\Delta y}\right) \chi\left(\frac{z_{l'} - z}{\Delta z}\right) dx dy dz \quad (15)$$

$i = 1, \dots, N; j = 1, \dots, N; l' = 1, \dots, L'$

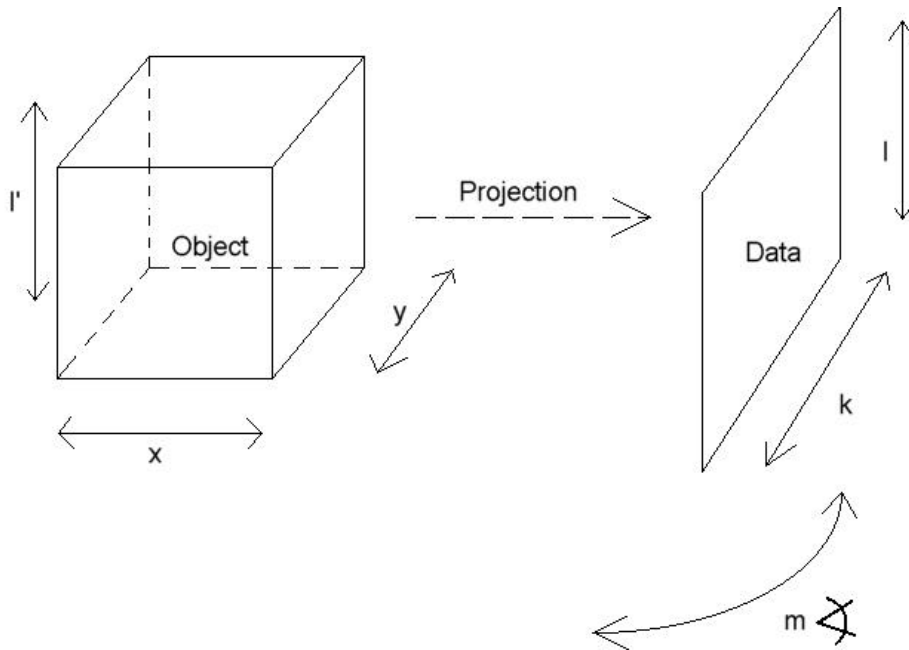


Figure 16: Object and Data space.

## Object-data mapping

Before suggesting a discretized version of the 2D and 3D Blurred Radon Transforms, a few observations related to the projection process are necessary, or, more precisely, related to the relationship between the discretized object slices and the discrete data slices. As a general rule, we will establish that for each data slice, the corresponding object slice is the one placed on the same plane  $z$ . This means that the indexes  $l$  and  $l'$  will be consistent with each other, i.e. the values of indices  $l$  and  $l'$ , related to some data slice and its correspondent object slice, respectively, are always equal.

As far as the axial dimensions of object and data are concerned, it is to be noted that when the real extent of the object in the  $z$  direction is larger than the  $z$  extension of the available data, Gibbs-like artifacts may appear in the reconstruction; a possible solution to avoid this is to consider - in the mathematical model - a number  $L'$  of object slices greater than the number  $L$  of data slices. However, we will assume here that the object being reconstructed always fits well inside the field of view of the detector, so that we can set  $L=L'$  without loss of generality.

## The 3D discrete Blurred Radon Transform

According to the notations introduced so far for the data and object, we can now write a discretized expression of the 3D Blurred Radon Transform:

$$\mathbf{g}_l = \sum_{l'=1}^L \mathbf{E}_l^{l'} \mathbf{f}_{l'} \quad (16)$$

$(l = 1, \dots, L)$

where  $\mathbf{E}_{3D}$  represents the fully 3D projector in block notation.

Note that due to the cylindrical structure of the tomograph, the geometrical and physical concepts that lie behind the acquisition of the data on one plane are the same for each single sinogram. Moreover, as discussed above, because of the blur due to the collimator geometry, the radiation source lying on one specific plane contributes to both the counts collected at that very same plane as well as to the data collected at neighbour transaxial levels – the number of levels being determined by the voxel-detector distance  $t$ : the farther the voxel is from the detector, the larger the number of influenced data slices. As already mentioned, this is expressed in the continuous formula of the Radon Transform equation (3) by the convolution along the  $z$  direction. The discretized version of a convolution operator always presents a Toeplitz structure, that is emphasized by the block notation used above: every single entry  $\mathbf{E}_1^{l'}$  of the 3D projector  $\mathbf{E}_{3D}$  is itself a Toeplitz matrix of elements  $E_{mk}^{ij}$ , and it represents a 2D projector, mapping one single object slice to one single data slice. The physical meaning of its elements  $E_{mk}^{ij}$  should be obvious.

For consistency with the “stack notation” used in equations (12) and (14), we will refer to the  $L \times L$  square matrix that represents the 3D projector as  $[E]_3$ , and to the  $(N \times N) \times (K \times M)$  2D ones as  $[E]_2$ . Thus, we have

$$[g] = [E]_3 [f] \quad (17)$$

Furthermore, we can also set

$$\mathbf{E}_1^{l'} = [E_{l'-1}]_2$$

where every  $[E_n]_2$  projects onto data slice  $l'+n$ , if applied to the  $l'$ -th object slice. It is not difficult to show that, due to symmetrical properties,  $[E_{-n}]_2 = [E_n]_2$ . Thus, we can conclude the discussion about the discrete 3D Blurred Radon Transform by expliciting equation (16) as

$$\begin{pmatrix} \mathbf{g}_1 \\ \vdots \\ \mathbf{g}_L \end{pmatrix} = \begin{pmatrix} [E_0]_2 & \cdots & [E_{L-1}]_2 \\ \vdots & \vdots & \vdots \\ [E_{L-1}]_2 & \cdots & [E_0]_2 \end{pmatrix} \begin{pmatrix} \mathbf{f}_1 \\ \vdots \\ \mathbf{f}_L \end{pmatrix} \quad (18)$$

### The 2D discrete Blurred Radon Transform

In the bidimensional case the discrete Blurred Radon Transform can be derived from the 3D case based on reasoning analogous to that described in the continuous case for deriving equations (10) and (11) case from the 3D form of equation (9): due to the independence of each projection along the  $z$  axis, the full projector is expressed by a diagonal matrix, with elements  $[E]_2$  each mapping one single object plane to the corresponding data plane, all in the same way – thus they all are the same. Moreover, apart from a scaling factor, they equal the  $[E_0]_2$  elements that lie on the diagonal of the fully 3D projector of equation (18).

Hence, the corresponding 2D versions of equations (16), (17) and (18) introduced above for the 3D discrete case are, respectively,

$$\mathbf{g}_l = \sum_{i=1}^L \mathbf{E}_i^l \mathbf{f}_i = [E]_2 \mathbf{f}_l \quad (19)$$

$(l = 1, \dots, L)$

$$[g] = [E]_{2D} [f] \quad (20)$$

and

$$\begin{pmatrix} \mathbf{g}_1 \\ \vdots \\ \mathbf{g}_L \end{pmatrix} = \begin{pmatrix} [E]_2 & 0 & \cdots & 0 \\ 0 & [E]_2 & & 0 \\ \vdots & & \ddots & \vdots \\ 0 & 0 & \cdots & [E]_2 \end{pmatrix} \begin{pmatrix} \mathbf{f}_1 \\ \vdots \\ \mathbf{f}_L \end{pmatrix} \quad (21)$$

Computationally, the 2D model is simpler than the 3D one: instead of having to determine all  $\mathbf{f}_i$  simultaneously, only  $L$  2D problems have to be solved and then stacked onto each other to obtain a 3D estimate of the object. These computations can be performed either sequentially – thus requiring the memory resources of a single 2D reconstruction – or in parallel, due to the assumption that the 2D

projections are independent: in this way, the time complexity is reduced to the same order of magnitude of a single plane reconstruction.

A summary of all expressions of the Blurred Radon Transform is given at the end of the next section in Table 2.

## **The 2D+1 approximation of the 3D projection model**

We present here a model we refer to as “2D+1”, because it lies in between the 2D and the 3D models described above: it aims at approximating the quality of a 3D scheme, by addressing the problem of the PSF’s shift variance along the  $z$  axis, but at the same time it features complexity properties comparable to a 2D method, both in terms of space requirements for the projector matrix and in terms of time necessary to invert the model and extract an estimate of the source distribution. Thus, it synthesizes into a single scheme the advantageous properties of the two approaches described above.

The basic idea is to fully take into account the shift variance of the PSF on transaxial planes, as both the 2D and the 3D techniques do, but only approximate the properties of the PSF in the  $z$  direction modeled in the 3D case: this is achieved by accounting for the PSF’s axial extent in a constant way, instead of as a function of the distance  $t$  between the source and detectors as in the 3D model, or completely neglecting it, as in the 2D model.

Graphically, one can picture the 3D PSF as a circle, with a radius varying as a function of the distance  $t$ ; the 2D PSF as a projection of the circle into a segment lying on the plane onto which the projection occurs, and with length varying as well as a function of the distance  $t$ ; the 2D+1 PSF as a deformation of a circle, obtained by “freezing” the radius to a constant value along  $z$ , and allowing it to vary as a function of  $t$  in the transaxial direction only. These concepts are shown in Figure 17.

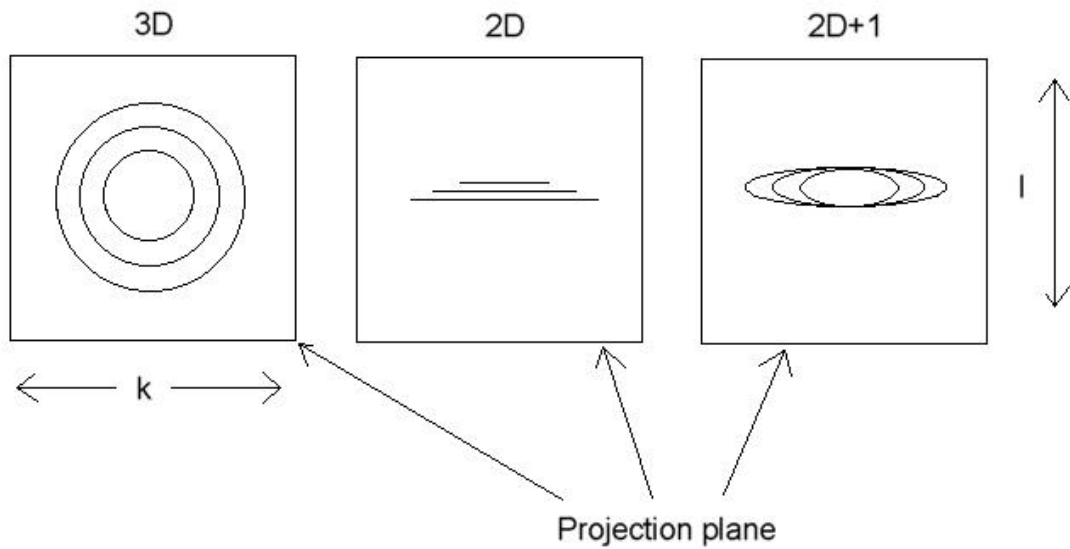


Figure 17: Projection of a point-like source with the 3D, 2D and 2D+1 models.

### The 2D+1 continuous Blurred Radon Transform

One can exploit the properties mentioned above and derive a mathematical model for the 2D+1 by splitting the 3D kernel into two factors: the first is given by the 2D kernel and describes the PSF on a transaxial plane; the second depends on the  $z$  variable only and “spreads” the 2D projection on a constant number of planes - no matter what the distance between source and detector is - that are neighbouring to the one on which the photon source lies. Thus, the resulting kernel is an extension of the 2D that improves it towards the 3D one:

$$E_{2D+1}(s, t, z) = E_{2D}(s, t) A(z) \quad (22)$$

The exact values of  $\mathbf{A}$  depend on the system and they can be obtained from the fully 3D model that is to be approximated. The 2D+1 Blurred Radon Transform thus becomes

$$\begin{aligned}
g_{2D+1}(\Phi, \mathbf{s}, z) &= \iiint_{2D+1} f(\mathbf{x}, z') E_{2D+1}(\mathbf{s} - \mathbf{x} \cdot \mathbf{q}, \mathbf{x} \cdot \hat{\mathbf{q}}, z - z') d\mathbf{x} dz' \\
&= \int \left[ \iint_{2D} f(\mathbf{x}, z') E_{2D}(\mathbf{s} - \mathbf{x} \cdot \mathbf{q}, \mathbf{x} \cdot \hat{\mathbf{q}}) d\mathbf{x} \right] A(z - z') dz' \quad (23) \\
&= \int_{2D} g(\Phi, \mathbf{s}, z') A(z - z') dz' .
\end{aligned}$$

### The 2D+1 discrete Blurred Radon Transform

A discrete representation of the 2D+1 kernel of the Blurred Radon Transform can be easily derived either from the continuous version or from the 2D and 3D discrete kernels. We will chose the latter approach. It is obvious that the 2D+1 projection matrix has a Toeplitz structure, with 2D projection matrixes  $[E]_2$  on its diagonal that map each single plane of the object into the corresponding plane in the data space. The off-diagonal elements that describe crosstalk effects among nearby slices cannot possibly be null as in the 2D approximation (equation (21)). At the same time, because the contribution of the PSF in the axial direction is not fully modeled here, but only approximated by neglecting its shift-variance property, these entries will not have such a complex structure as in the fully 3D case. More specifically, the  $[E_n]_2$  elements of the 3D case (equation (18)) will be approximated by “weighted 2D projectors” of the form  $[E]_2 \alpha_n$ , where the  $\alpha_n$  have the same symmetry properties as the  $[E_n]_2$ , namely  $\alpha_{-n} = \alpha_n$ . The  $\alpha_n$  - defined over a suitable range of index  $n$  - represent an average estimate of the fraction of photons emitted by some slice  $l'$  of the object and detected at data slice  $l'+n$ . Because each of them is a fraction of a unity, the property  $\sum_n \alpha_n = 1$  also holds for these weights. They can be ordered into a square matrix  $[A]_1$  that, once again, presents a Toeplitz structure, reflecting the convolution contained in equation (23) that defines the 2D+1 Blurred Radon Transform in the continuous case. The elements  $A_1^{l'} = \alpha_{l'-l}$  of the matrix are related to the continuous form by a discretization expression similiar to equations (13) and (15):

$$\alpha_l = (\Delta z)^2 \int_{-1/2}^{1/2} \int_{-1/2}^{1/2} A[\Delta z(z - z' + l)] dz dz' \quad (24)$$

where  $z - z' = (l')Dz$  is assumed.

In summary, the 2D+1 projection matrix combines the 2D operator  $[E]_2$  with the weights  $\alpha_n$  by a Kronecker product with the LxL Toeplitz matrix  $[A]_1$ :

$$[E]_{2D+1} = \begin{pmatrix} [E]_{2\alpha_0} & \cdots & [E]_{2\alpha_{L-1}} \\ \vdots & \vdots & \vdots \\ [E]_{2\alpha_{L-1}} & \cdots & [E]_{2\alpha_0} \end{pmatrix} = [E]_2 \otimes [A]_1 \quad (25)$$

The properties of the Kronecker product allow us to express the approximate projector in a very convenient form that points out its computational cheapness:

$$\begin{aligned} [g] &= [E]_{2D+1}[f] \\ &= [A]_1 \otimes [E]_2[f] \end{aligned} \quad (26)$$

This clearly evidences the way the data are obtained from the object: first L 2D projections are performed over the L slices of object  $[f]$ . The results are then spread over the elements  $g_l$  of the data  $[g]$  in a weighted arrangement by matrix  $[A]_1$ . The computational cost of the first step is in the order of L 2D projections, in comparison to which the cost of spreading the results over the data is neglectable. Thus, the 2D+1 approximation is computationally equivalent to the 2D one. We will later show how the results obtained by the 2D+1 model present an improvement upon the 2D method and are comparable to those achieved by the fully 3D projector.

	Fully 3D	2D approximation	2D+1 approximation
Continuous form	$E_{3D}(s, t, z)$ (9)	$E_{2D}(s, t, z)$ (10), (11)	$E_{2D+1}(s, t, z) = E_{2D}(s, t) A(z)$ (22), (23)
Block notation	$E_{3D}$ $[E]_{3D}^3$ (16)      (17)	$E_{2D}$ $[E]_{2D}^3$ (19)      (20)	$E_{2D+1}$ $[E]_{2D+1}^3$ (26)
Vectorial form	$\begin{pmatrix} [E_0]_2 & \dots & [E_{L-1}]_2 \\ \vdots & \vdots & \vdots \\ [E_{-1}]_2 & \dots & [E_0]_2 \end{pmatrix}$ (18)	$\begin{pmatrix} [E]_2 & 0 & 0 \\ 0 & \ddots & 0 \\ 0 & 0 & [E]_2 \end{pmatrix}$ (21)	$\begin{pmatrix} [E]_{2\alpha_0} & \dots & [E]_{2\alpha_{L-1}} \\ \vdots & \vdots & \vdots \\ [E]_{2\alpha_{L-1}} & \dots & [E]_{2\alpha_0} \end{pmatrix}$ (25)

Table 2: Kernels used for different versions of the Blurred Radon Transform, both in the 2D and in the 3D case. The numbers below each expression refer to the equations that define the projection models.

## Iterative reconstruction

As we have seen, direct methods such as the FBP are based on a line-integral model that is only approximate. Moreover, noise is not explicitly considered, which turns out to be a major issue in SPECT, where the photon count is low: the resolution, intrinsically limited by the geometrical factors described above, is quite poor at acceptable noise levels.

On the other hand, the more sophisticated models we have introduced, that account for collimator blur and that accurately describe the system response, do not present any closed form and the solution can not be computed directly: it is generally found through an iterative procedure that optimizes a cost function over the image space, thus leading to a solution that fulfills the desired properties. Model-based iterative approaches require i) the design of an accurate model, describing the key-properties of the system, as, for instance, the noise related to data and acquisition process or the collimator geometry as we have done above, ii) the selection of an objective function over the image space, that usually maps the model into a concave maximization (or, equivalently, a convex minimization) problem, so that the solution can be found as the reconstruction that optimizes the cost function itself; iii) the design of an iterative algorithm that finds the solution in an efficient, i.e. fast and rapid way.

Iterative algorithms have regularizing properties when applied to ill-conditioned problems: the number of iterations performed plays the role of regularization parameter and determines the quality of the reconstruction. The best reconstruction is the one obtained at the iteration at which the objective function is maximized (respectively minimized if the cost function is convex): this is the “optimal” iteration number, at which the algorithm must be stopped. In the case of simulations, where the “true” solution is known, the optimal iteration number can be easily determined. On contrast, in the case of experimental data, the determination of a reliable rule for stopping the iterations is a key-issue and can turn out to be a rather difficult task, since the “truth” is not known. Many iterative schemes provide an acceptable solution to the optimization problem even before convergence, so that they are stopped ahead of the “optimal time”. Thus, even though the solution to a concave maximization (respectively convex minimization) problem is theoretically independent of the iterative algorithm, in the practice it becomes a function of the algorithm and of the number of iterations performed. Moreover, different schemes do not necessarily lead to the same image when applied to the same objective function, if they are stopped before full convergence.

We will now briefly present a few, widely used iterative algorithms, along with efficient objective functions, that can be applied to our 2D+1 model as well as to the full 3D one and to its 2D approximation in order to find satisfying solutions to the SPECT problem. Later, we will show how these methods perform in simulations and experiments and we will use them to validate the efficiency of the 2D+1 model.

### **The CG (Conjugate Gradient) algorithm**

The CG [Han95, Hes52] belongs to a class of algorithms called *descent*<sup>8</sup>, in that they search the minimum of a convex function by *descending* along a certain path towards the solution. The basic idea of descent methods is to choose a search direction at each iteration, and minimize the function along that direction by using a line minimization method. The direction can be chosen according to different criteria, as, for instance, by simply alternating variables over the set of unit vectors, or by selecting the greatest slope at each step.

The peculiarity of Conjugate Gradient methods is that they choose search directions using information gained from previous searches: this is achieved by selecting directions that are conjugate to the Hessian of the surface represented by the objective function. To see what this means, consider a line search along a particular direction: this ensures that the gradient along that direction is zero. If the next direction is conjugate to the first, the subsequent search will not affect the gradient along the original direction. Thus, by looking along  $n$  independent directions, we get  $n$  directions for which the gradient is zero. For an  $n$ -dimensional space quadratic surface, a CG method converges in  $n$  or less steps, thus proving to be extremely fast. For this reason, it has been proposed by several authors for quality restoration of SPECT data [For89, Hue77, Tsui91]. A problem related to gradient based

---

<sup>8</sup> In a similar way, one could consider *ascent* methods, that seek the maximum of a concave function by iteratively *ascending* along a certain path. Without any loss of generality, we will only refer here to the descent methods, since we will consider a convex objective function.

methods in general, is that they do not ensure non-negativity of the solution. Such a property can only be achieved by imposition of specifically designed constraints, as shown in [Kau93].

Here, we will use a preconditioned form of the CG, proposed by Huesman *et al* [Hue77], to minimize the weighted least-squares functional

$$\chi^2([f]) = \left\langle C^{-1}([E]_3[f] - [g]), ([E]_3[f] - [g]) \right\rangle$$

where  $\langle \cdot, \cdot \rangle$  denotes the Euclidean scalar product and  $C$  is a symmetric positive definite matrix that modifies the metric in the data space: it is usually taken as the error covariance matrix, which, in the case of uncorrelated noise, has only diagonal entries given by the variances relative to the acquired  $g_{km,l}$  [Ber89, Ber95, Van87]. This way, the statistical uncertainties of the data are embedded in the functional that is to be minimized. Following [Hue77] and [Tsu91] we assume a Poisson probability of the noise.

### **The EM-ML (Expectation Maximization-Maximum Likelihood) algorithm**

The EM-ML, introduced by Shepp and Vardi [She82] and Lange and Carson [Lan84], consists of applying the EM algorithm [Dem77] to the problem of tomography, formulated in a statistical framework, in terms of a Maximum Likelihood. We will first briefly introduce the ML method and then see how the EM algorithm can be combined with it, leading to an elegant closed form update equation that converges to the desired solution.

The data can be modeled as a collection of independent random variables, with the mean given by the corresponding entries of  $[E]_3[f]$  (where  $[f]$  represents the mean emission rates) and probability or likelihood given by a Poisson distribution. This way, the mapping from the image  $[f]$  to the mean of the detected events includes the physical model for the detection system. In this mapping, other factors, as scatter or background radiation, can be easily taken into account. The maximum likelihood  $L$

estimator is the image that maximizes the likelihood over the set of feasible images  $[f] \geq 0$ .

The goal of the EM algorithm is to approximate a probability function and, therefore, it is typically used to compute maximum likelihood estimates given incomplete samples, as in the case of SPECT and PET data. It basically operates alternating between two steps, referred to as the expectation and the maximization steps, respectively. In the first step, it computes the conditional mean of the data log likelihood function  $\ln L([\underset{2D+1}{E}] | [f])$ , from  $[g]$  and the current image estimate  $[f]^{(r)}$ :

$$E - step : Q([f] | [f]^{(r)}) = E[\ln L([\underset{2D+1}{E}] | [f]) | [g]; [f]^{(r)}]$$

In the second step, it maximizes the previously computed quantity with respect to the image:

$$M - step : [f]^{(r+1)} = \arg \max_{[f]} Q([f] | [f]^{(r)})$$

This step can be explicated in a closed form as:

$$M - step : [f]^{(r+1)} = \frac{[f]^{(r)}}{[\underset{2D+1}{E}]_3^T [1]} [\underset{2D+1}{E}]_3^T \left( \frac{[g]}{[\underset{2D+1}{E}]_3 [f]^{(r)}} \right)$$

where  $[1]$  is a projection set with all pixels equal to 1, and the products and divisions are to be understood as component-by-component operations. This form shows that the images at each new iteration are obtained by backprojecting the data, normalized by the estimate  $[g]^{(r)} = [\underset{2D+1}{E}]_3 [f]^{(r)}$ , and multiplying by the current image estimate  $[f]^{(r)}$  normalized by  $[\underset{2D+1}{E}]_3^T [1]$ . The iterations are usually started with  $[f]^{(0)} = [1]$ , an object with all voxels set to 1.

This algorithm features interesting characteristics, such as conservation of an initial domain, normalization of each current solution, and non-negativity of the solution, naturally constrained by the iteration. Because of its elegance in providing the

estimates updates by a closed form, and due to the improvements in image quality, it has led to wide interest in ML approaches and has inspired abundant subsequent research. However, it presents two fundamental problems:

It exhibits instabilities, particularly at higher iterations in high variance in the estimated voxel intensities. This can be dealt with in several ways, as by early termination of the algorithm [Coa91, Joh94, Vek87], by post-smoothing of the reconstruction [Lla93, Sil90] or using Grenander's method of sieves [Gre81].

It suffers from slow convergence rate. Several methods have been proposed to speed up the algorithm, many of them involving a reformulation of the E-step update equation [Kau87, Lew86, Raj92], using over-relaxation or line-search methods, or returning to standard gradient ascent methods, as the preconditioned CG [Kau93]. It has been shown [Tsui91] that, in order to obtain an acceptable solution, EM requires a number of iterations about ten times higher than the one required by CG, which is the reason why EM is not in widespread use in clinical environments. In the case of reconstructions with the fully 3D model, the computational overhead is practically unacceptable; in the case of our approximate projector  $[E]_{2D+1}^3$ , the time required for a reconstruction is of the same order of magnitude as that required by CG on the fully 3D model.

## The OSEM (Ordered Subset Expectation Maximization) algorithm

The OSEM algorithm was proposed as an alternative version of the EM algorithm, aiming at speeding up the low convergence rate of the latter [Hud92, Hud94, Li94]. It belongs to the class of *ordered-subset*, or *block-iterative* methods, that are based on the idea of partitioning the data into disjoint, equally sized subsets or blocks, using a single block at each iteration, instead of the whole data volume. Thus, the closed-form update equation of the EMML algorithm can be rewritten as

$$M - step : [f]^{(r+1,k)} = \frac{[f]^{(r,k-1)}}{\left[ \begin{array}{c} [E] \\ [E] \end{array} \right]_3^T [1]_{2D+1}} \left[ \begin{array}{c} [g] \\ [E] \end{array} \right]_3 [f]^{(r,k-1)}_{2D+1}$$

where  $k=1, \dots, Q$  denotes the partition,  $r$  is the number of complete cycles through the  $Q$  subsets, and  $[f]^{(r,0)} = [f]^{(r-1,Q)}$  is assumed.

In order to improve the convergence rate, subset balance [Hud94], as well as careful selection of subset ordering [Gua94, Her93] and ordering of the items within the subsets themselves, are recommended. In SPECT, for instance, the projections should be partitioned in such a way that the emission from each pixel has the same probability of being detected in each subset. As this turns out to be difficult to realize in practical cases, they are usually grouped into each subset so that their separation in angle is maximal, which in turn means that the number  $Q$  of blocks is a factor of the number of angular views.

When only one subset is used, OSEM corresponds to EMML; in all other cases – except for singleton blocks, to which OSEM does not apply – it has been shown to perform as well as EMML in terms of quality of the reconstructions, but to outperform it in terms of convergence rate. More precisely, the result of  $r$  iterations of EMOS with  $Q$  subsets is roughly equivalent to the one given by  $r \cdot Q$  iterations of EMML; bigger values of  $Q$  correspond to higher convergence speeds at the cost of an increasing noise in reconstruction [Man95]. Also, in early iterations, OSEM produces considerable improvements in terms of convergence rates, but, as for the

case of EMMML, it causes high variance at large iteration numbers: in general, it does not ultimately converge and enters a limit cycle condition. However, this is not an issue of major importance, as the algorithm can usually be terminated after a few iterations. Alternatively, final iterations over the entire data can be performed.

### **Inversion methods suggested by the structure of the 2D+1 projector**

Here, we outline an alternative way to compute a solution to the 2D+1 model. The method is somewhat *sui generis*, in that it is suggested by the structure of the 2D+1 expression itself: it cannot be applied to the 2D or 3D models, nor can it be classified into any category of known, “standard” algorithms.

The basic idea of the method is to split the reconstruction process into two steps, according to the form of equation (26): in the first step the effects due to the matrix  $[A]_1$  are addressed by deconvolving the data  $[g]$  to obtain a stack of blur-free projections; in the second step the 2D operator  $[E]_3$  is inverted in order to obtain a stack of 2D reconstructions.

Both of the two steps can be accomplished by means of existing methods. To illustrate an example, we briefly sketch the way we have implemented the algorithm in the simulations described in the next section.

Concerning the first step, we note that the 2D+1 equation (26) can be written in terms of the 2D equation (20) as

$$[g]_{2D+1} = [E]_{2D+1} [f] = [A]_1 \otimes [E]_2 [f] = [A]_1 \otimes [g]_{2D}$$

We want to invert the 64x64 Toeplitz matrix  $[A]_1$ , which corresponds to deconvolving the 2D+1 data to obtain blur-free projections: this can be done by representing the problem in diagonal form and using one of several regularization methods to compute the desired solution.

As we are working in the discrete case, the diagonalization can be achieved by means of a 1D DFT along the  $z$  direction, i.e. with respect to index  $l'$ . Since  $[A]_l$  is a circulant matrix, one first needs to double its size in each direction (and obtain another circulant matrix, four times as large), in order to avoid interperiod interference artifacts that appear when an aperiodic (de)convolution is implemented as a periodic one.

Among the several regularization methods proposed in the literature (we refer to [Ber95] and [Ber98] for a comprehensive description), we have used two deterministic algorithms – Tikhonov [Tik63] and SA-POS (Successive Approximation with the constraint of non-negativity), that belong to the class of constrained Landweber-Bialy iteration schemes [Bia59, Lan51, Pia97, You82] – and one statistical approach: the EM algorithm described above, for which an iteration scheme for deblurring of projections can be easily derived from the one presented earlier in this section.

The implementation of the second step, namely, the inversion of the 2D projection operator, only consisting in a sequence of 2D reconstructions, can be performed by either one of the CG, EM or OSEM algorithms already presented.

Beyond the computational low cost of this two-step algorithm, other advantages are the variety of methods to implement the two phases (including those, relative to the first step, that allow to incorporate useful constraints such as non-negativity, or properties derived from some *a priori* information on the solution), and the possibility of reconstructing only some slices of interest, instead of the entire volume, once the first deconvolution has been performed. This strategy permits relevant savings in computational time, since it is the reconstruction phase that represents the major component of the computational costs of the entire algorithm.

## Simulations and results

This section describes the simulations we have performed to validate both the accuracy of the 2D+1 projector-backprojector model (with respect to the fully 3D one) and its performance when it is used in combination with any of the iterative reconstruction algorithms mentioned above to invert SPECT data into the image space. The simulations are applied to data of a particular SPECT device, which we will describe in the subsection below. With reference to this particular scanner, we will also show how the  $\alpha$ -weights of equation (25) can be evaluated.

### The CERASPECT device

The SPECT device on which our simulations are based is called CERASPECT (Digital Scintigraphics Incorporated, Waltham, MA 02154, USA; Figure 1 of the “Overview” section); it is a brain scanner, located in the building of the Department of Motor Sciences at the University of Genoa, Italy.

Data are acquired on a 128x64 pixels detector<sup>9</sup>, at 120 different angles, with a distance of 3° from each others. Thus,  $M=120$ ,  $K=128$  and  $L=64$ , and each sinogram can be stored in a 120x128x64 matrix. We reconstruct objects into 64 slices, each of size 128x128 pixels<sup>10</sup>. Hence,  $N=128$  and  $L'=L=64$ .

In [Bal98] some basic properties of the PSF have been investigated. It has been found that its FWHM depends on the source-detector distance in an almost linear

---

<sup>9</sup> In the following, we express all distances and sizes using the pixel as a unit of measure: a pixel's side length is 1.67 mm.

<sup>10</sup> Images are reconstructed into 128x128 arrays when technetium is used as a radiotracer; when xenon is used instead, then image size is 64x64 pixels. Throughout the thesis we will refer to 128x128 reconstructions.

way, and it varies from 2.8 pixels, corresponding to a source-detector distance of 36 pixel, to 7.2 pixels, corresponding to a distance of 36 pixels; at the center of the camera, namely, when the source is located on the  $z$ -axis, at 89 pixels from the detector, the FWHM is 5 pixels. According to investigations performed on a similar device [Bai94], the FWHM values can be thought of as the radial values of a symmetrical PSF on the detector surface.

It is to be noted, that the CERASPECT features an annular collimator [Bal98, Hol90], whose radius amounts to about 15 cm. The effects of the collimator curvature had to be considered while performing these investigations.

In our implementation of the fully 3D projector model, we take all the above results into account. We model the collimator blur by a 2D Gaussian function [For97] that is symmetrical in the  $z$  and  $s$  directions, and with the FWHM depending on the source-detector distance and can be evaluated as described with details in [Bal98]. Moreover, as is usually assumed in SPECT, we limit the maximum number of slices that can be affected by the signal coming from one specific object plane. On the basis of experimental measurements, we set this limit to 10, which means that the signal coming from a single voxel influences up to  $2 \times 10 + 1$  data slices.

### **Evaluation of the $\alpha$ weights for the 2D+1 model**

The  $\alpha$ -weights introduced in equation (25) represent a quantitative estimate of how the activity emitted by the source at a specific plane is projected onto the detector over the adjacent planes. We have estimated these values by an experimental procedure that exploits the symmetrical properties of the system's geometry.

We have considered a disk of uniform activity, with a radius of 55 pixels, centered with respect to the camera, i.e. located on the central transaxial plane (32<sup>nd</sup> slice), with the center lying on the  $z$ -axis of the device. The background was constant, without any kind of activity. The disk's projections, represented by the  $g_{km,l}$  values,

were computed by means of the fully 3D projector  $[E]_{3, 3D}$ , and subsequently summed up over indexes  $k$  and  $m$ , to produce the set of values  $a_l$  given by

$$a_l = \sum_{m=1}^{120} \sum_{k=1}^{128} g_{km,l} \cdot \quad (l=1, \dots, 64)$$

Ideally, the  $\alpha$ -weights could be set to be equal to the  $a_l$  values, with an appropriate shifting of the indices, such that  $a_l = a_{l+32}$ ,  $l=-32, \dots, 32$ . In practice, however, it turns out that many  $a_l$  values are close to zero and can be neglected without any significant loss of information as far as the projector accuracy is concerned. This way, the  $[E]_{3, 2D+1}$  projection matrix is sparser, and computations are faster, since a smaller number of products is performed.

In this work, we only considered the 13 central  $a_l$ , with  $l$  ranging from 26 to 38: their sum is about 99.5% of the sum of the  $a_l$  over the full range of index  $l$ . These values were scaled so that their sum was equal to 1, and finally we set

$$\alpha_l = a_{l+32} \quad l=-6, \dots, 6 \quad \text{and}$$

$$\alpha_l = 0 \quad \text{for all other values of } l.$$

Figure 18a) shows one of the  $g_{km,l}$  3D projections of the disk of uniform activity, from which the  $\alpha$ -weights were derived. For comparison, a 2D projection of the same disk, computed by means of  $[E]_{3, 2D}$ , is shown in Figure 18b): this projection does not feature any extent along the  $z$ -axis.

In Figure 19, the 13  $\alpha$ -weights are plotted: the plot has a Gaussian shape with an FWHM value of approximately 4.7 pixels, which is slightly less than the value of 5 pixels one could expect as the average value. The reason for this difference with the FWHM relative to the PSF evaluated at the center of the camera is due to the curvature of the collimator.

### Accuracy of the 2D+1 projector approximation

To assess the accuracy of the 2D+1 projector, we performed both a qualitative and a quantitative investigation: the former was based on a visual inspection of some case-study projections, and the latter was based on an analytical error expression applied to a set of projections and to one of projection-back projection pairs. In both studies the data consisted of a point-like source located on the central transaxial plane, at some specific distance from the detector.

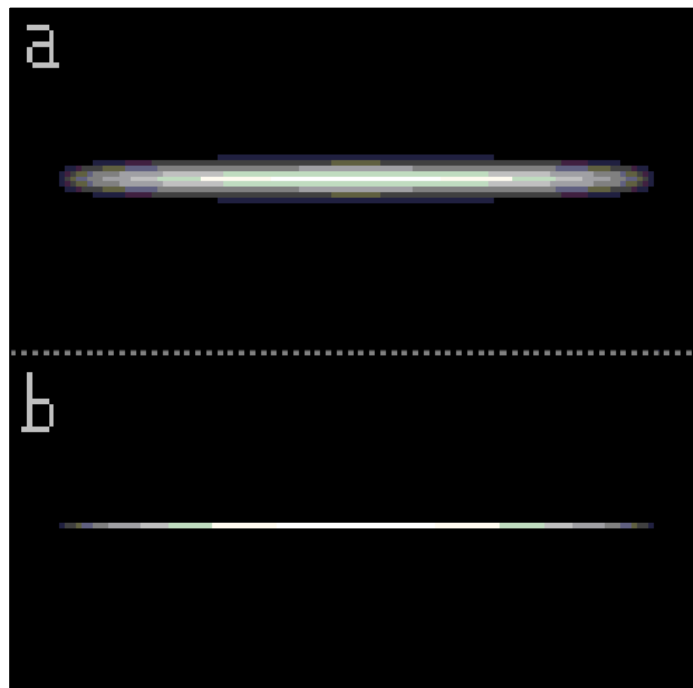


Figure 18: a) 3D and b) 2D projection of a disk of uniform activity, centered on the z-axis and placed on the 32<sup>nd</sup> plane, half way between the top and the bottom of the camera.

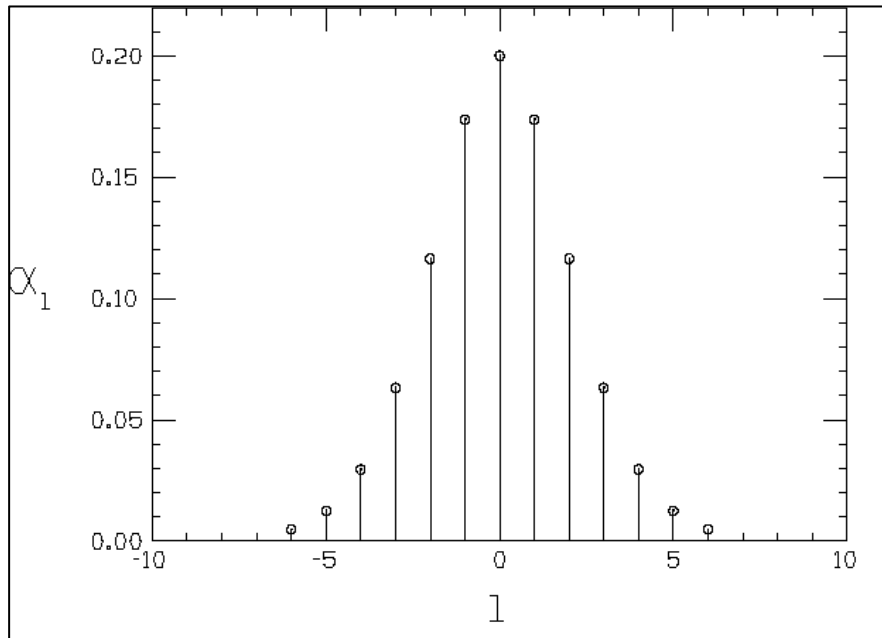


Figure 19: Plot of the 13 weights  $\alpha_l$  ( $-6 \leq l \leq +6$ ) used by the 2D+1 projector. All other weights are taken to be zero.

In the first study, we considered a single, 56 pixel off-axis voxel of activity, placed on the 32<sup>nd</sup> slice - i.e. halfway between top and bottom of the z-axis - in three different locations: a) at a minimum distance from the detector (33 pixels); b) at an intermediate distance of 82 pixels, chosen so that the corresponding FWHM amounted to approximately 4.7 pixels, for the reasons described above; c) at a maximum distance of 145 pixels. We then computed some angular views of these activity voxels by means of the 3D, the 2D+1 and the 2D projectors, and performed a visual inspection on the results, which are shown in Figure 20.

The left column, which is to be considered to be the “reference” one, shows the views relative to the fully 3D projector  $[E]_3^{3D}$  : the PSF has a symmetric, circular shape with radius increasing at greater distances between the detector and the activity. The central column is the one relative to the 2D+1 projector  $[E]_3^{2D+1}$  : the PSF clearly features an elliptical shape – its height remaining constant over varying distances between the source and the detector, whereas its extent along the  $s$  direction increasing at greater distances in much the same way as occurs in the case of the 3D projector. In particular, the 2D+1 view is almost identical to the 3D one, when the activity voxel is located at an intermediate distance of 82 pixels (see middle row of Figure 20), which occurs twice over a full rotation of the collimator. Finally, the third column displays the views obtained by means of the 2D projector  $[E]_3^{2D}$  : these are extremely poor in that, in this case, no extent along the  $z$ -axis is modeled, so that the PSF is reduced to a horizontal segment of varying length, depending on the detector-activity distance. This gives rise to artifacts that are mostly evident when reconstructions of full 3D objects are imaged in sagittal or coronal views, and that represent the major cause of the low accuracy of the 2D model.

In order to reduce these effects, one could consider a PSF that, while still being space shift-invariant, has a circular shape, with a radial FWHM set to some reasonable value, as, for instance, 5 pixels. This model turns out to be computationally equivalent to the 2D one, but yields reconstructions that are more relevant than those obtained by  $[E]_3^{2D}$  , especially when it comes to comparisons with the other two projectors. In the simulations described in the following subsection, we will also consider such a projector variant.



Figure 20: Projection of a 56 pixel off-axis voxel at the minimum (top row), intermediate (middle row) and maximum distance from the detector (bottom row). These angular views are obtained by means of the fully 3D (left column), the 2D+1 (middle column), and the 2D projector (right column).

The data on which we performed the quantitative study to compare the efficiency of different projectors are very similar to those used for the qualitative evaluation. A single, non zero voxel of activity was placed in the central transaxial slice, i.e. at halfway between the top and the bottom of the projector; instead of only three locations, as used above, we chose 11 different distances between the voxel and the detector, varying from 1 up to 125 pixels: a central position, i.e. the source lying on the z-axis, and 5+5 other locations, which, due to the rotational symmetry of the camera, are pairwise symmetric (and equivalent as far as the (back-)projections are concerned).

In this study, we restricted our attention to the 3D and the 2D+1 models and dropped off the 2D one, since we were mainly interested in an estimate of how much our approximation diverges from the “optimal” 3D case. For every object  $[f]$ , we computed both the two projections -  $[E]_{3D} [f]$  and  $[E]_{2D+1} [f]$ , respectively, – and the corresponding projection-backprojection pairs given by  $[E]_{3D}^T [E]_{3D} [f]$  and  $[E]_{2D+1}^T [E]_{2D+1} [f]$ , respectively. The choice of also including the action of the projector-backprojector pairs was suggested by the consideration that iterative inversion algorithms often use such a sequence. Finally, we computed the relative error of the 3D and the 2D+1 models, using the expression

$$\frac{\| ([E]_{3D} - [E]_{2D+1}) [f] \|}{\| [E]_{3D} [f] \|}$$

for the projections and

$$\frac{\| ([E]_{3D}^T [E]_{3D} - [E]_{2D+1}^T [E]_{2D+1}) [f] \|}{\| [E]_{3D}^T [E]_{3D} [f] \|}$$

for the projection-backprojections.

The results are plotted in Figure 21. The projection error increases for voxels departing from the z-axis position, while the projection-backprojection error remains substantially constant at the level of 4% for a diameter of about 75 pixels. The cause of the small hump at the center is due to the fact that the FWHM of the  $\alpha$ -weights we have chosen is smaller than the value of 5 pixels corresponding to the center. Thus, the error for the voxels in close proximity to the z-axis is larger than for voxels somewhat off-axis. But it must be noted that, overall, there are more off-axis voxels than in-center ones.

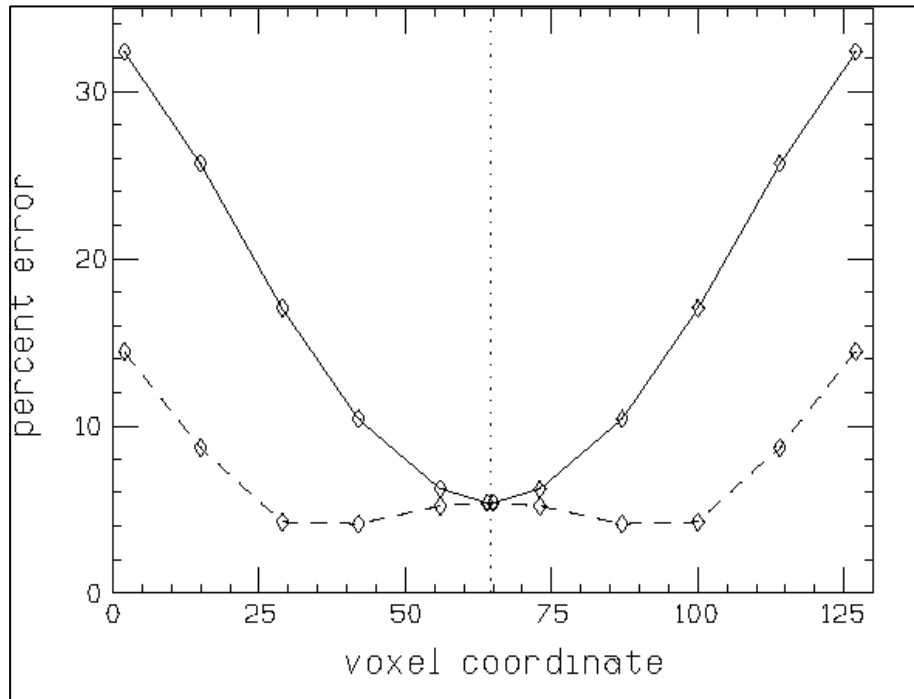


Figure 21: Plot of the percentage projection error (—) and of the percentage projection-backprojection error (- - -) for voxels at increasing distances from the z-axis (marked by the vertical dotted line). The computations have been performed in correspondence to the points marked by the diamonds. The horizontal distance from each one of these points to the vertical dotted lines measures the distance of the voxel from the z-axis in pixel units.

### Evaluation of the algorithms and validation of the reconstructions

In order to provide a complete study of the efficiency of our 2D+1 approximation, we have reconstructed a 3D brain phantom, using different algorithms on different projection models; we have compared the results and discussed the benefits and the disadvantages of each single case, also considering factors such as the computational costs and the clinical requirements on the quality of the images.

### **The study: data set and reconstruction schemes**

We generated a 64 slice brain phantom by interpolating the 19 plane 3D Hoffman phantom [Hof90] to a 57 slice volume and adding void slices at the top and at the bottom. The resulting object was projected by means of a 3D projector, simulating the process of data acquisition as performed by the CERASPECT. Thus we obtained a set of projections that we subsequently scaled to 7 Mcounts, the average number of photons detected during a standard clinical brain scan. Finally, the data was contaminated by Poisson noise, which we generated by a routine based on the rejection method [Pre94]. The purpose of the entire procedure was to simulate the effects of collimator blur in a real brain scan.

At this point, we need to clarify that we deliberately did not model any scatter, nor attenuation, basically for the sake of simplicity. As a matter of fact, the study focuses on collimator blur in the presence of noise: thus, we have tried to isolate this aspect and avoid the inclusion of other factors that might influence and bias the study.

In the practice, the inclusion of these two factors is rather straightforward: scatter correction can be performed directly by the device, using a technique of window subtraction, as suggested in [Jas84], that consists of acquiring data over two different energy windows – the photopeak one and the scatter one – and then subtracting the latter from the former. Thus, our study is equivalent to working on data that have already been compensated for scatter by the device.

On the other hand, attenuation can be easily included under the assumption that the attenuation coefficient is uniform over the object: such an assumption is quite realistic in the case of brain SPECT scans. Besides, our most recent version of the reconstruction code, that is currently being used on the CERASPECT at the San Martino Hospital in Genova, also includes scatter correction.

The data obtained were reconstructed by means of different algorithms: CG, EM, EM-OS with 12 subsets, and various two-step methods, all based on the CG for the second step (2D inversion) and on the schemes mentioned in section 0 for the first step (deconvolution). The CG algorithm was used in combination with four projection models, namely, the 3D, the 2D+1, a so called S-PSF and the 2D one. All other reconstruction algorithms were only applied to the 2D+1 projector.

The S-PSF model is basically a 2D one, with a shift invariant, circular, symmetric PSF, with a FWHM fixed to 5 pixels, uniform over the entire field of view. With such a Point Spread Function, in which no depth dependence is modeled, some peculiarities of the device on which we based our simulations became irrelevant – peculiarities that are mainly due to the curved detector geometry of the CERASPECT scanner. Hence, this model offers the possibility of exploiting some implementations of (back-)projectors, which are computationally convenient and of widespread use on standard cameras and for parallel collimation. Such projectors are based on the strategy of rotating the emission matrix, with the purpose of aligning its columns with the direction of projection [Tsui94, Wal97, Zen91], as opposed to all other projectors considered in this study, that are based on a voxel-driven technique instead.

In order to evaluate the accuracy of the S-PSF model we implemented both a 2D+1 and a fully 3D projector-backprojector pair, based on the strategy of a rotating emission matrix. These projectors also provided further insight into timing issues and complexity of the 2D+1 scheme as opposed to the fully 3D one, and to exploit the potential benefits of the 2D+1 approximation with reference to a very general class of SPECT scanners. It is worth highlighting that in the context of the S-PSF, the terms “2D+1” and “3D” do not refer to different approximations or models, but only to different algorithms.

We have finally evaluated the results in different ways as discussed below, trying to address the major interests, requirements, and clinical uses. A summary of the most meaningful figures of merit we considered is reported in Table 3.

Model	Reconstruction algorithm	Relative error (%)	Optimal iteration number	Timing requirement
<b>2D</b>	CG	37.6	7	8
<b>2D+1</b> <b>(SI-PSF+ rotator)</b>	CG	36.1	15	10
<b>Fully 3D</b> <b>(SI-PSF+ rotator)</b>	CG	36.1	15	44
<b>2D+1</b> <b>two-step method</b>	Tikhonov +	35.1	$\mu=0.15^*$	10
<b>2D+1</b> <b>two-step method</b>	CG		9	
<b>2D+1</b> <b>two-step method</b>	SA-POS +	34.9	3	11
<b>2D+1</b> <b>two-step method</b>	CG		10	
<b>2D+1</b> <b>two-step method</b>	EM +	34.8	5	10
<b>2D+1</b>	CG		9	
<b>2D+1</b>	CG	34.4	16	17
<b>2D+1</b>	EM	34.7	110	111
<b>2D+1</b>	EM-OS12	34.6	9	10
<b>Fully 3D</b>	CG	34.5	15	232

Table 3 Comparison in reconstruction accuracy and timing requirements among the 2D, SI-PSF, 2D+1 and 3D models. The unit in which the timing requirements are expressed corresponds to the time required by one 2D+1 CG iteration. In all computations, voxel-driven projector-backprojector pairs were used, except for the case of the SI-PSF model, where the strategy of rotating the emission matrix was adopted.

---

\* Since the Tikhonov method is not iterative, instead of reporting here the optimal iteration number, we report the optimal value of the regularization parameter  $\mu$  (see [Tik63a, Tik63b, Tik77] for more details about the significance of this parameter).

## Visual Inspection

CG reconstructions of the phantom based on different projectors are shown in Figure 22 (transaxial sections) and in Figure 23 (sagittal and coronal sections). The number of iterations performed for each case is the one leading to the minimum relative error between the reconstruction and the original phantom, as will be discussed with more detail below. In all figures, a section of the original Hoffman phantom is shown in the top left, whereas the corresponding sections of the 2D+1, 3D and SI-PSF reconstructions are shown to its right, below and in the bottom right corner, respectively.

The differences between the three models are minimal and hard to detect if an accurate investigation is not performed. The major ones are basically visible by confronting the SI-PSF against the other approaches - surprisingly, mainly in the transaxial section, rather than in the sagittal or coronal ones, in which the non modelling of the blur in the  $z$  extent was mostly expected to affect the reconstructions. These differences are reported in terms of some anatomical details that are roughly recovered by both the 2D+1 and the 3D model, but which are missed by the 2D one.

Despite the appearance of these details as being almost neglectable, the benefits of the 2D+1 and the 3D approaches are, in general, well appreciated by the nuclear medicine staff members of our department, when comparing them with the 2D approach, all of them applied to real clinical data. One major reason for this might lie in the fact that the counts acquired in a brain scan can easily exceed the 7 Mcount level selected for our simulation.

In order to address situations where the signal-to-noise ratio has higher values, we also computed reconstructions of noiseless projections of the same brain phantom. This is equivalent to an idealized situation where the count density is extremely high. An evaluation of the results obtained over over 100 iterations of the CG algorithm

with both 3D, 2D+1 and SI-PSF models confirmed the hypothesis above. In particular, a weak advantage (0.5% in terms of the Relative Error discussed below) of the 3D model over the 2D+1 one can be observed starting from 40 – 50 iterations, but it remains quite steady all the way thereafter. For the SI-PSF model, the more the signal-to-noise ratio increases, the easier the aftermath of an approximation in the model of collimator blur can be noticed, with respect to the 2D+1 and the 3D methods. Further details about these simulations are to be found in [Boc99].

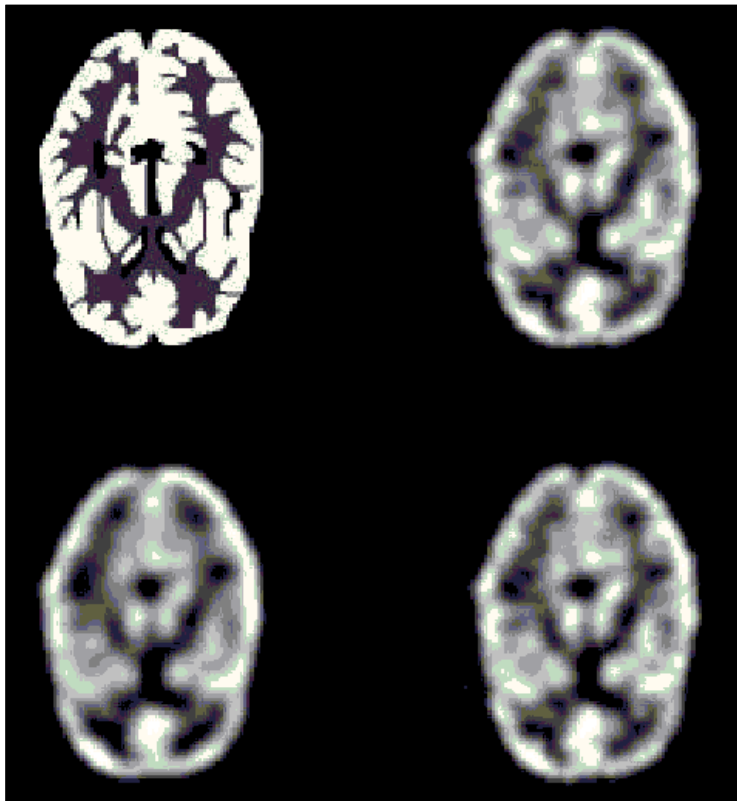


Figure 22: A transaxial section of the phantom (top left) is compared with the corresponding views cut from the reconstructions produced by the 2D+1 approximation (top right, 16 CG iterations), by the fully 3D model (bottom right, 15 CG iterations) and by the SI-PSF approach (bottom left, 15 CG iterations).

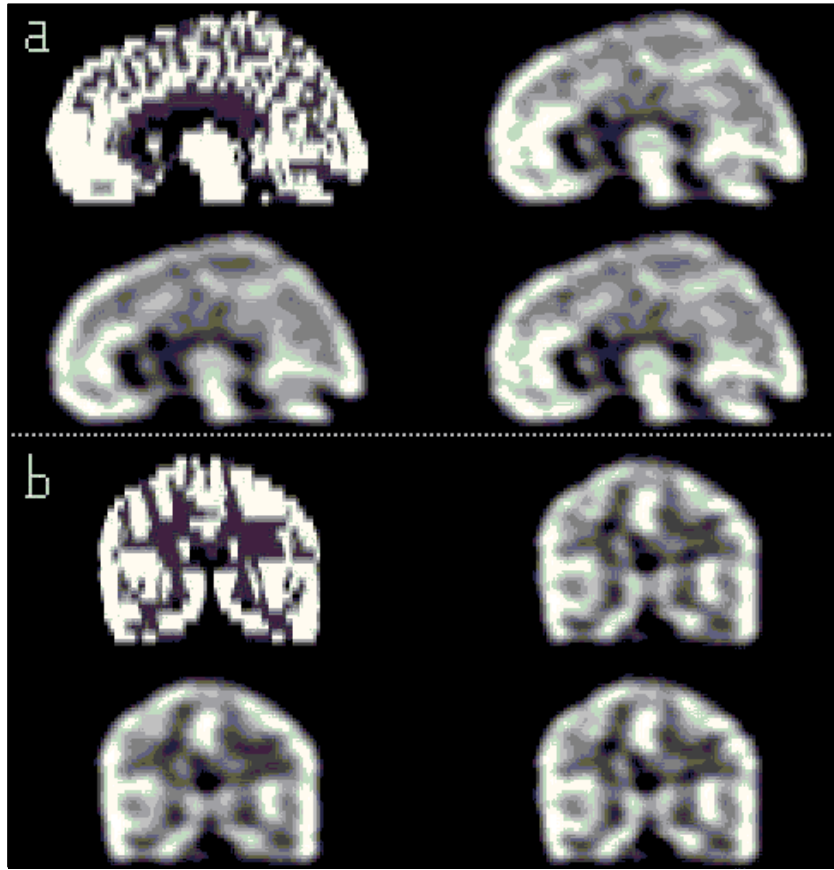


Figure 23: a) A sagittal and b) the respective coronal view of the phantom (top left) and, in clockwise rotation, the corresponding 2D+1, fully 3D and SI-PSF CG reconstructions.

### Relative error

In order to have a quantitative estimate of how accurately images can be obtained by means of the 2D+1 model as opposed to others, we computed the relative error (RE) of the reconstructions  $[f]$  with respect to the original brain phantom  $[f]_{ph}$ , that was suitably scaled to the appropriate count number. Such RE values, given by

$$RE = \frac{\| [f] - [f]_{ph} \|}{\| [f]_{ph} \|},$$

were computed for the reconstructions obtained by each model in conjunction with each algorithm as described above, and for different iteration numbers of the algorithms themselves.

Part of the results are plotted in Figure 24. Here, we omitted the EM method because its optimal iteration number (110) is rather out of scale with the convergence values of the other methods. Among the two-step algorithms, we only plotted the values related to the EM+CG, which provides the best performance in terms of accuracy.

Among the CG reconstructions, the 2D+1 and the 3D are almost equivalent in terms of optimal iteration number and accuracy. At lower iterations, the 3D model slightly outperforms the 2D+1 – the error being so small though, that it can be considered negligible in the clinical routine. At higher iterations, the 2D+1 features a slightly more stable behavior and, definitely, a smaller error. In the case of the S-PSF model, the same curve is obtained by the 2D+1 and the 3D implementations of the same computation.

Rather interesting results are those provided by the EM-OS12 algorithm in conjunction with the 2D+1 model: an extremely low optimal iteration number and a quite stable behavior in the neighborhood of the best iterate. Comparable results, both in terms of accuracy and timing requirements, can be expected from EM-OS10 and EM-OS15.

As far as the two-step scheme is concerned, a few elucidations are necessary in order to interpret the long-dashed curve of Figure 24. In this case, the semiconvergence behavior is plotted against the number of iterations relative to the CG algorithm, i.e. the second step of the scheme, namely, the reconstruction of the deblurred sinograms: the time required for the first step to be performed is neglectable. Similarly, the RE is computed over the final reconstructions, i.e. over the results obtained after execution of both steps.

However, an evaluation of the intermediate results and of the behavior of the first step separately might also be interesting. For this purpose, we generated synthetic projections of the brain phantom by means of a customization of the 2D projector to the CERASPECT system. This way, the ‘true’ 2D projections were obtained and they represented the reference point for exploiting the semiconvergence property of the deblurring process. We computed both the ‘optimal’ value of the regularization parameter (the ‘optimal’ number of iterations respectively, depending on the algorithm being used) and the correspondent RE, relative to the first inversion step: these values are reported in Table 3 as the first entries in each of the rows relative to the two step methods. As a side issue, the ‘optimal’ values determined in this way are supposedly suitable for the reconstruction of experimental data as well.

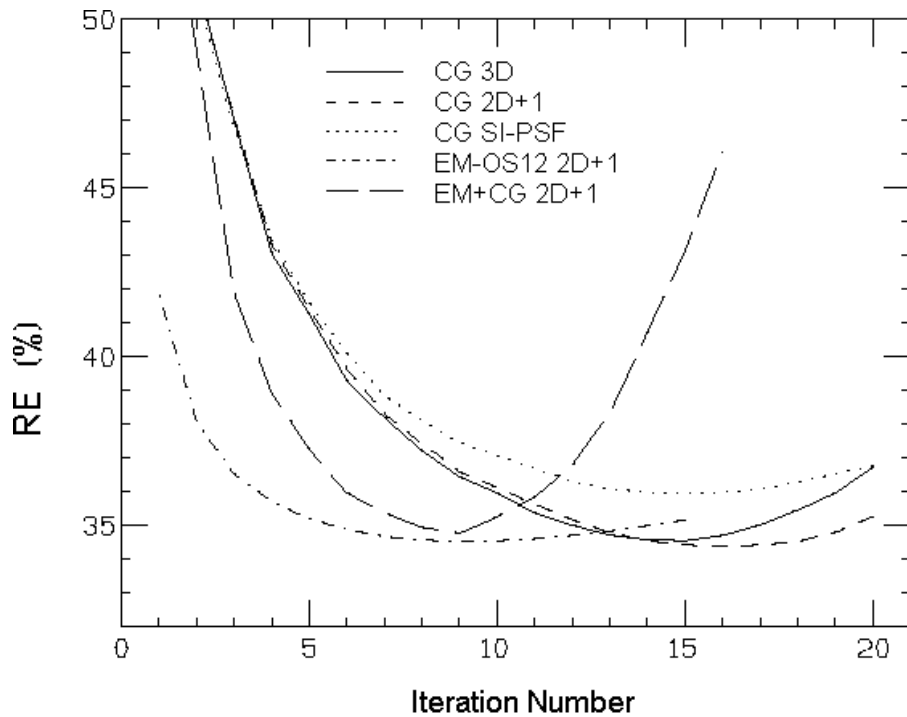


Figure 24: Plot of the RE (in %) of the reconstructions performed in the simulation study with different projectors, as a function of the iteration number.

### **Relative error over an image partition**

Based on the relative error expression defined above, we performed a different kind of quantitative evaluation, with the aim of specifically addressing the advantages of the 3D approaches that model the collimator blur over the simpler 2D ones. The idea was to gain more spatial information on the quality of the reconstructions and further insight into the nature of the error, by computing it separately over five non-overlapping regions of the images. The regions were concentric, axial cylinders, centered on the z-axis, having an elliptical section, with a radius was that chosen so that the average number of counts in each region was the same. The outermost ellipse would loosely fit the phantom contour in its caudal slices. A single RE value was computed for each region in the 'optimal' GC reconstruction for the 2D, the 3D, and the SI-PSF models, respectively. These values are plotted in Figure 25. It is evident that, in the case of noisy data, the approaches that accurately model collimator blur offer a better recovery of the outermost parts of the phantom. Since these parts correspond to the location of the brain cortex in real patient images, we conclude that an accurate modelling of the collimator blur is important in the reconstruction of clinical data.

### **Computational cost**

In addition to the quality of the reconstructions, another fundamental discrimination parameter for choosing one algorithm over another is the time required to obtain the 'optimal' result. This factor is reported in Table 3 for each method considered in this study and it is expressed in terms of a unit corresponding to the time required by one 2D+1 CG iteration. Considering the processing power available at the time we ran our simulations, this unit was about 15 min on a 64 Mb RAM, 133 MHz Pentium running Linux, and less than 2 min. on a Digital AlphaStation with 433 MHz CPU running on DEC-Unix.

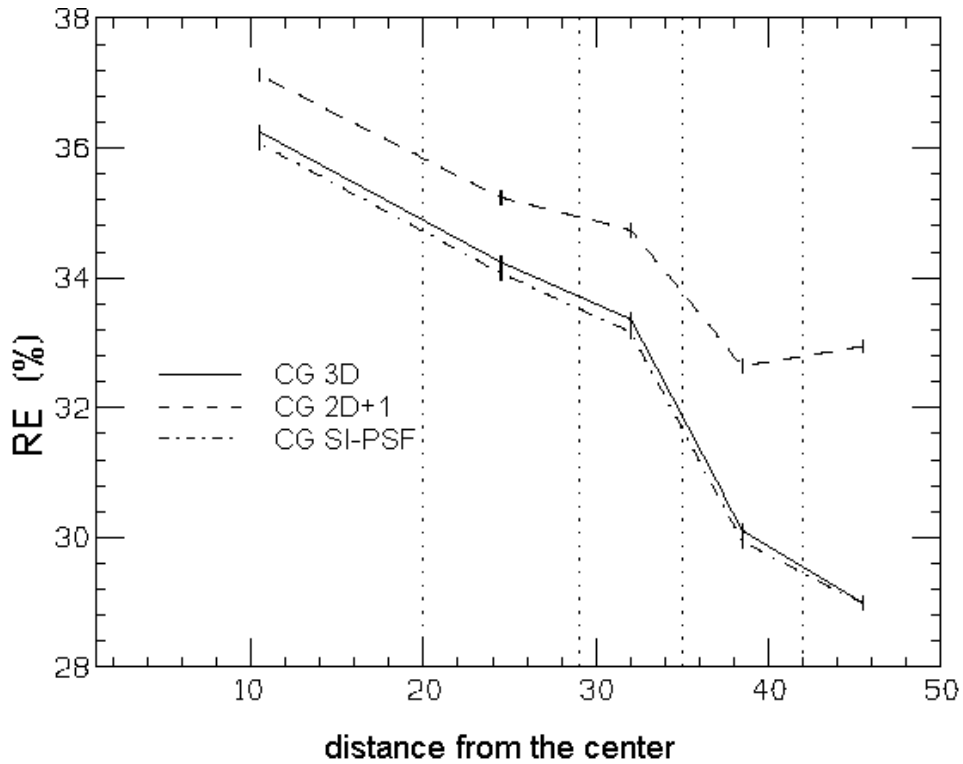


Figure 25: Plot of the RE values (in %) relative to five concentric isocount regions into which the whole phantom volume was partitioned. The points are located halfway between region boundaries. Distances from the center are measured in pixels along the major axes of the ellipses.

Generally speaking, in the context of iterative methods, the computational complexity is given by the product of two major factors: the optimal number of iterations and the time required to perform a single iteration.

The first of these factors has already been discussed above, when analyzing the minimum relative error for different combinations of projection models and reconstruction algorithms. The values for each method, along with the corresponding RE, are summarized in Table 3.

Concerning the second factor, an estimate of the time required for one iteration by each method can easily be obtained from the values reported in the two right columns of the same table<sup>11</sup>:

$$232/(15+1) = 14.5 \text{ time units for a fully 3D CG iteration}$$

$$44/(15+1) = 2.75 \text{ time units for a 3D CG iteration with the rotational technique}$$

$$10/(15+1) = 0.625 \text{ time units for a 2D+1 CG iteration with rotational technique}$$

$$1 \text{ time unit for a 2D+1 CG iteration}$$

Hence, in terms of computational costs, the 2D+1 model outperforms the fully 3D one by a factor of about 14 in the case of voxel-driven projectors and by a factor of about 4 in the case of rotational technique.

Analogous conclusions can also be drawn for EMOS and the two-step algorithms. In the latter case, it is important to point out that the cost required by the first step is almost neglectable and the reasoning above is to be applied to the reconstruction phase performed in the second step.

---

<sup>11</sup> On all platforms we tested, the total computational time was in the order of the number of iterations performed, plus one: this offset is due to the necessary initializations that are performed once only, before the actual loop of projection-backprojection sequence is entered - in the case of CG, the preconditioner has to be generated, whereas, in the case of EM-OS, normalization masks have to be created.

## Statistical framework

Deterministic approaches to image reconstruction do not take into account the presence of noise in the data. For this reasons such approaches are not well suitable when the SNR is not high, as is the case of PET and SPECT: here, the low photon counting statistics should be explicitly considered when formulating the mathematical model by extending the latter to both the physics of the detection and the statistical fluctuations due to the random nature of the radioactive decay. This can be done by formulating the tomographic inverse problem in terms of classical estimation techniques using statistical models of the data, whereby image reconstruction involves maximizing a certain probability of interest.

The major assumption of statistical methods is that the projection measurements are always affected by some statistical variation due to the random nature of the noise and, hence, they are different every time, even when the object remains the same. Any type of statistical property of the noise that is known, such as expectation, correlation or distribution, can be used for the reconstruction of the image. However, different assumptions about the randomness inherent in the data can be made and hence the reconstruction approaches differ in their structure. They can be broadly divided into two main classes: *Maximum Likelihood (ML)* and *Bayesian* methods.

### Maximum Likelihood methods

Maximum Likelihood methods assume the object to be deterministic and treat the image only as probabilistic, due to the presence of noise. The mapping of data and object in the discrete case is mathematically modeled as

$$\mathbf{g} = \mathbf{P}\mathbf{f} + \mathbf{w} \quad (27)$$

where  $\mathbf{f}$  is the deterministic object to be imaged and  $\mathbf{P}$  is the projection matrix: it relates image and data by modelling the probability  $P_{ij}$  of detecting an emission from voxel site  $j$  at detector element  $i$ . The particular form depends on the specific device geometry and other factors, as described for instance in [Boc99] for the case of SPECT and [Qi98a] for PET. We will take a closer look to the formation of such a matrix in the case of PET in the next section.

$\mathbf{w}$  is a noise term and its components are a realization of a random vector. Hence, also the data  $\mathbf{g}$  is composed by elements that are the realization of a random vector. For simplicity, let us here denote by  $\mathbf{g}$  the random vector itself and, likewise, let  $\mathbf{w}$  represent a vector-valued random variable.

In low-count tomography, it is reasonable to model the data as a collection of independent Poisson random variables, since these - in contrast with, for instance, Gaussian variables - reflect how the variance of the measurements increases with the expected number of counts. If we denote their mean by  $E[g_i]$ , then their conditional probability given the image coefficient, or likelihood, is:

$$p(\mathbf{g} | \mathbf{f}) = \prod_i \frac{E[g_i]^{g_i} e^{-E(g_i)}}{g_i!} \quad (28)$$

The physical model for the detection system, embedded in matrix  $\mathbf{P}$ , is included in the mapping from the image  $\mathbf{f}$  to the mean  $E[g_i]$  of the detected events as will be shown below. When the data is modeled according to a collection of Poisson distributions, the photon or quantum noise  $\mathbf{w} = \mathbf{g} - \mathbf{P}\mathbf{f}$  is sometimes referred to as *Poisson noise*.

In emission tomography the mean  $E[\mathbf{g}]$  of the data can be estimated as

$$E[\mathbf{g}] = \mathbf{P}\mathbf{f}$$

which, with reference to equation (27), evidences the implicit assumption that  $E[\mathbf{w}] = 0$ .

It might be useful to also express the mean of the data in the case of transmission tomography. As a matter of fact, SPECT and PET can also be operated in transmission mode: these measurements are used to correct for attenuation in the emission studies. In the transmission case, the element  $P_{ij}$  of matrix  $\mathbf{P}$  represents the probability of attenuation in voxel  $j$  of a photon that would otherwise be detected by the  $i$ -th detector. If we assume the source intensity to be constant and denote it by  $a$ , then the mean  $E[g_i]$  of the  $i$ -th element of the transmission data  $g_i$  is [Mum94]

$$E[g_i] = ae^{-\sum_j P_{ij} f_j}.$$

The ML solution is found as the maximum of  $p(\mathbf{g}|\mathbf{f})$ , the conditional probability of the data  $\mathbf{g}$  given the image  $\mathbf{f}$ : the image that maximizes the likelihood is the one for which the data is most likely. Often, it is more convenient to work with the logarithm  $L(\mathbf{g}|\mathbf{f})$  of the likelihood, so that the ML solution is computed as the maximizer of

$$L(\mathbf{g}|\mathbf{f}) = \sum_j g_j \log(E[g_j]) - E[g_j] \quad (29)$$

which is derived from equation (28) by simply applying the logarithm to both sides of the equation.

When the data is modeled according to a Poisson distribution as shown above, one of the most popular examples of ML methods is the EM algorithm developed by Shepp and Vardi [She82] and briefly described in section 2.3.4. This method outperforms direct or iterative linear techniques in terms of quality of the reconstruction because it models the spatially variant fluctuations in the process of photon countings. However, it presents the disadvantage of having an ill-conditioned solution in PET and SPECT, which results in high variance reconstructions. Such an instability is usually controlled by early termination of the iterative process.

Another disadvantage of EM, namely its slow convergence rate, is addressed by variants of this algorithm, the most popular being i) the Ordered Subset (OSEM) [Hud94], mentioned in section 0, that belongs to the class of block iterative

algorithms [Byr97] and, ii) the Row-Action Maximum Likelihood Algorithm (RAMLA) developed by Browne and De Pierro [Bro96]. In contrast with OSEM, under certain conditions RAMLA converges to a true ML solution. Other approaches to the ML computation include gradient-based methods that, however, do not impose a natural non-negativity constraint on the solution as is the case of EM and OSEM [Kau93], and Iterated Coordinate Ascent (ICA) methods that lead to dramatic speed up in convergence rate in comparison to the EM algorithm [Sau93].

### Bayesian methods

An alternative way to avoid the sensitivity of the ML method to perturbations in the data is to introduce some form of *a priori* information about the unknown object, representing a regularizing factor<sup>12</sup>. In the simplest case, *a priori* information can take the form of rigid or deterministic constraints, requiring that the solutions belong to some fixed domain in the object space. More complex forms of *a priori* information can be introduced by assuming that the unknown object is a value of a random vector, whose density function is given. In such cases the problem can be reformulated in a Bayesian framework, since Bayes theorem provides a means for merging all statistical terms into one single model. The posterior probability for the image conditioned on the data is given by:

$$p(\mathbf{f} | \mathbf{g}) = \frac{p(\mathbf{g} | \mathbf{f})p(\mathbf{f})}{p(\mathbf{g})}. \quad (30)$$

$p(\mathbf{f})$  is the prior distribution. Mathematically, it represents a regularizing factor of the ML method; physically, it models the known statistical properties of the object. Since these are, in general, local properties, they can be well modeled by Markov random fields (MRF) [Gem85]. More specifically, one can express the densities of the MRF and, hence, the prior itself in terms of a Gibbs energy function, i.e. a sum over a set

---

<sup>12</sup> Such regularization procedures are sometimes presented as a penalized ML methods, the difference being mainly only a matter of terminology.

of potential functions defined on neighboring pairs of pixels that reflect the locally smooth properties of several images.

More complex MRF can be used to model the edges of objects that result in sharp intensity changes: these include the generalized  $p$ -Gaussian model proposed by Bouman and Sauer [Bou96] and the Huber prior [Qi98a], that show a similar behaviour. While these examples both produce convex energy functions, non convex functions have been proposed in an attempt to model even sharper intensity transitions [Gem85, Gin93].

It is interesting to observe the relation between the Bayesian formulation given by equation (30) and the ML model: since the probability  $p(\mathbf{g})$  is a constant for each data set, the posterior probability  $p(\mathbf{f}|\mathbf{g})$  is a function of both the likelihood and the prior. This is better evidenced by taking the logarithm of both sides of equation (30) in a similar way as was done for the ML method and comparing the result with equation (29).

Bayesian estimators in tomography, which, from a computational point of view, are, in general, rather heavy to determine, are usually of the Expectation a Posteriori<sup>13</sup> type and, more commonly, of the Maximum a Posteriori (MAP) type. Since the second part of this thesis is based on PET data reconstructed with a MAP algorithm, we will devote a more detailed discussion to such method in the following section.

---

<sup>13</sup> The solution is found as the estimate provided by the *a posteriori* expectation value of the unknown object.

## Maximum A Posteriori

Here, we present a specific implementation of the MAP algorithm developed by R. M. Leahy and J. Qi for the reconstruction of PET images [Lea00, Qi98c]. Both a Siemens/CTI ECAT EXACT HR+ 962 system<sup>14</sup> [Qi98b] and a MicroPET scanner for small animals [Qi98a] were considered in the description of the system model. The model features a factored structure in order to reduce storage and computational costs. Compensation for attenuation, scatter and random is also addressed. MAP solutions are computed using a pre-conditioned conjugate gradient method on this model combined with a Poisson likelihood function and a Gibbs prior [Zho97] into a Bayesian formulation [Mum96, Mum99].

### The inverse problem

As we have seen, the posterior density  $p(\mathbf{f}|\mathbf{g})$  is expressed by combining the likelihood function  $p(\mathbf{g}|\mathbf{f})$  of equation (28) and the image prior  $p(\mathbf{f})$  through Bayes rule as defined in equation (30). The MAP estimate of the image is the maximizer of the posterior and it is usually computed on an objective function  $\Phi(\mathbf{f}|\mathbf{g})$  that is given by the log of the posterior:

$$\Phi(\mathbf{f} | \mathbf{g}) = \log(p(\mathbf{f} | \mathbf{g})) = \log(p(\mathbf{g} | \mathbf{f})) + \log(p(\mathbf{f})) - \log(p(\mathbf{g})) \quad (31)$$

The first term on the right hand side of equation (31) is the objective function of the ML method, denoted  $L(\mathbf{g}|\mathbf{f})$  in equation (29). We assume that the data can be represented as a set of independent Poisson random variables with mean  $E[\mathbf{g}]$ , so that the expression for the likelihood is the one given above.

The second term is a function of the prior that we model here by a Gibbs distribution because this presents some convenient Markovian properties. Such a distribution has the general form

---

<sup>14</sup> This is the instrument we will refer to in the next part of this thesis.

$$p(\mathbf{f} | \beta) = \frac{1}{Z} e^{-\beta U(\mathbf{f})}$$

where  $Z$  is a normalizing constant or partitioning function,  $\beta$  is the hyperparameter that influences the degree of smoothness of the estimated image and  $U(x)$  is the Gibbs energy function. We will discuss the form of such a function shortly. The logarithm of a Gibbs prior is thus simply given by  $-\beta U(\mathbf{f})$ .

The last term of equation (31) is a constant and thus it can be dropped off when computing the estimate that maximizes the log of the posterior.

In summary, the objective function reduces to

$$\Phi(\mathbf{f} | \mathbf{g}) = L(\mathbf{g} | \mathbf{f}) - \beta U(\mathbf{f})$$

that better points out the role of the smoothing parameter  $\beta$ .

Since the log likelihood functions are concave, if the Gibbs energy is convex  $\Phi(\mathbf{f}|\mathbf{g})$  will also be concave and a global maximum can be found using standard nonlinear optimization methods; otherwise, local searches for a stationary point of the objective function can be used to find a local maximum - global searches being usually impractical because of the remarkably large number of voxels in PET reconstructions [Qi98c].

The Gibbs energy functions considered in this MAP implementation have the general form of a sum of potentials, each being a function of a subset of voxels. Such a subset is typically the collection of voxels closest, in terms of some Euclidean distance, to some given voxel. The collection of subsets defines a neighborhood system which must satisfy the property that each two voxels are mutual neighbors. In a 2D problem, the neighbors of a given voxel would be the nearest 4 in a 1<sup>st</sup> order model and the 8 surrounding voxels in a 2<sup>nd</sup> order model. Likewise, in a 3D problem, a 1<sup>st</sup> order model would refer to the 6 nearest voxels and a 2<sup>nd</sup> order one to the 26 closest voxels. The most common potentials in image processing are defined on pair-wise cliques of neighboring voxels: The potentials must reflect the smooth variations in tracer uptake within a specific organ or tissue

type and, at the same time, the edges and abrupt changes between different organs or type of tissue. Several different potentials have been suggested [Cha95, Gem84, Gre90, Lea91, Lee95], all aiming at finding the best compromise between these two conflicting requirements and all having the property of being monothonic non-decreasing functions of the absolute intensity difference. Different potential functions were considered in this implementation of the MAP scheme including a quadratic and a Huber one [Qi98a].

### Data modeling

As mentioned with reference to the ML method, the physical model for the detection system is included in the mapping from the image  $\mathbf{f}$  to the mean of the detected events  $E[\mathbf{g}]$  used to compute the likelihood. Here, we express the mapping between the unknown parameters, namely, the emission intensities in each pixel, and the mean of the data by a slightly more accurate transform than the one above that also includes the effects of randoms and scatters:

$$E[\mathbf{g}] = \mathbf{P}\mathbf{f} + \mathbf{r} + \mathbf{s}.$$

Let us take a closer look to the three terms  $\mathbf{P}$ ,  $\mathbf{r}$  and  $\mathbf{s}$ .

$\mathbf{P}$  is the detection probability matrix, whose elements  $P_{ij}$  denote the probability of detecting an emission from pixel site  $j$  at detector pair  $i$ . In an attempt to develop an accurate, clear and efficient model the matrix has been factorized as follows:

$$\mathbf{P} = \mathbf{P}_{\text{detect}} \mathbf{P}_{\text{attn}} \mathbf{P}_{\text{geom}} \mathbf{P}_{\text{positron}} \quad (32)$$

$\mathbf{P}_{\text{positron}}$  is a local image blurring operator that is applied to the true source distribution. It models the blur due to the small distance covered by the emitted positrons before they annihilate with an electron. The distance depends on both the isotope of the compound used and the type of tissue traversed by the positron.

Since this kind of blurring is neglectable compared to other factors, we have only modeled it in the mathematical expression but we have not considered it in the software implementation of our MAP algorithm.

$\mathbf{P}_{\text{geom}}$  describes the geometrical mapping between the source and the data and it also includes the effects of uncertainties in the angular separation of the photon pair produced by annihilation. The  $(i,j)^{\text{th}}$  element represents the probability that a photon pair produced in voxel  $j$  reaches the front faces of detector pair  $i$  in the absence of an attenuating medium. Instead of computing this probability by considering the intersection of a tube joining the detector pair with each voxel, as is usually done, here the solid angle is considered that is subtended at each of the detectors by each voxel: this angle is numerically integrated over the volume of each voxel in order to account for finite voxel size [Qi98a].

The matrix encoding exploits several rotation and reflection symmetry properties, and additional symmetries between rings in the 3D case [Che91, Joh95], as well as the sparseness that arises from the small fraction of voxels that produce coincidences at each detector pair. Since the multiplication by  $\mathbf{P}_{\text{geom}}$  represents one of the major computational bottlenecks of the forward and backprojection processes, such an efficient representation remarkably reduces both the spatial and the computational complexity of the entire reconstruction algorithm [Qi98a, Qi98c].

$\mathbf{P}_{\text{attn}}$  is a diagonal matrix that contains the attenuation correction factors. It models the fact that one or both photons might be scattered while traveling towards the detectors and thus lose energy and change direction. This results in a loss of counts along the path in which they were originally travelling. The probability of attenuation along any given straight line path is independent of the location, along that specific path, in which the annihilation took place. This is the reason why the matrix has a diagonal form.

The attenuation factors can be computed in different ways. The most common require the acquisition of transmission data and assume that transmitted and

emitted photons are attenuated with the same probability. Transmission data can then be used to reconstruct an image of the linear attenuation coefficient via statistical methods [Fes97, Mum94, Lan87]. Alternatively, they can be used in conjunction with a blank scan: an estimate of the probability of survival photons is obtained as the ratio of the number of photons detected with the presence of the attenuating medium and the number of photons collected without any attenuating medium.

$\mathbf{P}_{\text{detector}}$  is a banded square matrix that is applied to the sinogram. It includes all factors related to the detectors: intrinsic and geometrical sensitivity of each detector that can be measured through calibration procedures and that could be factored out of  $\mathbf{P}_{\text{detector}}$  into a separate, diagonal matrix; crystal penetration due to the fact that the crystal surface is not always exactly orthogonal to the arrival direction of the photons; intercrystal scatter that results in a mispositioning of the detected photons; system deadtime, a complicate factor since it causes non-linear behavior at high count rates; and, finally, the non collinearity of photon pairs. Once again a reduction in storage and computational time can be achieved by exploiting several symmetry properties.

The term  $r$  in equation (32) represents the mean of the random events. Randoms are a form of additive noise that corrupts the data. They are caused by pair of photons being collected within the same timing windows but originating from different locations. When operated in standard mode, PET scanners automatically precorrect for randoms during data acquisition by subtracting a randoms sinogram from the transmission coincidence sinogram. The former is collected using a delayed coincidence circuit with the same resolving time as that of the coincidence sinogram. However, while this process corrects the data in mean, it also increases their variance due to the subtraction of two Poisson processes. Hence, a Poisson model as described above does not reflect the true variance any more. Several

methods have been proposed to deal with randoms [Lea91, Mum94, Pol91]. Our implementation is based on a shifted Poisson model [Qi98c, Yav96].

The last term of equation (32),  $\mathbf{s}$ , is the mean of the scatter events. Since scattered photons have a lower energy than unscattered ones they could theoretically be removed from the data by rejecting those events whose energy is below a certain threshold. However, due to the poor energy resolution of the detectors, this would result in a loss of true coincidences as well.

The usual approaches to deal with this kind of noise in the data are based on the assumption that scattered events have a fairly uniform distribution and the scatter sinogram is generally smooth and robust to small variations in the image. Thus, in qualitative studies scatter contribution can simply be ignored. Since our implementation aims at providing an accurate estimate of the object also from a quantitative point of view, the scatter profile is here computed preliminarily using the Klein-Nishina distribution for Compton scatter [Bar81] and then treated as an offset in the mean of the data in the likelihood. More sophisticated methods [Dau92, Mum92, Oll92, Wat95] model this term as an explicit function of the data, but in this way it needs to be re-computed at each new estimate of the image: such a procedure turns out to be highly time consuming, if not even impractical, from a computational point of view.

### **Computation of the MAP estimate**

Several methods have been proposed to compute the maximum of functionals with continuous derivatives. Although they differ in the way they reach the solution, all of them – with only a few exceptions – will ultimately converge to the same result. Since we already have presented most of them in section 0 we will here mention only the major issues that arise when implementing such algorithms in conjunction with a MAP model.

The most popular approach is to use some form of gradient ascent as, for instance, the steepest ascent, Newton's method, or the conjugate gradient.

The major problem associated with these methods is that they are designed for the maximization of an unconstrained functional. MAP solutions, however, have to be non-negative. Several attempts to incorporate such a constraint have been proposed, the most efficient being the use of restricted line searches [Kau87], bent line searches [Kau87], penalty function methods [Lue84, Mum94], active set approaches [Kau93, Mum96], and coordinate-wise updates [Bou96, Fes94, Sau93].

An important issue related to the conjugate gradient method is the use of appropriate preconditioners to achieve a faster convergence rate: when a preconditioner is used the convergence properties of the CG method depend on the eigenstructure of the matrix obtained as the product of the preconditioner and the Hessian of the original posterior probability, instead of on the Hessian only. We refer to [Cli93, Lan87, Mum94] and to [Kau87, Lan87] for further details about the preconditioners that can be used in the case of transmission and emission reconstruction respectively, since these are the models on which our MAP implementation is based. In [Mum94] a numerical method for computing the MAP estimate is described that combines pre-conditioned CG with a penalty function to impose a non-negativity constraint.

Coordinate-wise optimization methods [Bou96, Fes94, Sau93] deal very well with the non-negativity constraint, because they update each voxel in turn so as to maximize the objective function with respect to that voxel. However, since one complete iteration through the image requires the re-application of the blurring kernels each time a different pixel forward projects to a particular sinogram element, the computation cost results fairly high.

Mean field annealing techniques have been proposed in [Gin93] and [Lea00] to be combined with any of the other techniques when compound Gibbs priors that involve line-processes are used.

The EM algorithm can be extended to include a prior term [Gin93] and hence maximize equation (31). Like the preconditioned conjugate gradient, and in contrast to coordinate-wise methods, such a technique allows to fully take advantage of the savings in storage and computational costs of the factored matrix approach, because it considers all data and all pixels at each iteration. However, this algorithm suffers from the same slow convergence problem as the standard version.

An interesting compromise between the two above mentioned requirements, namely, taking advantage of the efficiency offered by the factored matrix approach and, at the same time, achieving a fast convergence rate, is achieved by a special adaptation of the OSEM algorithm. Since this method couples sinogram elements through the blurring kernels, the advantages of the factored matrix approach would theoretically be lost. However, by approximating the blurring kernels as a 1D radial-only blurring function, one can use OSEM with the factored system model without losing any computational efficiency [Qi98a, Qi98b].

### **Evaluation of the MAP method**

Several experiments and studies were conducted by our group to validate the efficiency of our MAP implementation for PET reconstruction, also comparing it with different approaches. While we will deal with qualitative evaluations with more detail in the next part of this thesis we summarize here the major results of the work performed to quantify the quality of the reconstructions in terms of classical measures of estimator bias and variance, resolution, and contrast recovery.

Several experimental studies were carried out covering a wide range of conditions and possibilities: both phantom and in vivo animal and human experiments in both 2D and 3D modality were performed on different PET devices, including the Siemens/CTI ECAT931 [Mum94, Mum96] the EXACT HR+ [Hsu98, Hsu98t, Qi98b] and the microPET scanner [Cha99, Cha00, Lea99, Qi98a]. On the MicroPET scanner, resolution, contrast recovery and noise were measured using point sources, cylindrical phantoms and a small monkey brain phantom. The MAP algorithm was compared with other algorithms, including FBP and OSEM. Under all conditions MAP showed to perform best. This can be mainly attributed to the accurate modeling of the statistical and physical properties of the system.

Beyond the experimental studies also some useful theoretical results were derived that allow to accurately characterize the resolution and noise properties of MAP images [Lea99, Qi99a, Qi99b, Qi00]. They are based on the computation of the local impulse response of the reconstruction and the image covariance. By further developing this basic idea, compensation for spatially-variant resolution was also achieved [Qi00], so that the reconstructed images have a uniform resolution. Furthermore, as will be shown in later chapters, this very same idea will represent the basis of an efficient theoretical model for lesion detection with computer observers [Bon00].

We conclude this section by remarking that we have implemented a multithread version of the MAP algorithm. This implementation computes the results by taking full advantage of the hardware resources of multiprocessor machines and thus results in being computationally very efficient. The details are overviewed in Appendix a. In Appendix b, the graphical interface is shown that we have developed for a Windows operating system in order to facilitate the use of the software by non-experts.

## **3. Image quality assessment**

We have presented methods to reconstruct an estimate – in the form of an image - of some human or animal organ, or anatomy, given a collection of data acquired over it by a tomographic device. To follow up, we would like to evaluate the quality of these images and gain feedback about the accuracy of the reconstructions.

As was the case of the first part of this dissertation, the overview is intended to provide the general notions regarding the concept of image quality and assessment. The most popular tools to perform evaluation studies are surveyed and attention is then given to two methods in particular, human and computer observers. In the following sections, a deeper insight into these techniques is taken. We will describe two observer studies that we carried out on PET images reconstructed by the MAP algorithm introduced in the previous part.

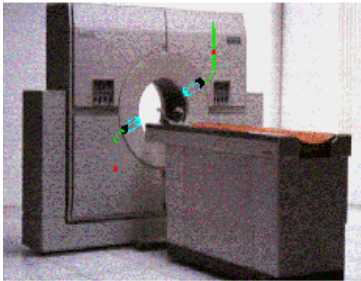
### **3.1. Overview**

#### **3.1.1. Methods to evaluate image quality**

As we have seen, the process of image formation involves several steps, the basic of which are sketched in Figure 26. Although both the technology and the mathematical models utilized throughout have seen remarkable improvements in recent years, leading to extremely accurate representations of the object analyzed, the final result is far from being “ideal”: the reconstructed images are not the exact copy of the object, but rather only a possible estimate of it.



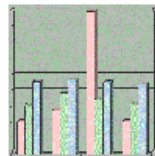
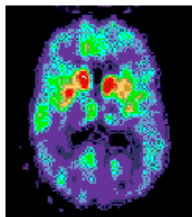
Injection of a radiopharmaceutical into the body to be imaged



Data acquisition



Image reconstruction



Quantitative  
ex: VAR, SNR,  
CRC, COV



Task oriented  
ex: observers

Image quality evaluation

Figure 26: A schematic view of the basic steps involved in the process of image formation.

There are multiple reasons for this, including the physical limitations of the devices, some practical restrictions such as the amount of radiopharmaceutical that can be administered to the patient as well as the duration of the acquisition, and several factors intervening all along the process of image formation that have a random nature and that, thus, can not be modeled exactly but only approximated or estimated - if not even neglected, in an attempt to restrict the computational burdens. Noise, due to the variability in the number of photons reaching the receptors, is one of the major degrading factors.

Beside the efforts to reduce the complexity of the reconstruction procedure both in terms of storage requirements and of computational time, the major focus of research in tomographic imaging is devoted to improving the accuracy of the reconstructions. In order to identify which direction to take to produce “better” results, it is fundamental to precisely define the term “image quality” and develop tools to measure it. In the case of medical images, subjective criteria such as “appearance” are not reliable considering the final use that will be done, and other, more specific methods have to be addressed. These fall into two major categories: those related to quantitative image characteristics, and qualitative, task oriented methods, based on the particular use that is done of the reconstructions.

Before specifically addressing each of the two types of evaluation studies, we would like to point out the importance of also performing simulations, rather than working with real data only, when analyzing the accuracy of reconstruction methods.

In the context of tomography, simulations are usually carried out in one of two basic ways. Instead of a human or animal body, one can use a physical phantom as, for instance, a simple cylinder or any other container, which can be provided with compartments to be filled with different concentrations of radiotracer (See Figure 27) This is inserted into the tomograph and data are acquired with the standard protocols. In this way, the exact shape of the object is known but everything else is executed as in a real clinical study.

Alternatively, one could simulate the entire process of image formation: instead of using a physical object to be scanned, a synthetic object in the form of a 2D or 3D image can be generated<sup>15</sup> and its projections can be computed by a software program that simulates the acquisition performed by the tomograph. Such a program should also account for issues such as the attenuation due to the tissues traversed by the photons, the scatter of photons and other noise factors, in order to compute projections that are as close as possible to those obtained by a real scan. The resulting data can then be processed, i.e. reconstructed, in the regular way. The advantage of this method is that the “ideal” reconstruction is already available because it is given by the initial, synthetic image itself. Such an initial image can be used as a reference point in the evaluation of the reconstruction accuracy: the results of the evaluation studies performed on the reconstructions can be compared with the output of the same studies applied to the initial synthetic object. We will make wide use of this approach in the studies presented in the following sections.

### **Quantitative performance measures**

These kind of studies address image characteristics that can be quantified and measured, such as sharpness or signal to noise ratio. These measures are usually computed by some kind of post-processing software. The most commonly measured quantities include resolution, contrast recovery, bias, and variance, both voxel-wise and over a region of interest.

---

<sup>15</sup> This approach was used in the experiments regarding the 2D+1 projection model described in the first part of this dissertation and it will also be used in the studies described in later sections. A 2D section of a synthetic brain phantom is shown for instance Figure 42, while a 2D chest phantom is illustrated in Figure 41.

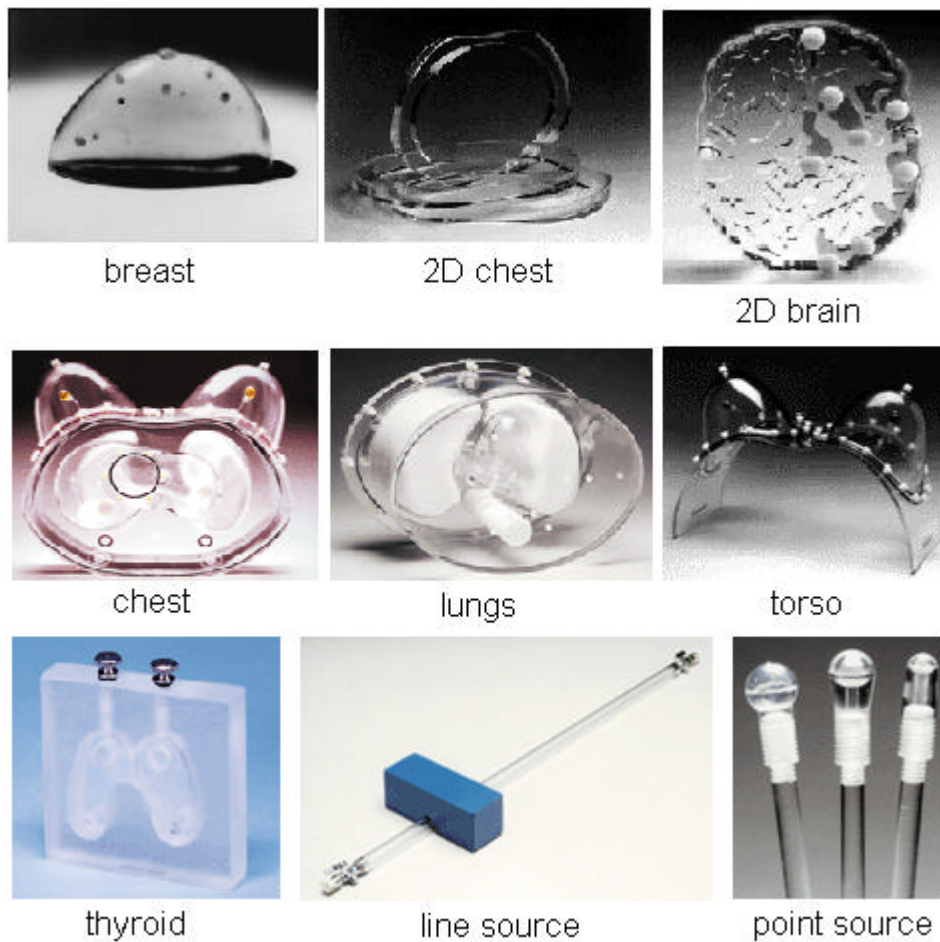


Figure 27: Examples of physical phantoms.

The resolution is related to the ability of the algorithm to reconstruct images with fine details. More technically, it expresses the extent to which two or more points in the original object can be separated in the reconstructed images<sup>16</sup>.

On the other hand, the contrast is related to the relation between a signal and the background. The contrast recovery coefficient (CRC) measures the contrast of a

---

<sup>16</sup> Resolution measurements can be performed using the point source phantom pictured in Figure 27.

signal with respect to the background in a reconstructed image, normalized by the true contrast computed on the phantom.

The concepts underlying the terms resolution and contrast recovery are illustrated in Figure 28. Depending on the properties of the reconstruction algorithm, resolution and CRC can be constant over the entire image volume, or they can vary over the space, in which case they are said to be *spatially shift variant*.

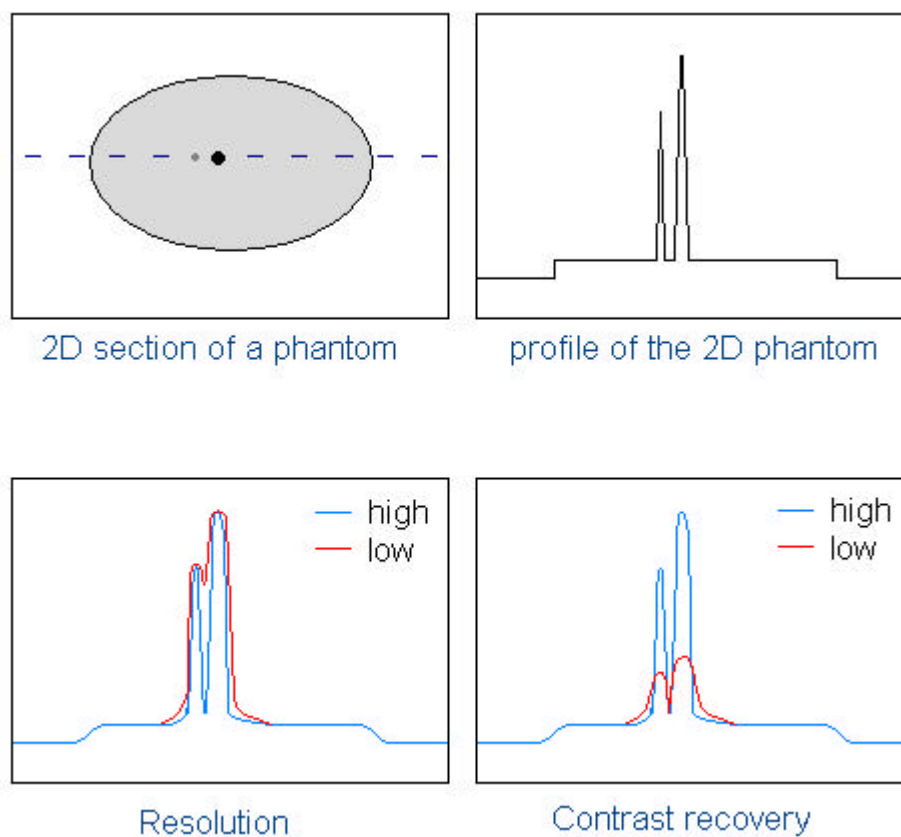


Figure 28: Resolution and Contrast recovery. The top row shows a 2D phantom (left) and its profile (right) along a line intersecting the two points. In the bottom row, the profiles of three different reconstructions are shown. The blue profile has both a high resolution and a high contrast recovery. The red profile on the left features a low resolution and a high contrast recovery, whereas the one on the right has a high resolution, but low contrast recovery.

Two estimators that are strictly connected to resolution and CRC are bias and variance, the latter computable in a voxel-wise manner or over a region of interest. Bias is defined as a systematic error (in contrast to a random error such as the one due to noise). There may be one or more systematic error components contributing to the bias. A larger systematic difference from the reference value is reflected by a larger bias value. Variance, on the other hand, characterizes the dispersion among the measures in a given population. A voxel-wise variance, for instance, is computed over a set of voxels and it expresses how distant are in the average the voxels from the mean of all voxels in the set. Bias and variance of a given type of reconstruction can be estimated directly from the data if the reconstruction algorithm satisfies certain properties, but their computation can turn out to be extremely time consuming for specific kind of reconstruction methods, such as the MAP scheme on which our studies are based. For these cases, some accurate theoretical approximations have been recently proposed.

### **Task specific evaluation**

Qualitative analysis is well founded in the context of radiology: here, image quality is defined in terms of how well a task of diagnostic interest can be performed. In other words, the accuracy of a reconstruction is measured by the performance in a clinical task, using indices that are of more direct clinical relevance than classical measures such as estimator bias and variance.

The first difficulty is choosing the task. Since this should address a major use of the image, it varies depending on the type of image to be considered. The main uses of PET are in cardiology, neurology, and oncology. In the latter case, for instance, PET imaging is an accurate and cost efficient method of establishing the presence of malignancies, their metastatic distribution (staging), recurrence and response to therapy. Hence, for this specific class of images the detection of cancerous lesions is an appropriate task of which to measure the performance in order to gain feedback on the reconstruction accuracy. In this context, the concept of simulation is fundamental because these tests require access to data in which the presence or

absence of lesions can be independently verified, which is virtually impossible in real clinical studies. Moreover, an extremely large number of images has to be considered in order to establish the results with acceptable statistical significance, and artificial generation of data is more straightforward than the acquisition in a medical setting.

Another difficulty is how to measure and how to express the performance in executing the task and, thus, indirectly quantifying the quality of the image. Once again, this strictly depends on the type of task chosen. In the last section of this overview, we will present the currently most popular method to evaluate binary<sup>17</sup> tasks such as the one of lesion detection: the ROC (Receiver Operating Characteristic), and its variant LROC (Localization Receiver Operating Characteristic) for lesion localization studies, along with the associated index AUC (Area Under the Curve). These are the tools we will use in the analysis described in sections 0 and 0.

The last difficulty relates to the choice of whom should execute the task. Since this is a crucial point in detection studies, we will come back to this issue shortly and devote deeper analysis to it.

Semi-quantitative analysis can be performed in conjunction with the visual inspection of images as an aid in deciding on the presence or absence of a lesion. The CRC method introduced earlier as a quantitative performance measurement can also be used for detection, by computing it versus the background noise variance using lesions in simulated or phantom data.

Such semi-quantitative analyses by themselves, do not directly indicate relative detection performance; however, they might indicate performance of other kinds of tasks carried out on PET images, namely tasks based on quantitative clinical applications, such as the uptake of the tracer in a volume of interest. These

---

<sup>17</sup> Lesion detection is a binary task in that the observer has to choose between two possibilities, namely, lesion present or lesion absent.

quantitative measures are used in pharmacokinetic studies and in monitoring disease progression.

### 3.1.2. Observers

Let us now take a closer look at the concept of “observers”: what exactly they have to do and who they are.

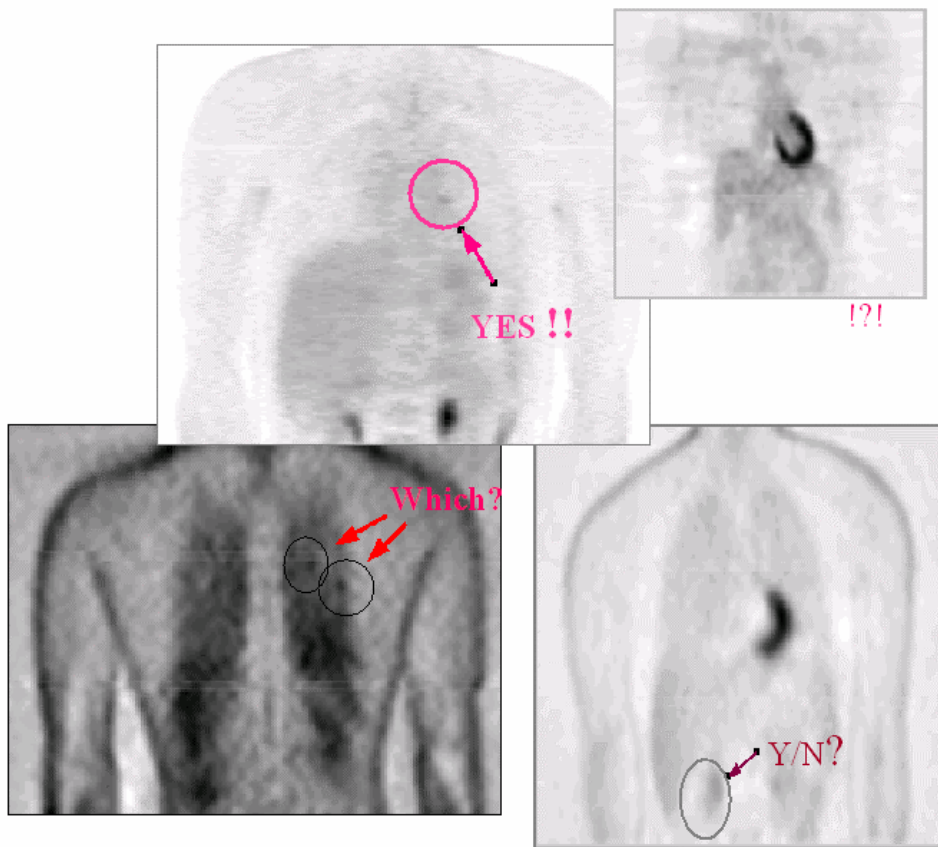


Figure 29: PET images for a lung study. The images are coronal slices of 3D volumes of both healthy and unhealthy patients, reconstructed by different algorithms. The observer is asked to evaluate whether they contain or not a lesion.

In the context of lesion detection, observers are given a set of reconstructions, each of which may be normal or abnormal, i.e. it may be the image of a healthy patient, or it might contain one or more lesions. Examples of such images in the case of a PET lung study are shown in Figure 29. Typically, the observer is asked to specify whether the image is believed to be normal or not. In some cases, the location of the lesion (if supposed to be present) is also requested.

### **Human Observers**

By far the most common observer of real radiographic images is the physician. Hence, radiologists represent the gold standard to perform a study of lesion detection, since this choice is the one that best reflects the clinical scenario.

We note, however, that in some cases the experience and the familiarity that radiologists have at reading medical images might present some disadvantages when the study is performed for the purpose of evaluating and comparing the image quality of different reconstruction algorithms. As a matter of fact, medical staff might be accustomed to interpret one particular type of reconstruction and might not perform as well on images obtained with different methods. The outcome of the study can thus be biased in favor of one algorithm or the other, depending on the previous experience of the observer. In such cases, “unbiased” readers are preferable, even though they are untrained and do not have any medical background or experience in the task of lesion detection.

In the case of human observers, task performance is typically measured by psychophysical studies. Such studies consist of presenting the reader with a set of normal and abnormal images, each of which has to be classified as either negative, i.e. related to a healthy patient, or positive, i.e. containing a lesion. More commonly, instead of simply giving a binary answer, “yes” or “no”, the reader can be asked to express a grade of certainty, or significance, in the answer. For instance, in the study we carried out that we describe later in this part of the thesis, we asked the observer to grade each image with a number from 1 to 5, where the meaning of the

numbers was roughly: 1 = “definitely no lesion”, 2 = “probably no lesion”, 3 = “maybe” or “I do not know”, 4 = “probably a lesion present” and 5 = “definitely abnormal”. The answers are stored in order to be subsequently evaluated. We refer to section 0 for a detailed description of the study. Figure 47 on page 151 shows the graphical interface of the program we developed to perform a human observer study of lesion detection. As one can see, the reader is also allowed to change some settings of the color scale, in order to adjust the visualization in the way that is more convenient to him. Moreover, in order to facilitate discrimination of the signal, not only a single slice is displayed, but also the two adjacent coronal planes.

With human observers more complex studies can be performed, such as those based on images that may contain more than one lesion. Another common alternative to the basic binary task of lesion detection is a localization study: in addition to expressing a grade of certainty about the possible presence of a lesion, observers are also asked to indicate the location of the suspected tumor.

On the other hand, a human observer study is subject to several limitations related to the specific user and to the external conditions, such as vision problems of the reader, distance between the observer and the screen, quality of the display, fatigue of the reader, lightning condition of the environment. Hence, it is suggested to have more than one observer and then consider all sets of answers collected, either by averaging them or by pooling them together.

Also, it is often convenient to have a preparatory, training session precede the real study, so that the observers can acquire familiarity with all details of the study. Figure 46 shows the training session version of the graphical interface we used to perform our detection study. The main difference with the interface used in the “real session” is that the reader is provided with the possibility of knowing the exact nature of the image shown, and in case the image is a positive one, the location of the lesion is indicated by a red spot on the image.

## **Computer Observers**

In theory, human observers satisfy most requirements for a task oriented definition of the term image quality. However, in practice, they are subject to several limitations. When large numbers of images have to be evaluated, psychophysical studies are highly time consuming and costly, especially if real clinical data is used. In addition to this, only a limited set of conditions can be tested in order to keep the problem complexity tractable: analysis has to be restricted to a few choices of engineering parameters, disease entities, type and number of algorithms, etc. Psychophysical studies turn out to be infeasible for a thorough investigation of optimal processing.

For these reasons, there has been recently growing interest in considering automated or machine observers, for which the performance can be more cheaply calculated instead of measured. Roughly, computer observers are programs that “read” an image as input and compute an answer, or statistic, as output, which is usually a number expressing the grade of confidence that the image may contain a lesion. The mathematical aspects underlying these programs are not of straightforward understanding and we thus refer to the later chapters for a comprehensive description.

The concept of computer observers is based on one fundamental idea that has to be strictly considered in the design of the model: since humans are the end users of medical images, computer observers have to be developed with the goal of reproducing the humans behavior, rather than with the final aim of obtaining the highest possible performance. In other words, the best computer observer is not necessarily “ideal” or perfect, but, on the contrary, is able, under certain conditions, to perform as poorly as the human.

This has a couple of important implications.

First, it is essential to understand the effects on human performance of different choices made during the image formation and reconstruction process on the resulting diagnostic performance. As noise is the major limiting factor of human detector performance, it will also represent the key issue to be considered in the design of the mathematical model underlying computer observers.

Second, since the ultimate goal is to reproduce the human behavior, rather than to effectively detect lesions in real clinical data, it is not restrictive to work on simulations, i.e. on images whose real nature – normal or abnormal – is known. This has the advantage that one can “tune” the observer and develop it by explicitly taking into account specific image properties that are known. A classical design choice is to already “center” the computer observer on the location of the lesion (if present), so that the aspect of localization is dropped and the problem is restricted to the issue of detection only.

### **3.1.3. Performance indices**

As mentioned, observer studies are usually performed on a set of simulated images, the real nature of which is known. Thus, once collected, the observer’s responses - no matter whether human or computer observers - can be checked and “graded”. Such a “grade”, or index, expresses the overall performance of the observer and indirectly represents a quality measure of the specific set of images considered.

Several performance indices have been proposed in the literature, some of them being related to a specific computer observer. Although these might have interesting properties and might be mathematically convenient to compute, they have the disadvantage of not being “universal” and precluding the possibility of comparing the performance of different observers over the same set of reconstructions.

Here, we will introduce the idea of Receiver Operating Characteristic (ROC) and the related concept of Area Under the Curve (AUC). ROC studies are presently the most popular way to measure the performance of any kind of binary task study, especially of diagnostic tests in the clinical framework.

Given a set of simulated images, one can preliminarily divide them in two classes, positive (with lesion) and negative (without lesion). Once the observer's answers have been collected and checked, each of the two classes can in turn be split up into two groups: positive images are divided into TP and FN, where TP means "True Positive", i.e. images correctly evaluated as abnormal, and FN stands for "False Negative", i.e. images falsely considered normal. Likewise, negative images will fall into TN and FP, TF standing for "True Negative", i.e. images correctly recognized as not containing any lesion, and FP meaning "False Positive", i.e. images wrongly considered abnormal. These concepts are sketched in Figure 30a.

Reader's answer:	"Negative"	"Positive"
Real nature of the images:		
Abnormal (with lesion)	False Negative	True Positive
Normal (no lesion)	True Negative	False Positive

(a)

Reader's answer:	"Negative"	"Positive"
Real nature of the images:	1   2   3   4   5 ←-----→	
Abnormal (with lesion)	False Negative	True Positive
Normal (no lesion)	True Negative	False Positive

Threshold

(b)

Figure 30: Partitioning of the image set according to the real nature of each image and to the reader's answers a) when only a binary answer is given about the assumed nature of the image and, b) when also a grade of certainty is provided.

When the reader's answer is not simply a binary one but a degree of certainty is also specified, then one can introduce a threshold in order to determine where to split the classes. For instance, if the reader's answer is a number from 1 to 5 then, by setting a threshold at 2, one fixes all abnormal images rated less than or equal to 2 as being FN, all abnormal images rated more than 2 as being TP, normal images rated less than or equal to 2 as TN, and normal images graded more than 2 as FP. This example is shown in Figure 30b.

Different values of the threshold point out different properties of the test. More precisely, two basic attributes are associated with a binary task:

*Sensitivity*: highly sensitive tests exclude the presence of a disease when reporting negative results.

*Specificity*: highly specific tests confirm the presence of a disease, when reporting positive answers.

In order to express the reader's performance in relation to both attributes one should encode the answers for all possible values of the threshold. This is exactly what ROCs do. ROCs are curves that map the TP fraction versus the FP one for each possible value of the threshold. It is probably worth pointing out that, for any given threshold value, once the TP value is stored, the information given by FN is redundant because it can be obtained as the difference between the *<number of abnormal images>* and the *<number of TP images>*. In other words, the relation

$$\langle \text{number of TP} \rangle + \langle \text{number of FN} \rangle = \langle \text{number of abnormal images} \rangle$$

always holds for the way TP and FN were defined. A similar reasoning applies to TN and FP in the case of negative images, namely:

$$\langle \text{number of FP} \rangle + \langle \text{number of TN} \rangle = \langle \text{number of normal images} \rangle$$

Figure 31 sketches the idea of ROC curve. Three points on the ROC curve are shown, corresponding to three values of the threshold, respectively.

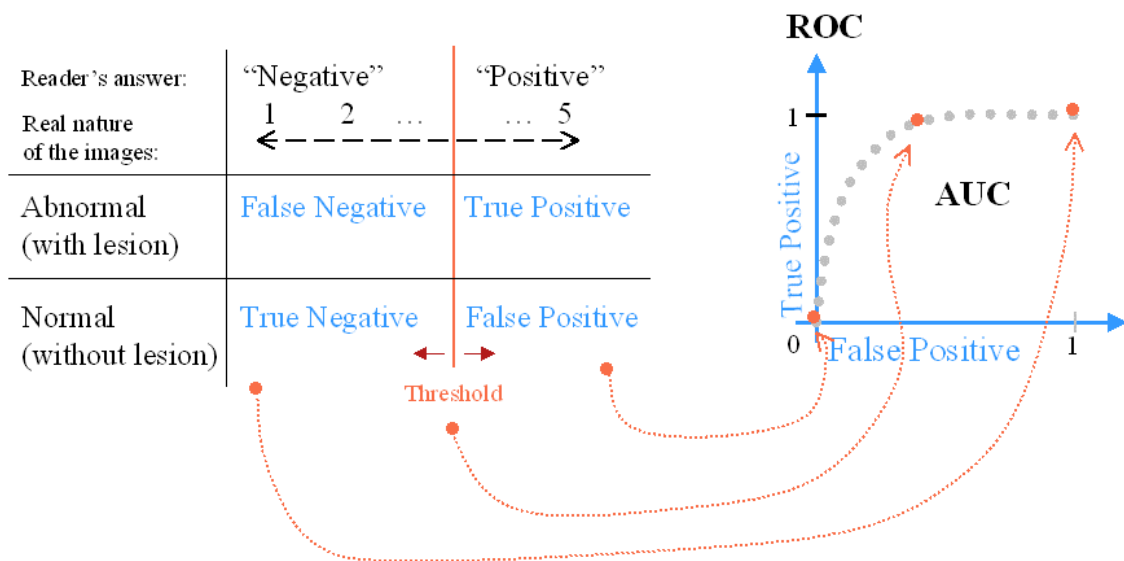


Figure 31: Graphical representation of the concept underlying the definition of ROC curve.

Evidently, that the performance is poor if TP is small and FP is large. When normal and abnormal images are equally distributed, i.e. when there is the same number of positive and negative images, then, an ROC curve given by the straight line  $TP=FP$  for all values of the threshold means that the observer gave random answers, equally distributed around the middle value of the possible grades (2.5 when the rating interval is [1,5]). Conversely, good performance is obtained when TP is large and FP is small. This suggests the idea of measuring the area under the curve as and index of the performance. The bigger the area, the better the observer performance. In the context of ROC studies, such index is referred to as AUC. Its potential lies in the fact that it expresses in a single scalar value the results of a study in which even hundreds of images may be involved.

Similar methods to those described above for a binary task of lesion detection have been proposed for more complex tasks such as multiple lesion detection or lesion localization. With reference to this latter case, the term LROC is used, which stands for Localization Receiver Operating Characteristic.

In the sections that follow we will provide the mathematical background underlying the concept of computer observer and we an efficient approximation that we have developed to compute the statistic of one specific computer observer model in a fast and reliable way. We will then show the studies that we have performed using both computer and human observers, with the latter case also including a task of localization. We will plot the ROC curves obtained from the readers' results and compute the AUC values in order to compare the performance over various sets of images, obtained with different parameter settings respectively. The images on which these studies are based were all reconstructed with the MAP algorithm introduced in the previous part of the thesis. The observer results gave us interesting feedback about the performance of this algorithm and pointed out the direction to take in order to optimize this method for the task of clinical lesion detection.

## Computer observers

The necessity of reproducing human signal detection performance in a fast and cheap way has led in recent years to the investigation of appropriate mathematical models, referred to as Computer Observers. The major goal is to reliably reproduce the human behaviour, rather than to obtain the most possible accurate detection capability. Steps towards clinical realism have to be made: this means that the analysis has to be extended from SKE / BKE tasks<sup>18</sup> – namely, the detection of completely specified signals, such as disks and bars, located in a uniform background - to noise limited tasks with statistically defined signal and background. In these more sophisticated cases, the optimal computer observer statistic is usually non-linear and analysis becomes mathematically intractable [Bur95]. For this reason, linear, sub-optimal observer models have been proposed that are mathematically more convenient. We will here give an overview this class of methods and in the next subsection we will focus on one particular of such algorithms, the Channelized Hotelling Observer.

Computer observers are applied to single images  $\mathbf{g}$  belonging to either a class of normal images  $\mathbf{f}_B$ , i.e. without any lesion, or a class of abnormal images  $\mathbf{f}_L$  containing a lesion. The mathematical model of the observer is a test statistic  $\lambda$ , whose value over a given image is compared to a threshold: if the value is below the threshold the image is assumed not to contain any lesion, otherwise it is considered abnormal.

---

<sup>18</sup> Signal Known Exactly / Background Known Exactly

The general test statistic  $\lambda$  of a linear observer for detecting a known lesion is [Bar92]

$$\lambda(\mathbf{f}) = [\bar{\mathbf{f}}_L - \bar{\mathbf{f}}_B]^T \mathbf{K}^{-1} \mathbf{f} \quad (33)$$

where  $\mathbf{f}$  is the image on which the statistic is computed and  $\bar{\mathbf{f}}_L$  and  $\bar{\mathbf{f}}_B$  are the means of the two classes of images with and without lesions, respectively. The superscript 'T' denotes a matrix transpose and  $\mathbf{K}$  is the matrix that determines the form of the observer, as sketched in Figure 32.

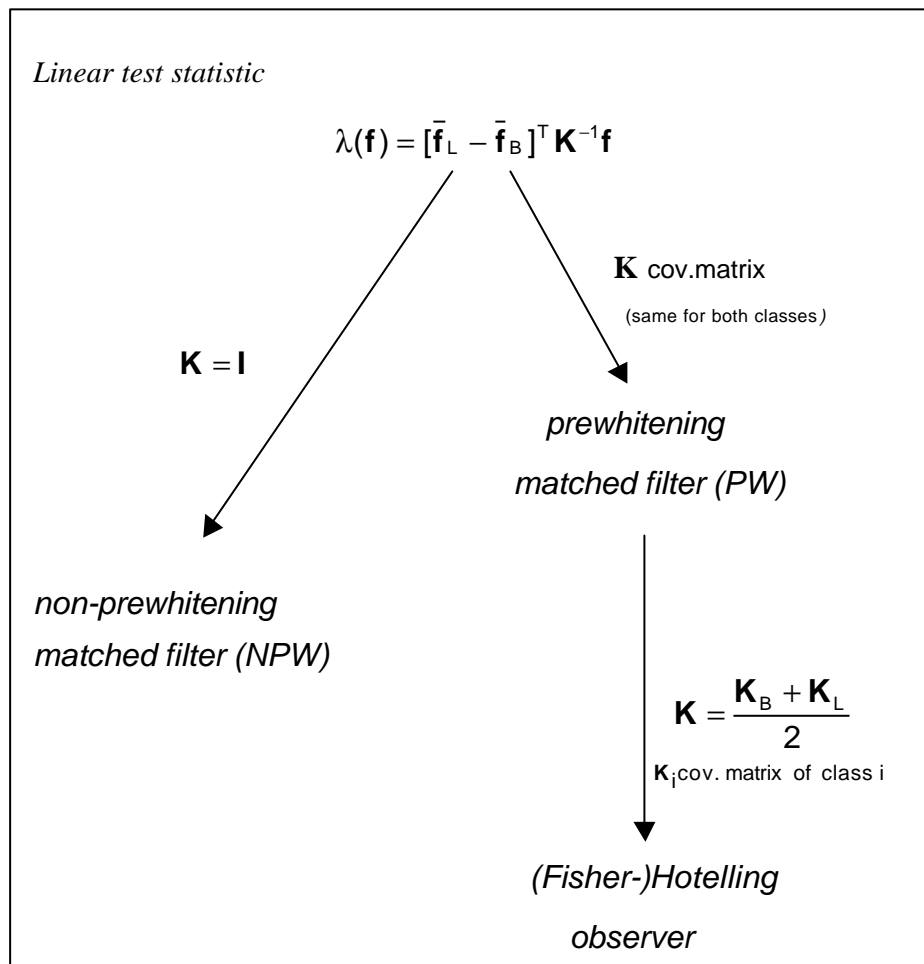


Figure 32: The main linear observer statistics as defined by the form of matrix  $\mathbf{K}$ .

If  $\mathbf{K}$  is the identity matrix, then the observer is a simple non-prewhitening matched filter (NPW) because there is no compensation for any noise correlation. Although it is inferior to the ideal test statistic, it has the virtue of correctly predicting human performance in a range of SKE/BKE tasks as, for instance, when the signal is known exactly and the noise is stationary, white and gaussian [Bar92]; on the other hand, it yields to very poor correlation with the human if there is inherent randomness in the task.

In order to deal with more sophisticated, realistic tasks that include randomness, different forms of the matrix  $\mathbf{K}$  have been proposed that basically all aim at decorrelating the noise inherent in the image. The simplest of such forms is when  $\mathbf{K}$  is a covariance matrix for both classes of normal and abnormal images. Then  $\lambda$  is the so-called prewhitening matched filter and is suitable when the noise is stationary and Gaussian but not white. Unfortunately, as discussed in [Bar92] and [Mye85], there is strong evidence that the human is not capable of performing certain kinds of noise decorrelation and, in these cases, the prewhitening matched filter is not an appropriate model.

A more sophisticated linear observer statistic is when the matrix  $\mathbf{K}$  is the mean of two covariance matrices  $\mathbf{K}_B$  and  $\mathbf{K}_L$  of the two classes of images respectively:

$$\mathbf{K} = \frac{\mathbf{K}_B + \mathbf{K}_L}{2} \quad (34)$$

Hence  $\mathbf{K}$  is a second order statistic and, because of its form, it is an intraclass matrix, while  $\mathbf{K}_B$  and  $\mathbf{K}_L$  are first order statistics, interclass matrices; they are obtained as the average of all  $\mathbf{f}$  produced by some data  $\mathbf{g}$  in class  $i = L$  (lesion) and  $i = B$  (non-lesion) and some realization of noise; this average is specified by the notation  $\langle \rangle_i$ :

$$\mathbf{K}_i = \langle (\mathbf{f} - \bar{\mathbf{f}}_i)(\mathbf{f} - \bar{\mathbf{f}}_i)^T \rangle_i \quad i = B, L .$$

This form of a linear discriminant is often ascribed to Fisher [Fis36], but had its origins in a classic paper by Hotelling [Hot31] and, therefore, will be here referred to as the Hotelling Observer. It is interesting to observe that the Hotelling observer statistic is a generalization of the prewhitening matched filter, in that the noise covariance matrix is replaced by a more general, weighted matrix.

Several investigations comparing this discriminant with others ([Bur95, Fie87, Rol92]) proved it to give a very good fit to human performance, although it is not as predictive a tool when high-pass noise correlations introduced by post-processing of the images are present [Bar92]; the Hotelling observer was also shown to feature too high a level of adaptiveness compared to the human performance and, thus, perform “too well” with respect to the human model it is supposed to reproduce. This appears evident when a large variety of conditions is considered, such as different controlled viewing distances, different signal shapes and several correlation distances for a lumpy background [Bur95, Rol92]. It has been suggested that it was modified to include spatial-frequency-selective channels similar to those of the human visual system. Such a variant is presented in the next subsection.

## **The Channelized Hotelling Observer**

We introduce here a special form of (33), called the Channelized Hotelling Observer (CHO) [Yao92], since it is based on the covariance matrix  $\mathbf{K}$  of the Hotelling Observer defined by (34) and the images  $\mathbf{f}$  are filtered by frequency-selective channels that model properties of the human visual system.

The channel space in which the reconstructions are considered is defined by a matrix  $\mathbf{U}$  whose rows represent the impulse response of frequency selective filters centered at the test location of the lesion [Kin97]. By calling  $\mathbf{r}$  the filtered images  $\mathbf{U}\mathbf{f}$ , the similarity between the Hotelling Observer and the Channelized Hotelling Observer statistic is pointed out, the latter being:

$$\lambda(\mathbf{f}) = [\mathbf{U}\bar{\mathbf{f}}_L - \mathbf{U}\bar{\mathbf{f}}_B]^T \mathbf{K}^{-1} \mathbf{U}\mathbf{f} = [\bar{\mathbf{r}}_L - \bar{\mathbf{r}}_B]^T \mathbf{K}_U^{-1} \mathbf{r} \quad (35)$$

where we implicitly assume that the two types of images – “No-lesion” and “Lesion” – are equally probable.  $\mathbf{K}_U$  is the mean of the two covariance matrices for the two classes after transformation through the channels, i.e. it is the composite channel noise covariance matrix:

$$\mathbf{K}_U = \frac{\mathbf{K}_{UB} + \mathbf{K}_{UL}}{2}$$

$$\mathbf{K}_{U_i} = \left\langle (\mathbf{r} - \bar{\mathbf{r}}_i)(\mathbf{r} - \bar{\mathbf{r}}_i)^T \right\rangle_i \quad i = B, L$$

The channels incorporate elements of the human visual system in that they act as circular symmetric filters selecting specific frequencies in a similar way the human system does. From a mathematical point of view, they are convenient because they are applied to the image in terms of a vector product and, thus, they preserve the linearity of the Hotelling discriminant. Moreover, the prewhitening operation achieved by matrix  $\mathbf{K}_U$  is entirely performed in the channel space, where data are smaller than in the image space because a small number of channels – usually between 2 and 5 - is used. For this reason, the time complexity of the noise decorrelation procedure turns out to be smaller for the CHO than for the standard Hotelling Observer. These concepts are illustrated in Figure 33.

Among the different types of channels that can be used the two most popular choices are DOG (Difference of Gaussians) and SQR (Square non overlapping channels) [Abb96, Cha98, Kin97]. Three profiles are shown in Figure 34 for each of these two cases, both in the space and in the frequency domain.

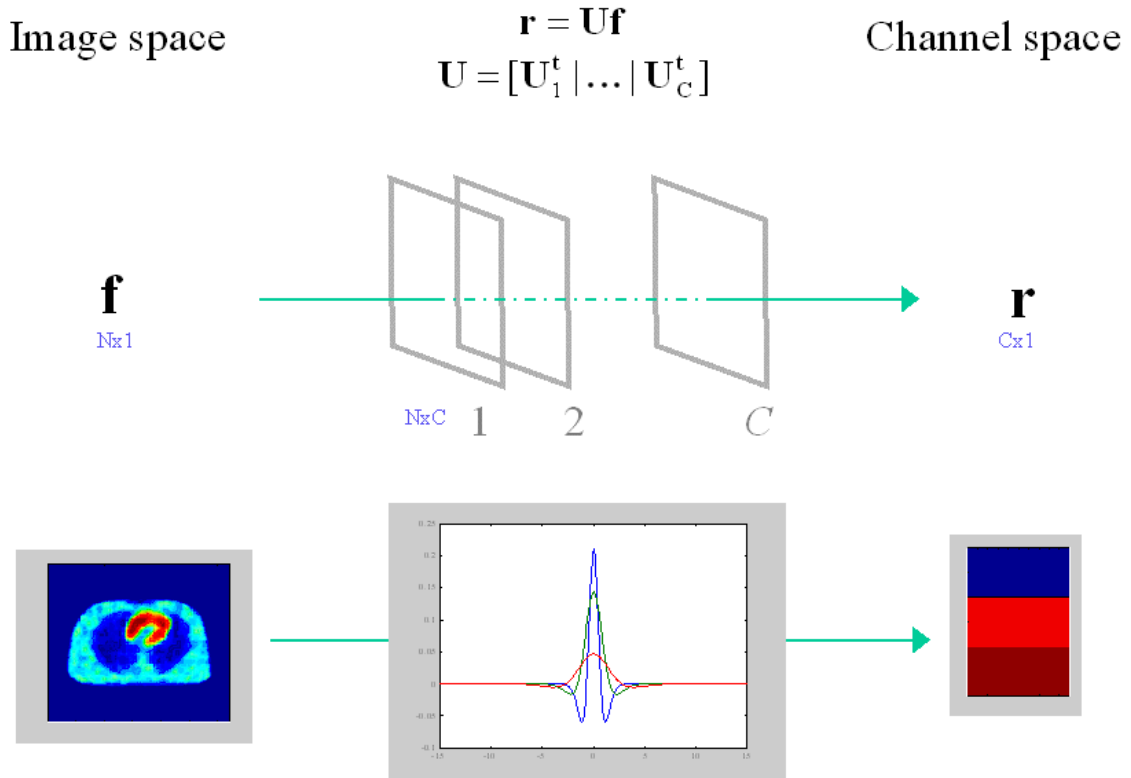


Figure 33: Transformation of an image into the channel space. Data complexity is reduced from  $N$  in the image space, where  $N$  is the dimension of the vector representing the image, to  $C$  in the channel space, where  $C$  is the number of channels used. Represented in the lower, central portion of the image is the profile of three bidimensional DOG channels in the space domain.

The  $k$ -th DOG channel [Abb95, Cha98] is defined as

$$T_k(i, j) = G(i - x_c, j - y_c, s_k) - G(i - x_c, j - y_c, s_{k-1})$$

where  $(i, j)$  are pixel coordinates and  $(x_c, y_c)$  is the center of the filter, which is set to be the same as the location of the lesion.  $G$  is a gaussian function,

$$G(x, y, s) = \frac{1}{2\pi\sigma^2} \exp\left(-\frac{x^2 + y^2}{2\sigma^2}\right)$$

with parameter  $\sigma$  given by

$$\sigma_k = \frac{1}{2\pi f_k}$$

$$f_k = c f_{k-1} = c^k f_0$$

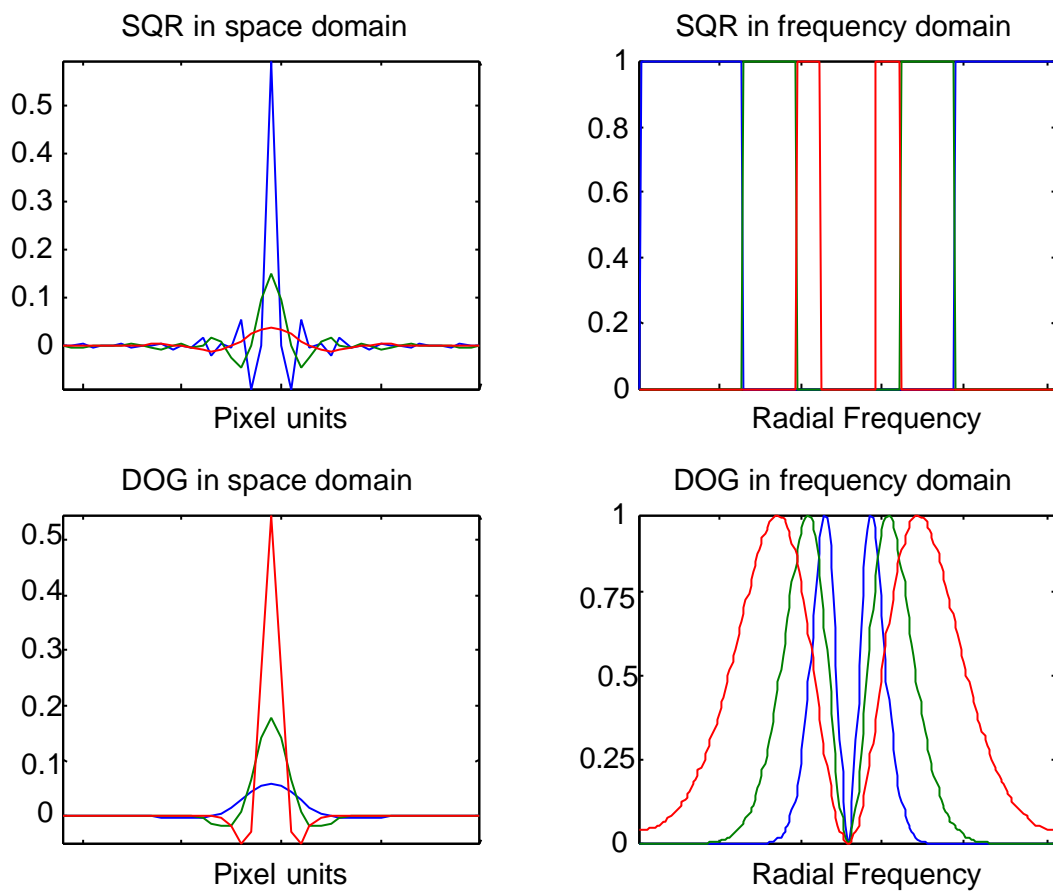


Figure 34: Profiles of three DOG and SQR channels respectively, both in the space and in the frequency domain.

For a three channel model  $f_0=0.06$  (measured in inverse pixel units) and  $c=1.75$  give the best fit to human performance; however, results depend on various factors, as the actual viewing distance and the physical pixel size of the displayed images. As suggested in [Cha97], in the studies that follow we will use  $f_0=0.03$  and  $c=1.75$ .

SQR channels as proposed by [Bar90] and [Mye87] are square functions in the frequency domain, with a filter width of 2 and the Nyquist frequency as the maximum frequency, passed by the first channel.

The observer Signal to Noise Ratio can be written as [Bar90b, Mye87]

$$\text{SNR} = \sqrt{\lambda(\bar{\mathbf{f}}_L - \bar{\mathbf{f}}_B)} .$$

Moreover, under the assumption that  $\lambda(\mathbf{g})$  is Gaussian, the area under the ROC curve is related to the SNR [Bar92, Bur95a] and can be written in terms of the observer statistic as

$$AUC = \frac{1}{2} \left( 1 + \text{erf} \left( \frac{\sqrt{\lambda(\bar{\mathbf{f}}_L - \bar{\mathbf{f}}_B)}}{2} \right) \right) \quad (36)$$

## Simulations

We have tested the Channelized Hotelling Observer on a set of synthetic data reconstructed using a MAP algorithm for different values of the smoothing parameter  $\beta$ : the goal was to investigate the sensitivity of the observer with respect to the hyperparameter and detect the best range of  $\beta$  values for the task of lesion detection on this specific type of image.

## The study

The study was based on a 2D chest phantom; the process of data generation is sketched in Figure 35.

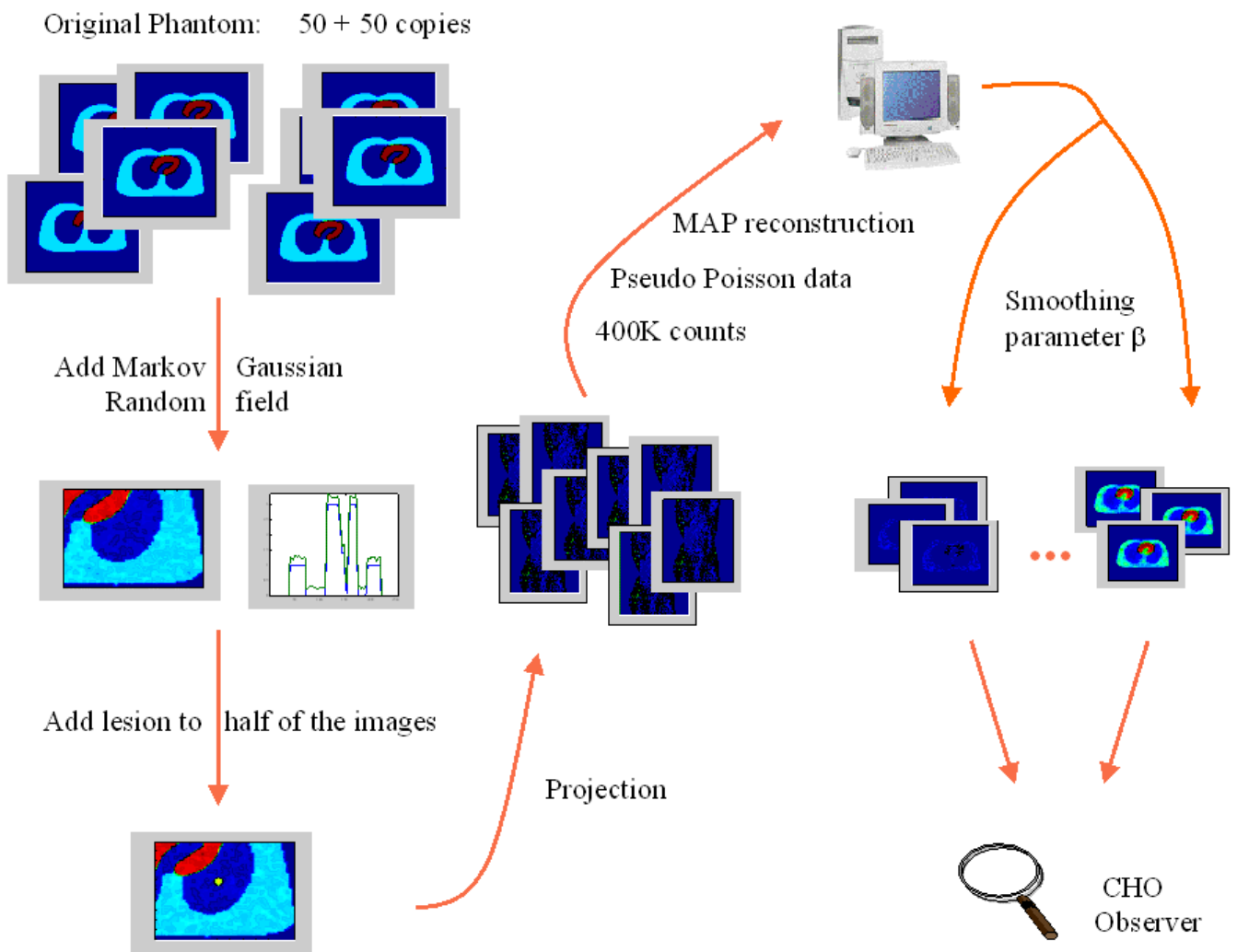


Figure 35: Data set generation for the Monte Carlo study to test the CHO performance.

The simulation consisted of a Monte Carlo analysis based on a 256x256 pixel chest phantom of which 100 realizations were obtained by adding a Markov Gaussian Random field to the anatomy. A lesion with constant activity across a three pixel radius circle was added to half of the objects in a fixed location (lower right half). The sinograms were computed using the realistic system model that we have developed for the CTI ECAT HR+ scanner [Qi98b] and then scaled to a mean of 400K counts on which pseudo-Poisson data was generated. They were finally reconstructed into 128x128 pixel images using up to 60 iterations of a MAP algorithm for different values of the smoothing parameter  $\beta$ .

We computed the sample mean difference  $\bar{r}_L - \bar{r}_B$  and the sample covariance matrix  $\mathbf{K}_U^{-1}$  for the CHO observer for the two different types of channels mentioned above, SQR and DOG, with three filters in each case. We then computed the performance of the observer as measured by the AUC, as defined in Eq.(36).

## Results

A plot of the AUC values for the SQR channels is shown in Figure 36, and the analogous plot computed with DOG channels is reported in Figure 37.

The results meet our expectations: the CHO is proven to be sensitive to the choice of the hyperparameter values, providing results that degrade with increasing values of  $\beta$ , i.e. with increasing smoothing of the reconstructions. DOG and SQR channels show different behaviours, the former providing overall better results and a maximum AUC of 0.950 for  $\beta = 100$ . AUC values obtained by the implementation of SQR channels are in general slightly lower, and they reach the highest values for small choices of the hyperparameter (smaller than 10), in contrast with the optimum range of [1,200] featured by the DOG channels; the maximum AUC of 0.932 is reported for  $\beta = 8$ .

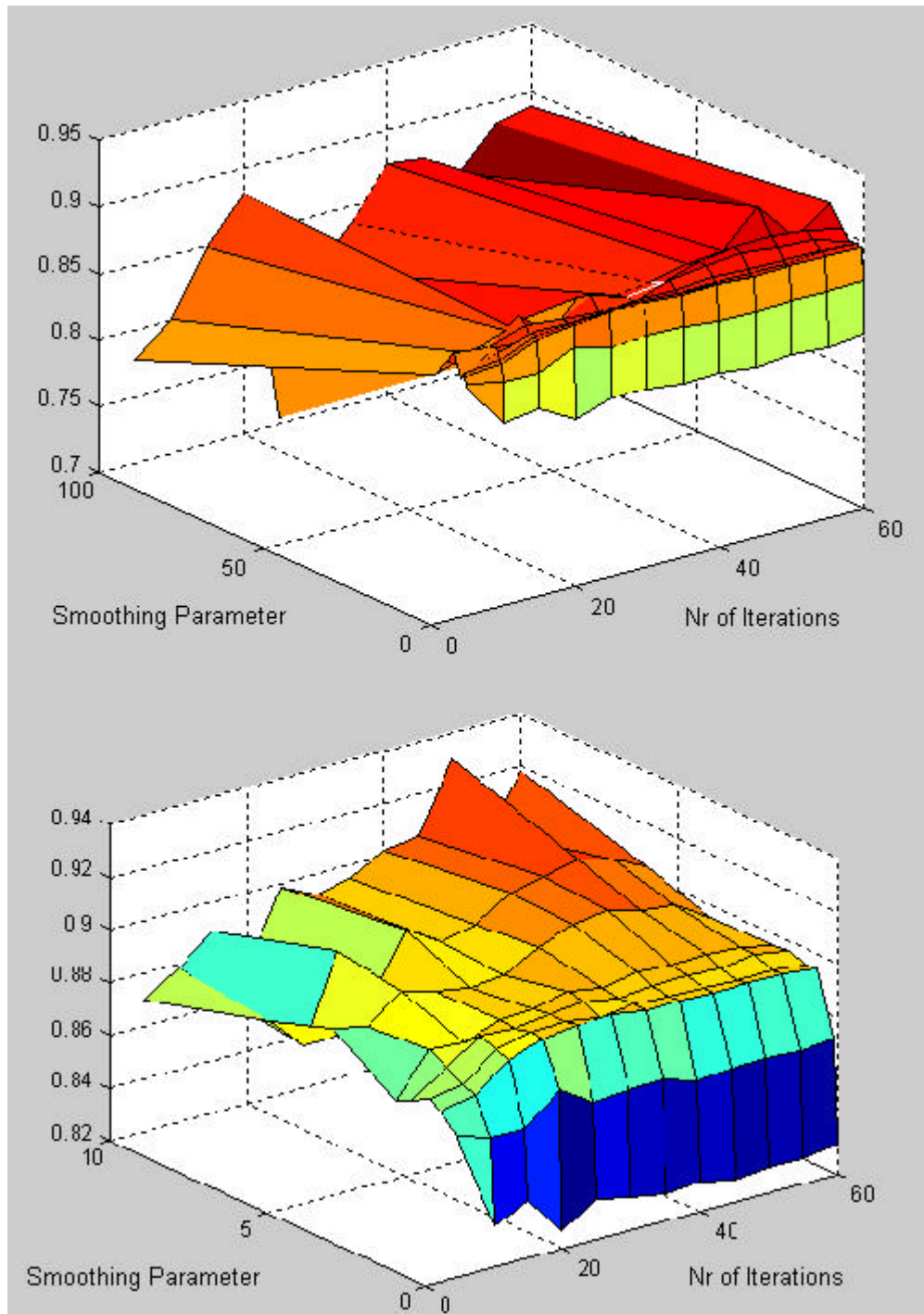


Figure 36: AUC values of the CHO with SQR channels applied to sets of images reconstructed with up to 60 iterations of a MAP algorithm for different values of the smoothing parameter  $\beta$ . The plot in the bottom zooms over lower values of the hyperparameter.

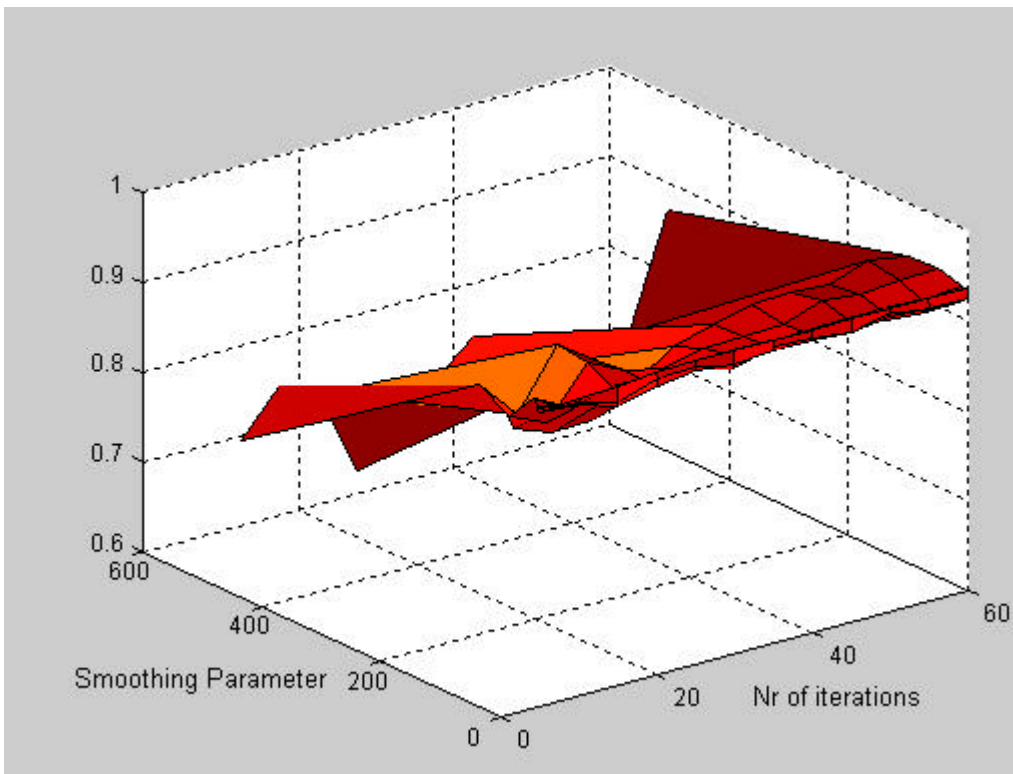


Figure 37: AUC values computed by the CHO with DOG channels over sets of images reconstructed with up to 60 number of iterations of a MAP algorithm, for different values of the smoothing parameter  $\beta$ .

This difference is more clearly pointed out by the plots of Figure 38, which represent the distribution in a 2D channel space of a set of reconstructions obtained for  $\beta = 100$ . Two channels only are considered for each of the two cases SQR (top) and DOG (bottom). The two different colors of the dots indicate the normal (blue) and abnormal (red) classes of images and they evidence how the two classes are well separated in the case of DOG channels, while they are more hardly distinguishable in the case of SQR filters, for this choice of the hyperparameter value.

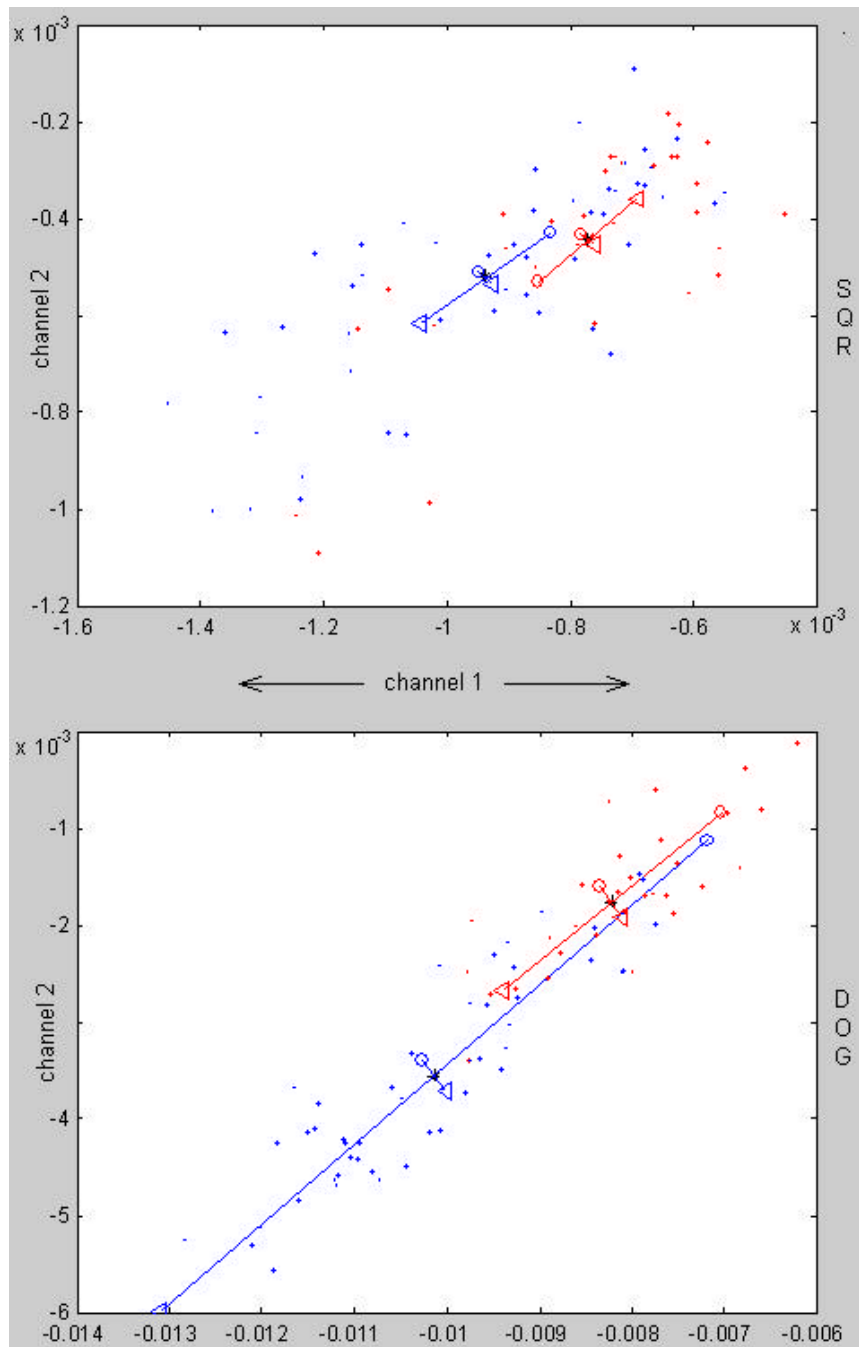


Figure 38: Plot of the image distribution in the channel space. Two channels are considered for each of the two cases SQR (top) and DOG (bottom). The two different colors of the dots are referred to the normal (blue) and abnormal (red) classes of images; the arrows represent the eigenvectors of the covariance matrices  $\mathbf{K}_b$  and  $\mathbf{K}_l$  and they are centered on the mean of the two classes of images respectively. The plots are computed on a set of reconstructions obtained with  $\beta = 100$ .

A possible explanation of the difference between the two types of filters is that the frequencies passed by the first of the DOG channels perfectly match those of the Markov gaussian random field that was initially added to the organ. Hence, the lesion, which was added to the gaussian field, is well isolated by the DOG channels. It is to be noted, however, that despite of the differences reported by the CHO using different channels, a visual inspection of the reconstructions for  $\beta$  varying within the (0,200] interval did not point out any major difference and did not suggest any preference or advantage of the  $\beta$  values in the (0,10] interval over higher choices.

### **Variance and Bias of Monte Carlo simulations**

The accuracy of the Monte Carlo study to compute the observer performance as measured by the AUC values is degraded by effects due to the finite sample size of the sets used in the simulations [Das74, Fuk89, Rau91]. In fact, the AUC values computed using sample statistics are affected by both variance and bias.

To gain a deeper insight into these effects, we extended the chest phantom study from 100 to 1000 images. We first addressed the problem of the variance, by applying the observer to several sets of 50+50 reconstructions each ( $\beta=100$ , CHO implementation with DOG channels), randomly chosen among the 1000 images. An example of the distribution of the AUC values thus obtained is shown in Figure 39. In this specific case, the distribution has a standard deviation of 0.022.

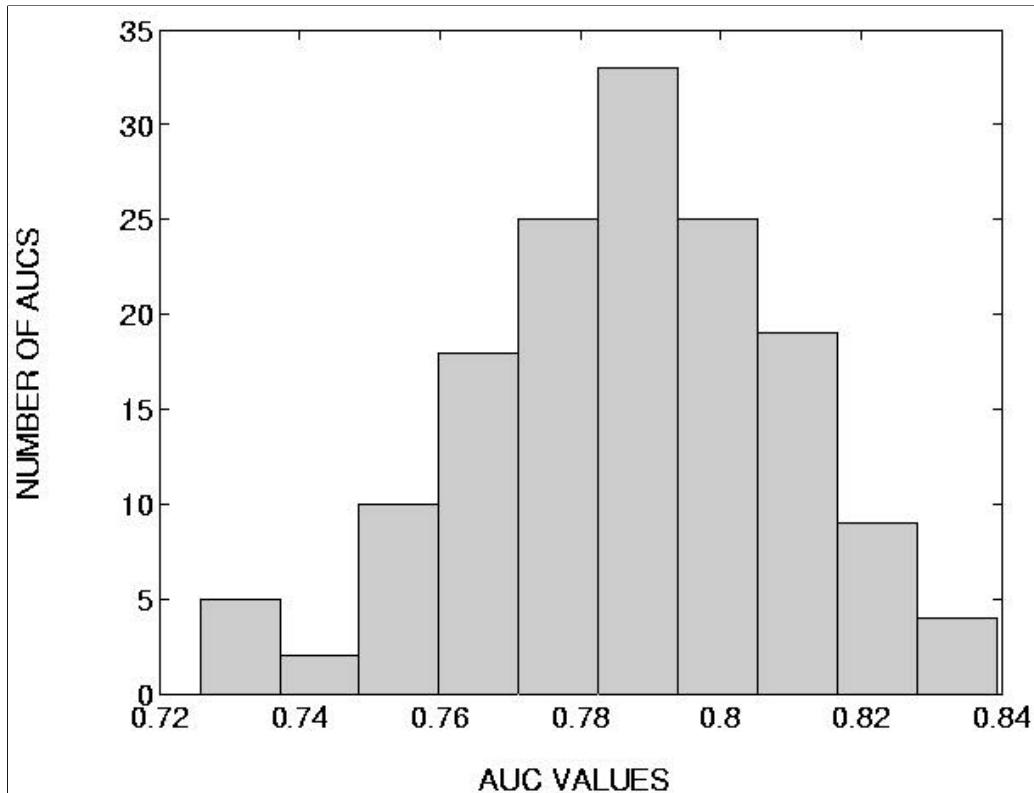


Figure 39: Distribution of the AUC values computed on 150 sets of 100 reconstructions each, randomly selected within a set of 1000 samples: standard deviation = 0.022.

We also plotted the AUC values as a function of the number of samples to examine changes in bias as a function of the number of images in the study. In the graph shown in Figure 40, each AUC is obtained as the average of 250 AUC values, each computed on sets of 100 reconstructions randomly selected within a set of 1000 samples. Because of the very high computational costs and storage space required, the image set is not large enough to allow one to pick completely independent sample sets and, thus, the AUC values are correlated. Nevertheless, the curve clearly shows a  $1/N$ -like dependency on the number of samples. These observations are consistent with the studies presented in [Fuk89].

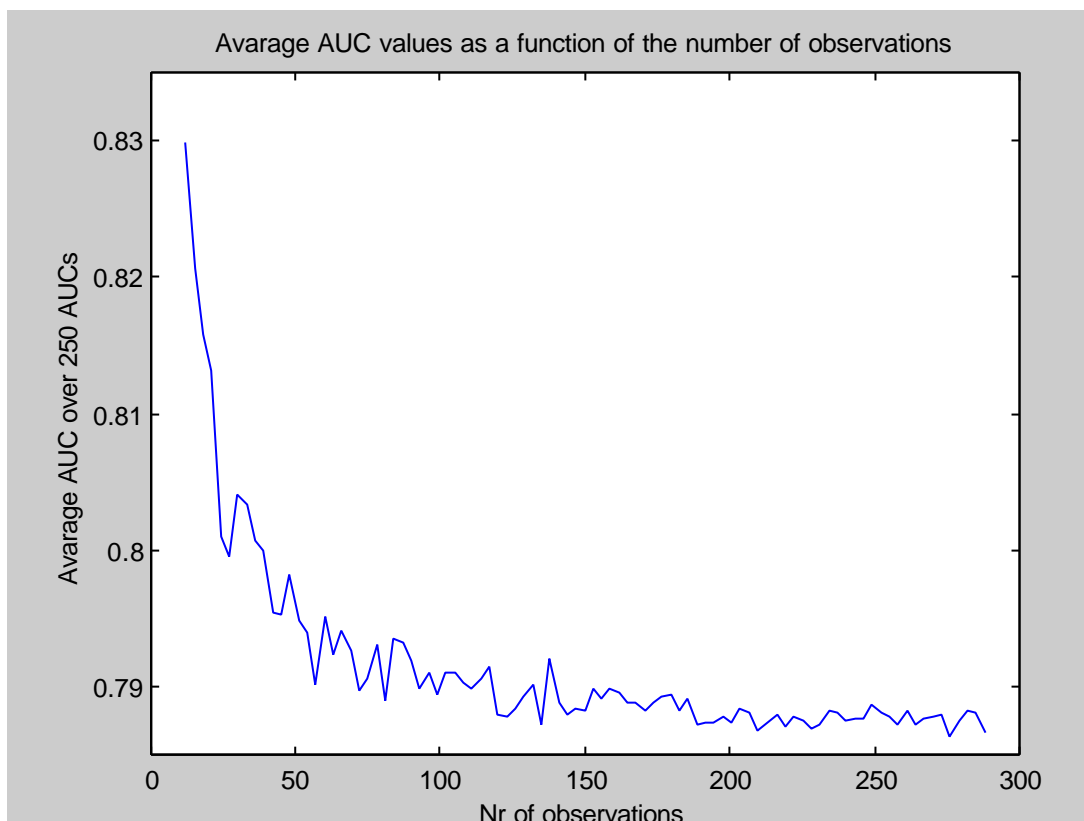


Figure 40: AUC values as a function of set cardinality: each AUC value was obtained as the mean of 250 values, each computed on sets of 100 reconstructions randomly selected within a set of 1000 samples.

## **A theoretical approximation for the computation of the CHO statistics**

The raison d'être of computer observers lies in their capability of overcoming the two major problems associated with psychophysical studies performed by human observers: high costs and subjective results. Methods for reliably reflecting human performance and efficiently and accurately computing the statistics may thus prove to be very useful, especially when evaluating reconstructed image quality over a

wide parameter space: these methods can be used to investigate changes in performance associated with variations in the parameters of the PET system, the source distribution, and the reconstruction method. Although computer observers represent an extremely advantageous tool in terms of computational costs with respect to human observers, they still require a considerable amount of computational resources, since they are based on highly time consuming Monte Carlo simulations, and their application to a wide range of different conditions might still be unfeasible in practical cases.

We have developed a theoretical approximation for quickly and accurately computing the statistics of linear observers applied to PET images reconstructed using nonlinear MAP algorithms [Bon00]: it is based on a theoretical approximation for the mean and covariance of MAP reconstructions, modelling both the Poisson statistics of PET data and the inhomogeneity of tracer uptake. As shown by the simulations described later, our model features good correspondence with the results obtained by standard Monte Carlo simulations.

The Hotelling observer makes use of the covariances of the images. For linear algorithms this can be computed directly from the mean of the data by assuming a Poisson model. However, when the reconstruction estimator is nonlinear, analysis of the covariance is more difficult. Moreover, when the image is defined implicitly as the maximizer of a cost function, there will be no closed-form expression for the image covariance, which is usually estimated through highly time consuming Monte Carlo simulations.

Fessler [Fes96a] developed an approach to solving this problem by using truncated Taylor series approximations: the reconstruction  $\hat{\mathbf{x}}(\mathbf{y})$  of data  $\mathbf{y}$  is approximated by its first order Taylor expansion as

$$\hat{\mathbf{x}}(\mathbf{y}) \approx \hat{\mathbf{x}}(\bar{\mathbf{y}}) + \nabla_{\mathbf{y}} \hat{\mathbf{x}}(\bar{\mathbf{y}})(\mathbf{y} - \bar{\mathbf{y}}). \quad (37)$$

As a result the covariance can be approximated by

$$\text{Cov}(\hat{\mathbf{x}}) \approx \nabla_{\mathbf{y}} \hat{\mathbf{x}}(\bar{\mathbf{y}}) \text{Cov}(\mathbf{y}) [\nabla_{\mathbf{y}} \hat{\mathbf{x}}(\bar{\mathbf{y}})]^T \quad (38)$$

In [Qi99a, Qi99f] this approach was adapted to obtain approximate theoretical expressions for the covariance of MAP images as a function of the mean of the sinogram data. The approximate covariance is based on an assumption of local invariance in the response of the PET system and is computed for each voxel using Fourier transforms with only one data dependent parameter that can be obtained by a modified backprojection of the mean sinogram.

The noise in PET data results from two factors, namely, (i) Poisson noise intrinsic to PET data and (ii) variability in the unknown image  $\mathbf{x}$  due to inhomogeneous tracer uptake. Let  $\boldsymbol{\mu}$  and  $S_x$  denote the mean and covariance, respectively, of tracer uptake. Then the covariance of the PET data is

$$\text{Cov}(\mathbf{y}) = D[(\mathbf{P}\boldsymbol{\mu})_i] + \mathbf{P}\boldsymbol{\Sigma}_x\mathbf{P}^T \quad (39)$$

where  $D[x_i]$  represents a diagonal matrix with diagonal elements  $x_i$ ,  $i=1, \dots, N$  and  $\mathbf{P}$  is the detection probability matrix.

Along the lines suggested in [Fes96b] the term  $\nabla_{\mathbf{y}} \hat{\mathbf{x}}(\bar{\mathbf{y}})$  can be derived from the objective function using the chain rule and the implicit function theorem: for the specific case of Poisson emission data and MAP estimation it can be approximated as

$$\nabla_{\mathbf{y}} \hat{\mathbf{x}}(\bar{\mathbf{y}}) \approx [\mathbf{F} + \beta\mathbf{R}]^{-1} \mathbf{P}^T D \left[ \frac{1}{\bar{\mathbf{y}}_i} \right] \quad (40)$$

where  $\mathbf{F} = \mathbf{P}^T D \left[ \frac{1}{\bar{\mathbf{y}}_i} \right] \mathbf{P}$  is the Fisher information matrix when using a Poisson

likelihood model [Fes96a] and  $\mathbf{R}$  is related to the energy function  $U(\mathbf{x})$  for a log quadratic prior by  $U(\mathbf{x}) = \mathbf{x}^T \mathbf{R} \mathbf{x}$ .

The substitution of equations (39) and (40) into (38) leads to the final closed form for the approximate covariance for  $\hat{\mathbf{x}}$ :

$$\text{Cov}(\hat{\mathbf{x}}) \approx [\mathbf{F} + \beta \mathbf{R}]^{-1} \mathbf{F} [\mathbf{F} + \beta \mathbf{R}]^{-1} + [\mathbf{F} + \beta \mathbf{R}]^{-1} \mathbf{F} \Sigma_{\mathbf{x}} \mathbf{F} [\mathbf{F} + \beta \mathbf{R}]^{-1}. \quad (41)$$

As shown in [Qi00], this term can be computed on a voxel by voxel basis using Fourier transforms, by assuming the PET system response to be locally shift invariant, i.e.:

$$\text{Cov}_j(\hat{\mathbf{x}}) \approx \mathbf{Q}^T \mathbf{D} \left[ \frac{\kappa_j^{-2} \lambda_i(j) + \lambda_i^2(j) \bar{\sigma}_i^2}{(\lambda_i(j) + \beta \kappa_j^{-2} \mu_i(j))^2} \right] \mathbf{Q} \mathbf{e}_j. \quad (42)$$

Here,  $\mathbf{Q}$  and  $\mathbf{Q}^T$  are the Kronecker form of the 2D DFT matrix and its inverse respectively;  $\mu_i(j)$  and  $\lambda_i(j)$  are related to the prior energy function in the MAP estimator and to the detection probability matrix, respectively;  $\kappa_j^2$  is the  $(j,j)$ -th element of the Fisher information matrix and thus represents the aggregate uncertainty in the measurement rays that intersect the  $j$ -th pixel;  $\bar{\sigma}_i$  is the 2D Fourier transform of the covariance  $S_{\mathbf{x}}$  of the unknown object;  $\mathbf{e}_j$  is the  $j$ -th unit vector.

These equations are able to model both the variation in the image and a spatially variant detector response using a local-invariant approximation as described in [Qi00]. However, they also assume a local stationarity in the covariance  $S_{\mathbf{x}}$  of the original image. Clearly, this assumption is not particularly well suited to the case of varying lesion sizes and activities. For this reason, the simulations presented in the following section assume a deterministic lesion but include random variation in the background activity in the form of a locally stationary Gaussian random field.

If variability in the lesion is also to be included, then the contribution to the reconstructed image covariance from the source image covariance must be accounted for by specific computation in the spatial domain of the appropriate terms in (42). This will result in increased computation costs, but they will still remain orders of magnitude lower than that required for an equivalent Monte Carlo study.

In [Qi99f] it is shown how the covariance approximation can be modified to compensate for the nonlinear effect of the non-negativity constraints typically used in MAP reconstruction and which are not taken into account when using the first order Taylor series expansion (40).

Approximation (41) is the key for explicitly computing the CHO statistic (35) in terms of the data. In fact, noting that in the case of MAP reconstruction the statistic's argument  $\mathbf{f}$  is given by the estimate  $\hat{\mathbf{x}}$ , we have the following:

$$\mathbf{K}_U = \mathbf{U}\mathbf{K}\mathbf{U}^T = \mathbf{U}\text{Cov}(\hat{\mathbf{x}})\mathbf{U}^T.$$

The first order Taylor expansion (40) can be used again to approximate the mean of the reconstructions as the reconstruction of the noiseless data [Fes96a] and, thus,

$$\bar{\hat{\mathbf{x}}}(\mathbf{y}_L) - \bar{\hat{\mathbf{x}}}(\mathbf{y}_B) \approx \hat{\mathbf{x}}(\bar{\mathbf{y}}_L) - \hat{\mathbf{x}}(\bar{\mathbf{y}}_B).$$

We finally have

$$\lambda(\hat{\mathbf{x}}) \approx [\hat{\mathbf{x}}(\bar{\mathbf{y}}_L) - \hat{\mathbf{x}}(\bar{\mathbf{y}}_B)]^T \mathbf{U}^T \mathbf{U} \text{Cov}(\hat{\mathbf{x}}(\mathbf{y})) \mathbf{U}^T \mathbf{U} \hat{\mathbf{x}} \quad (43)$$

where  $\text{Cov}(\hat{\mathbf{x}}(\mathbf{y}))$  is given by (41).

This equation models in a single mathematical expression all properties of the imaging process - the PET system geometry and detector response, the reconstruction algorithm, and the human visual system.

It allows us to isolate and study the effects of each component in a modular way and thus offers the potential for optimizing the system hardware and software for maximum lesion detectability, at least to the degree that the CHO model reflects true human observer performance.

By expressing the related area under the ROC curve directly as a function of the statistic [Bar90b, Bur95a], using equations (36) and (43), we can also describe the performance of the observer with a single expression that includes the features of the imaging device, the properties of the reconstruction algorithm, and the characteristics of the human visual system. Moreover, such a computation of the AUC requires only two reconstructions of the mean of data, one each for the case with and without lesion, and a modified backprojection to compute  $\kappa_j$  [Qi98c]. Compared to the Monte Carlo simulations that would otherwise be required to estimate (36), this represents a considerable advantage in terms of computational costs.

## **Simulations**

Two different kinds of simulations have been performed: one addressed the accuracy of the theoretical approximation through Monte Carlo studies and the other aimed at studying the performance of the theoretical approximation as a function of some of the key parameters that characterize PET images [Bon00].

### **The first study**

Three different data sets were considered: two were obtained from the same chest phantom (which was the same as the one used in the simulation described in the previous section; see Figure 41, left column, first two rows) with a lesion located in the right lung, whereas the third case was based on a brain phantom (Figure 42), that includes more anatomical detail than the chest one.

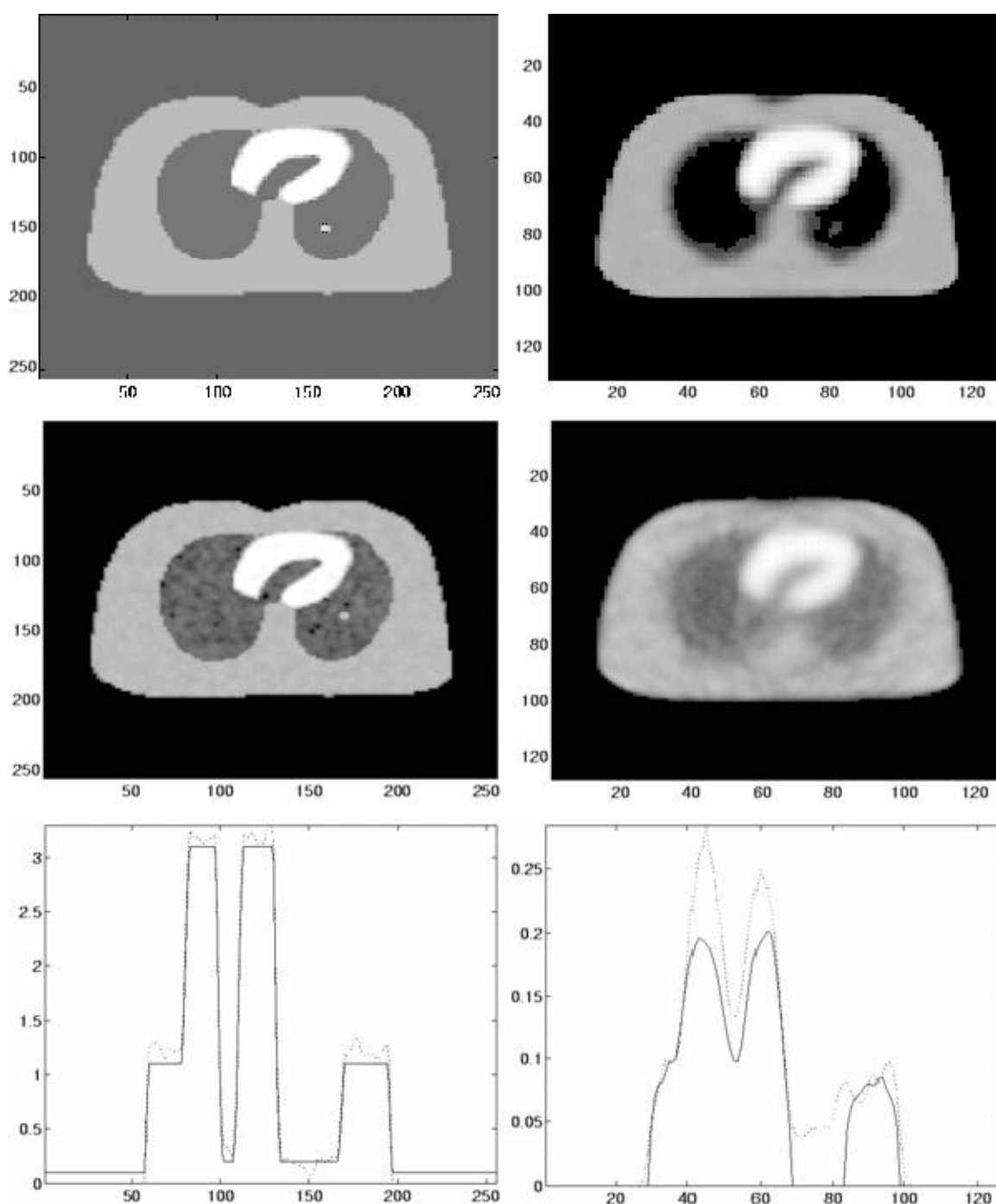


Figure 41: The transaxial plane chest phantom used in the simulations. The first row is related to the first data set: the left image is the original abnormal phantom with values for lung:heart:soft tissue of 0.1:3.1:1.1. A 3 pixel radius lesion of intensity 2 is shown in the right lung. On the right is a MAP reconstruction for  $\beta = 100$ . The second row refers to the second data set: the left image is the original abnormal phantom with values for lung:heart:soft tissue of 0:3:1 to which we added a

correlated Gaussian background with a mean of 0.2. A 3 pixel radius lesion of maximum intensity 1.1 is shown in the right lung. On the right is a MAP reconstruction for  $\beta = 100$ . The last row shows profiles of the 256x256 phantoms used for both data sets (left), and of their 128x128 reconstructions for  $\beta = 100$  (right). The profiles are taken along a vertical line passing through the heart and the right lung.

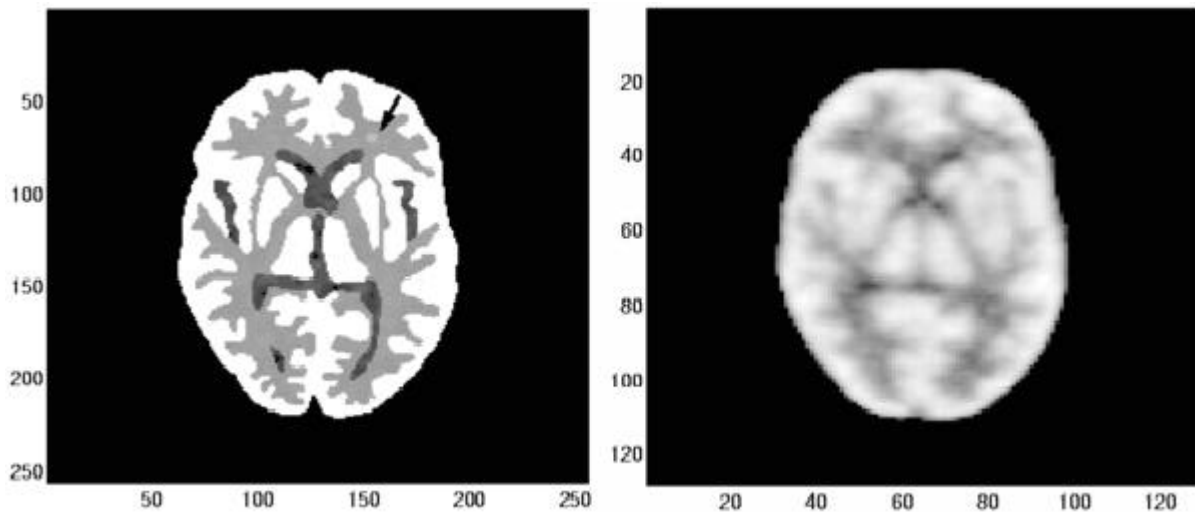


Figure 42: The 2D slice of the Hoffman phantom [Hof90] used in the simulations. Left: the original 256x256 abnormal phantom with values for gray matter:white matter:csf of 5:1:0, with a 3 pixel radius lesion of maximum intensity 0.9 in the right side of the brain, and with background variability of mean 0.2. Right: a 128x128 MAP reconstruction for  $\beta = 10$ .

In a similar way as done in the previous simulations, we built each image set from 100 sinograms obtained from a 256x256 pixel phantom; they were computed using the realistic system model that we have developed for the CTI ECAT HR+ scanner [Qi98b]. Half of the sinograms in each data set were computed from a phantom without lesion, the other half from the phantom with a lesion at a fixed location with constant activity across a three pixel radius circle.

The first of the two chest phantoms had a constant background, while in the second data set a different background was used in each phantom image by adding a smooth Gaussian random field to the lung, as illustrated in Figure 41. Each of the 144x288 element sinograms was scaled so that the mean number of counts generated was 200k and then realistic data was generated using a Poisson pseudo-random number generator. Both data sets included attenuation effects, but perfect attenuation correction factors were assumed known. Scatter was included only in the second set in which a 5% constant background was added to the sinograms before generating the pseudo-Poisson data.

Also in the last set of images a Gaussian random field was added to the white matter and the lesion was placed in 50% of the sinograms. Again, 5% constant scatter was added to the sinograms and the total sinogram scaled to a mean of 400K counts before generating pseudo-Poisson data.

2D images of size 128x128 pixels, on which to subsequently perform the Monte Carlo analysis, were reconstructed using a MAP algorithm for different values of the smoothing parameter  $\beta$ .

For each of the three sets we computed the sample mean difference  $\bar{\mathbf{f}}_L - \bar{\mathbf{f}}_B$  and the sample covariance matrix  $\mathbf{K}_U^{-1}$  for the CHO observer for two different types of channel filters: DOG and SQR with three channels in each case (Figure 34). We then computed the performance of the observer as measured by the AUC, as defined in Eq. (36).

The theoretical estimate of the AUC was obtained using equations (43) and (42). In this analysis, we included the method proposed in [Qi99f] to compensate for the effects of the non-negativity constraints used in the MAP reconstructions.

Note that instead of computing the mean difference  $\bar{\mathbf{f}}_L - \bar{\mathbf{f}}_B$  between the noiseless reconstruction of the normal and abnormal phantom, as suggested in Eq. (43), one

could also estimate it as the convolution of the function representing the lesion with the local impulse response at the center of the lesion [Qi00].

Comparisons of the two observers' performance with reference to all three sets of images are summarized in Figure 43, where the AUC values are plotted as a function of the MAP smoothing parameter  $\beta$ .

When no variability is present in the object, the two approaches show very good agreement. When background variability is included, the approximations used in the theoretical analysis have a greater influence on the final results, especially for the chest phantom. The major causes of the differences between Monte Carlo and the theoretical model are probably (i) the approximation of the mean difference with the difference of the noiseless normal and abnormal reconstructions, (ii) the assumption of space invariance used in computing the reconstructed image covariance, and (iii) the influence of the non negativity constraint on the accuracy of the covariance. Differences are also due to the finite sample size of the sets used for the Monte Carlo simulations, as described in the previous section.

### **The second study**

One of the advantages of the theoretical expressions is that we can study lesion detectability under various conditions without time consuming Monte Carlo reconstructions. As an example, we computed lesion detectability (SNR) as a function of the contrast of lesion to background, lesion size, and background noise (reflecting inhomogeneous tracer uptake).

Figure 44 shows the SNR for lesions with different contrast levels and sizes. The simulated lesion has a Gaussian shape. In general, SNR is linearly proportional to the contrast of the lesion, while it increases at a sub-linear rate as a function of size. As a result, for a fixed total lesion activity, it is easier to detect a high contrast small lesion than a low contrast large lesion.

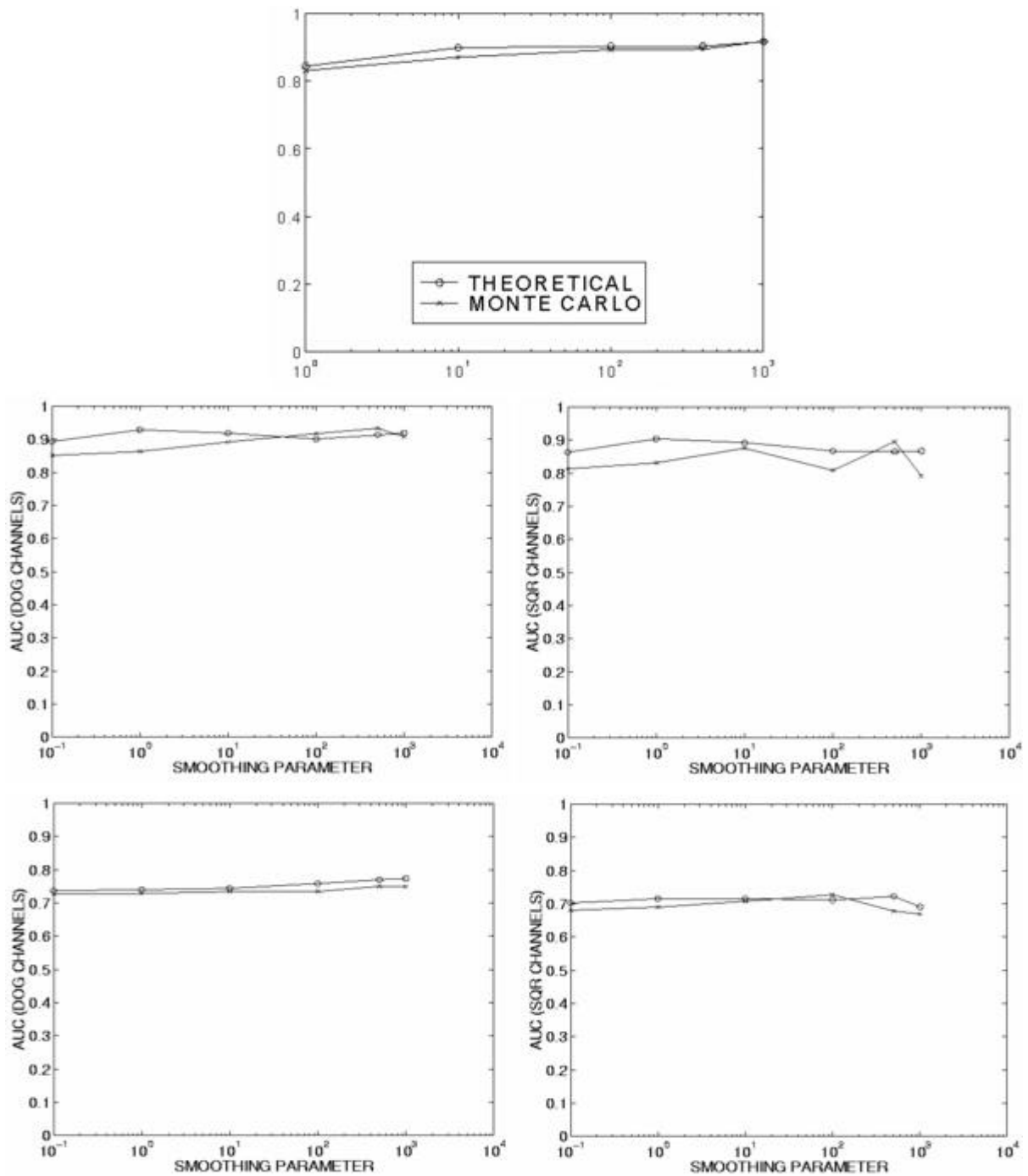


Figure 43: AUC values for the channelized Hotelling observer as a function of the smoothing parameter  $\beta$  computed both by Monte Carlo simulations (---x--) and by the theoretical approximation (---o--) on the set of (1st row) chest phantom with no variability (DOG channels) (2nd row) chest phantom with background activity (left: DOG channels; right: SQR channels) (3rd row) brain phantom with background activity (left: DOG channels; right: SQR channels).

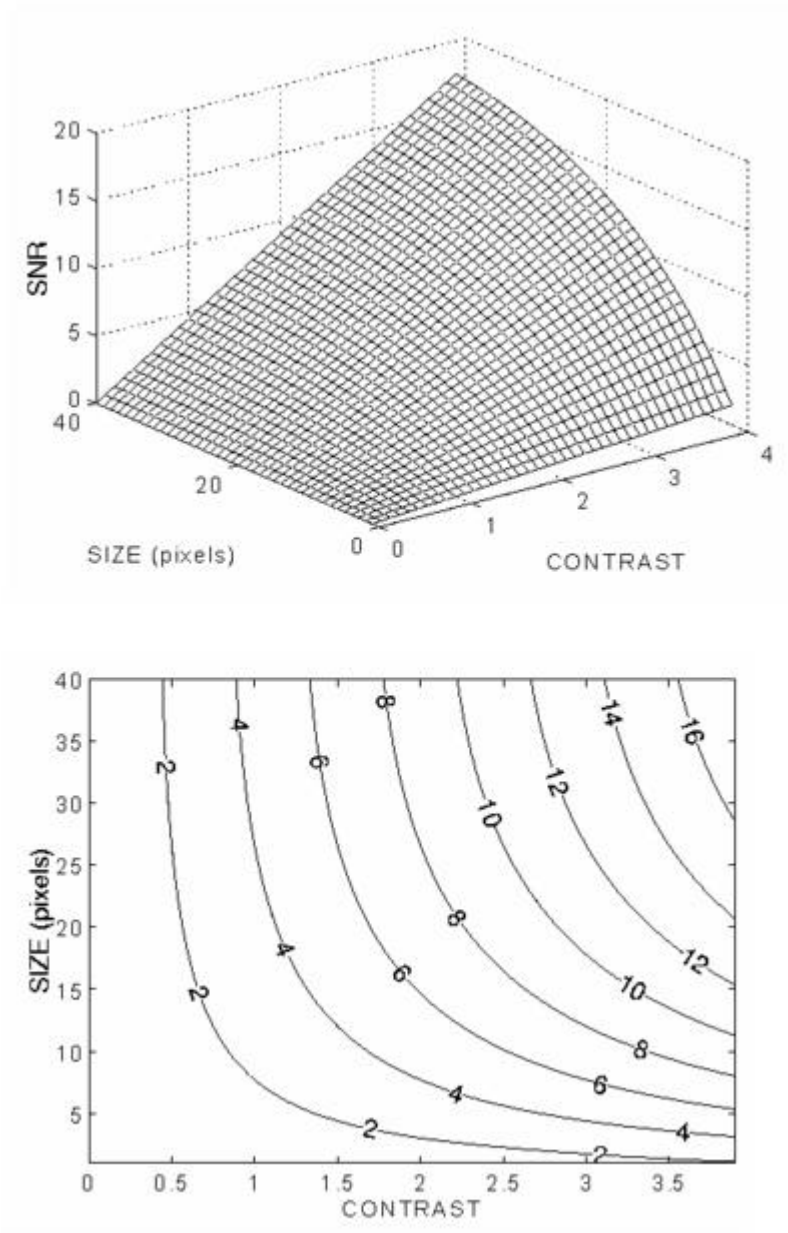


Figure 44: Surface and contour plot of the channelized Hotelling observer with SNR (DOG channels) as a function of lesion contrast and size.

In Figure 45 we plot SNR as a function of background noise and lesion contrast. The noise level is determined by the variance of the Gaussian MRF used to model the inhomogeneity in tracer uptake.

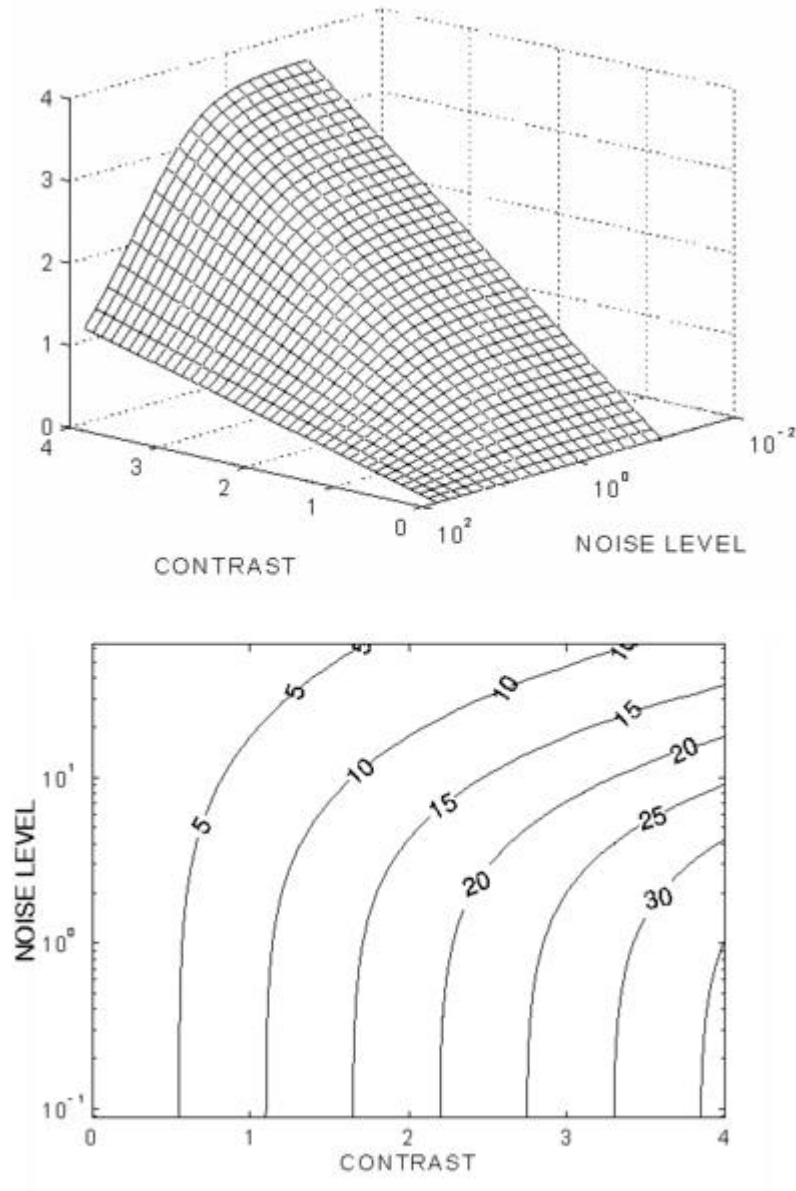


Figure 45: Surface and contour plot of the channelized Hotelling observer with SNR (DOG channels) as a function of background noise level and lesion contrast.

The computational complexity of this study is a function of the number of conditions considered: to plot the surface imaged in Figure 45 for instance, one has to compute two reconstructions along with a modified backprojection for each combination of lesion size and contrast of lesion to background - in our case 40 x 40; considering that a single 2D 20 iterations MAP reconstruction runs in about 1:50 min<sup>19</sup> on a 4 processor Pentium II 400MHz, the time complexity turns out to be on the order of a couple of days.

To obtain the same results by a Monte Carlo study, each of the 40 x 40 SNR values would require  $n$  reconstructions instead, where  $n$  is the number of samples used in the Monte Carlo simulation to estimate the mean and covariance for the CHO statistic, and should reasonably be in the order of a hundred. The computational complexity in this latter case is thus a function of both the number of conditions and the number of samples. In our example, by choosing  $n = 100$  and considering the same system as above, the whole study would require over 200 days!

## **Conclusion**

Computer observers are becoming a popular alternative to human observers for performing psychophysical studies to assess image quality and performance of imaging systems and reconstruction algorithms. We have presented a theoretical approach to reducing the computational costs of linear observer statistics developed for the task of lesion detection in tomographic images. Studies using the channelized Hotelling observer for nonlinear MAP image reconstruction methods showed our model to be a fairly accurate and very low cost alternative to the traditional Monte Carlo studies. Using chest and brain phantoms, we have shown the influence of smoothing parameter, lesion contrast, lesion size and background noise level on CHO performance.

---

<sup>19</sup> This includes an offset time spent on initialization and calibration procedures, and thus it does not reflect the efficiency of a 63 plane 3D reconstruction.

More generally, these closed form theoretical expressions allow us to compute observer performance over a large variety of parameter settings (including the system hardware configuration and reconstruction methods) and imaging features in order to study their effects on lesion detectability.

## Human observers

The Human Observer study described in this section has been performed in response to two considerations:

First, results of several quantitative studies presented in literature [Bou96, Fes96a, Fes96b, Her91] about the efficiency of statistical approaches to image reconstruction, as well as those performed by members of our group over the past few years [Mum96, Qi98b, Qi99a, Qi99f], provided the stimulus to further analyze the MAP algorithm and gain a wider view of its accuracy, by including into the exam investigations from a qualitative point of view. In particular, we were interested in analyzing the usability of our method in a clinical environment, addressing one of the major applications of FDG PET, namely, the localization of small tumoral lesions: the identification of metastases and involved lymph nodes and the detection of solitary foci of elevated uptake were deemed a considerable measure of algorithm performance.

Second, as has been pointed out in the concluding part of the previous section, computer observers still require several improvements in order to completely fulfill their potential utility. So far, they can reliably reproduce human performance only under specific conditions and, most importantly, they still do not represent a full substitute of the human ones when real clinical data have to be analyzed, since complex studies of the image properties and variabilities need to be performed preliminarily and implemented into the observer model.

## **The study**

The study we present had already been performed, with only slight differences, by Thomas Farquhar at the University of California at Los Angeles, and is thoroughly described in [Far98] and [Far99]. We refer to those references for the details and restrict here the discussion to an outline of the most fundamental issues and the aspects that differ from the references mentioned above.

### **Data set**

The study consists of the evaluation of patients with suspected lung cancer. The choice of this specific case is based on clinical considerations: in recent years FDG PET has gained considerable attention and general acceptance for the staging of lung cancer as well as for the diagnosis of solitary pulmonary nodules [Dew93, Duh95, Gup96, Hag97, Kni96, Pat95].

The main data set is based on 100 whole body PET scans of healthy volunteers, imaged on an ECAT EXACT HR+ 962 PET device. Each scan is composed of 5 caudal bed positions, extending from the legs up to beyond the top of the shoulders in order to include the apices of the lungs; however, only the upper three bed positions were used for evaluation. Data were acquired both in 2D and 3D mode, so that both 2D and 3D reconstruction algorithms could be used. Beyond emission, transmission scans were also acquired that were subsequently processed in order to compensate for attenuation.

50 abnormal scans were created by adding a simulated lesion to half of the normal data set. In order to provide the most possibly realistic setting, instead of using simple geometric shapes twenty-two lesions were segmented from X-Ray Computed Tomography images of patients with biopsy-proven lung cancer; moreover, the lesion locations chosen were verified by a nuclear medicine physician. The process was repeated both for the 2D and the 3D case.

The addition of a lesion to a normal scan performed by Dr. Farquhar and summerized above requires in the practice various considerations about sampling, accurate simulation of PET acquisition and compensation of several geometric and physical effects, and thus turns out not to be a trivial task. It is very well sketched in [Far99] by means of a diagram.

An additional, smaller data set was also created in a similar way and was then used for training purposes in a preliminary phase of the image evaluation.

### **Reconstructions**

In order to obtain a possibly objective assessment of the MAP algorithm, evaluation of FBP images was also considered, so that the two methods could be compared with each other. In fact, due to its low computational cost, FBP is nowadays the most widely accepted method in clinical scenarios and, thus, very well suits to the role of reference point in a comparison of different approaches<sup>20</sup>.

Various implementations of the FBP are taken into account, namely, 2D FBP with no attenuation correction (AC), 2D with segmented attenuation correction and 3D with no AC. As regards the MAP scheme, a 2D implementation is addressed, with AC based on correction factors reprojected from an attenuation image also reconstructd with a MAP, iterative algorithm on the original transmission and blank scan data [Qi98b]. 20 iterations are performed, with a 3D quadratic prior and smoothing parameter  $\beta$  set to 2000. These parameters were chosen on an empirical basis to provide satisfactory image quality.

In the reconstruction process none of the algorithms modeled any scatter correction.

---

<sup>20</sup> The same choice was taken in the study presented in the first part of this dissertation, dealing with the 2D+1 projection model.

50 normal + 50 abnormal scans were reconstructed with all four methods, thus producing a set of 400 images. Three consecutive coronal planes of dimension 256 x 193 each were extracted from the reconstructions: the planes covered a z-extent correspondent to the upper three bed positions, because these were the only ones necessary to image the field of view appropriate for an evaluation of a patient suspicious for lung cancer. In the case of abnormal images, the central plane was centered on the lesion.

### **Observers**

In his study Dr. Farquhar chose as observers four nuclear medicine physicians, in that they were already familiar with the interpretation of PET images and the task of lesion detection. At the same time, however, they were trained on interpreting FBP reconstructions only and had no acquaintance with the MAP approach; this might have influenced the outcome of the analysis, favoring one method rather than the other. For this reason, we chose here “non-trained observers” (engineering graduate students), i.e. personnel with no previous experience at reading one specific type of reconstruction, yet familiar enough with the basic concepts of inversion algorithms and owning the necessary knowledge to evaluate images in the task of tumoral lesion detection.

### **Image presentation and evaluation**

An apposite graphical interface was developed in Matlab (Figure 46 and Figure 47) to present the triplets to the readers and save their results for later evaluation.

In accordance with Dr. Farquhar’s study, the observers were instructed to consider the following clinical scenario:

*“For each image you are to assume that you are viewing the study of a patient with a presentation and history suspicious for lung cancer with any possible associated metastases. In rating each image, you are to consider the possible presence of a lesion or abnormality. A lesion or abnormality is to include BOTH malignant disease AND benign, inflammatory processes.”*

Reconstructions were presented to the reader in random order, each exactly once; the three coronal planes were visualized simultaneously and the central plane (displayed in the middle) was the one to be evaluated. Observers were allowed to adjust the color scale by modifying the upper and lower threshold, inverting the scale and change the Gamma correction factor.

They were to point the most probable lesion location, by clicking on the appropriate spot in the image. Also, they had to indicate the degree of certainty of their answer by rating each triplet using a continuous scale from 1 to 5. The ratings could be thought of as answers to the question “Does the image contain an abnormality?” with the following meanings: 1 = definitely no; 2 = probably no; 3 = maybe; 4 = probably yes; 5 = definitely yes.

Image evaluation was performed in two sessions: a training session and the study. The purpose of the first session (see Figure 46) was to get the readers familiar with the task of lesion detection, with the interface and with manipulating the color scale in order to better enhance the characteristics and details of the reconstruction.

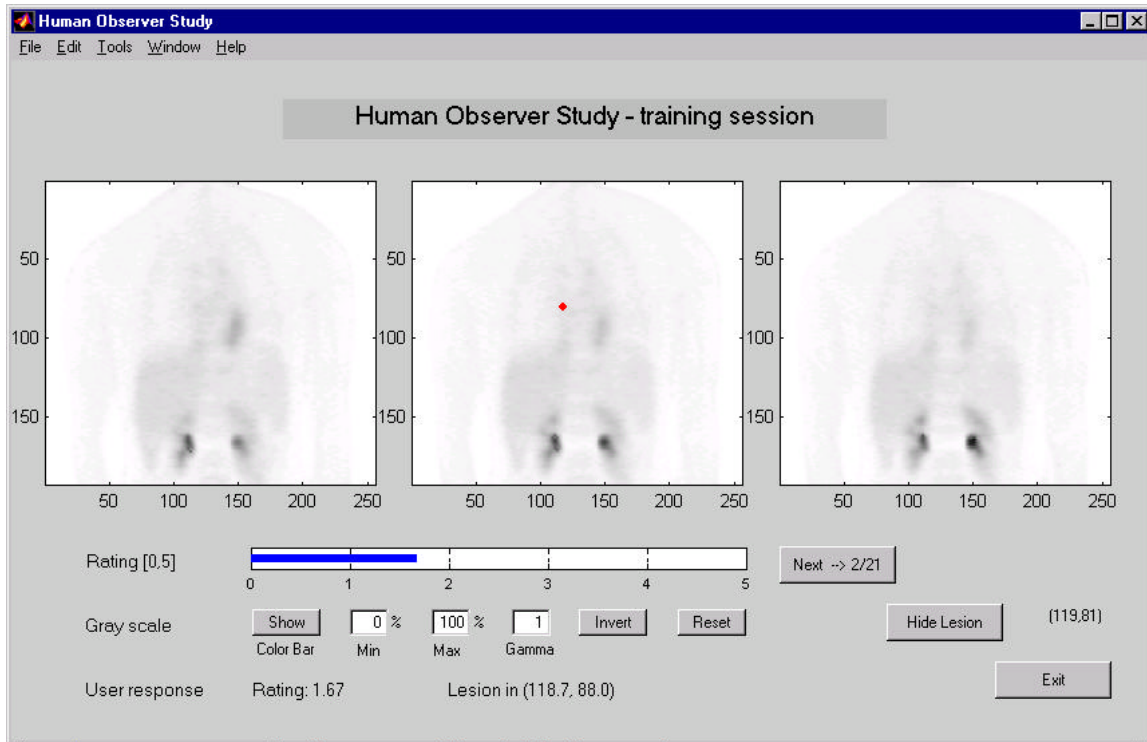


Figure 46: The graphical interface used by the readers for image presentation and evaluation. In addition to the normal operations in the training session the software allows the observers to find out about the details of the image: nature of the triplet as a true negative or a true positive and lesion location in true positive images.

In this modality the Matlab program also provided the user with information about the real nature of the image (true positive or true negative), and, in case of true positives, with the exact lesion location, by superimposing a dot on the central image and displaying the location coordinates. The training set consisted of about as many images as were used in the study, since the readers had little previous experience at the task of lesion detection.

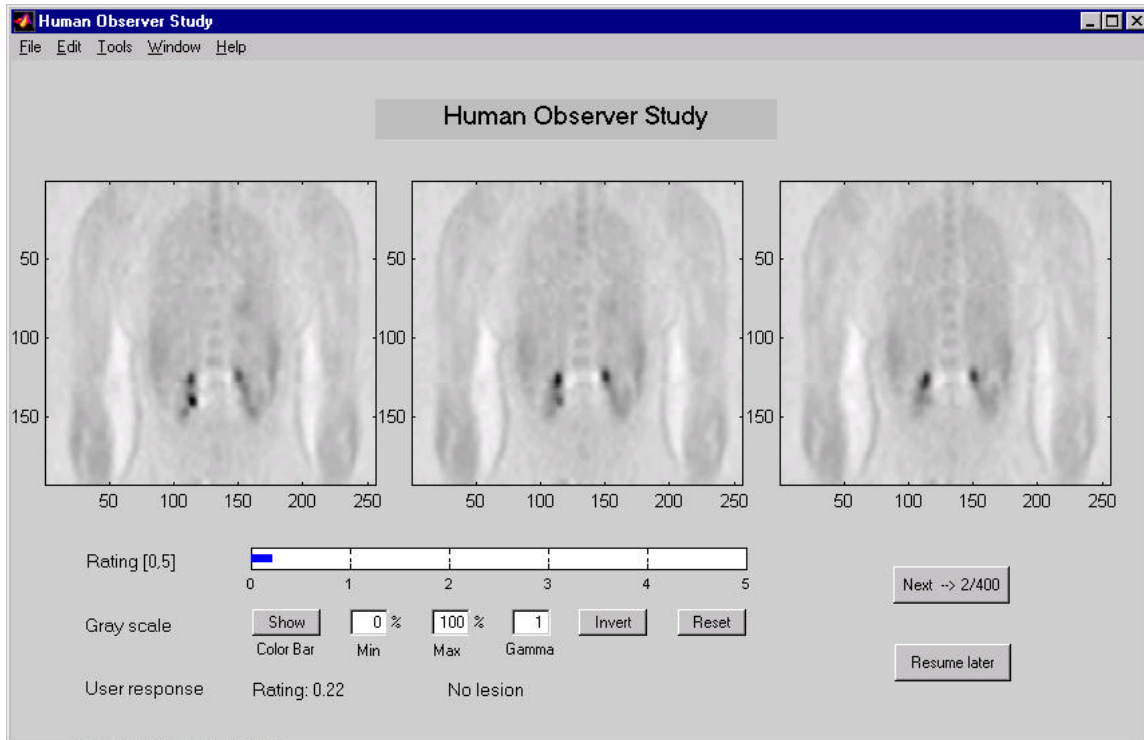


Figure 47: The graphical interface used by the readers for image presentation and evaluation. In the study session observers do not get any feedback about the true nature of the image. Their responses are saved in order to be later analyzed by the ROC/LROC software.

The study session (see Figure 47) followed the training one. The main features – color scale manipulation and rating - presented no differences with the first part. However, no information was available about the nature of the triplet or the lesion location in the case of true positives. Moreover, the observer's results were saved to disk, in order to be later processed by the ROC/LROC software.

In this session 400 images were presented in random order and also randomized between the readers, in order to further reduce any biases or reader-order effects. The readers were encouraged to minimize fatigue and inattention by freely limiting the number of triplets evaluated in a single session. For this purpose, a botton

<Resume later> was added to the interface, allowing the user to pause the session at any time and resume without having to repeat the evaluation of the same images twice. The average total time needed to perform the entire study was about 6-8 hours for each reader.

### **ROC and LROC Analysis**

The observer results were evaluated by both an ROC and an LROC analysis: as mentioned in the Overview section, these are nowadays well established methodologies for statistically quantifying and characterizing the performance of observers at binary tasks such as lesion detection [Bur77, Met86, Met89, Sta75, Swe96].

For the sake of consistency with the evaluation performed in [Far99], we used the same binormal fitting routine of the CORROC2 program developed at the University of Chicago by Metz et al. [Met84]. The matched pair design requires the same data to be reconstructed with different modalities and then pairwise compares the ratings from each modality of the same image: in this way, an accurate analysis is ensured and correlation is minimized. For both modalities being compared, the CORROC2 program calculates a binormal curve fit, the area (AUC) under the fitted ROC curve, a standard error (SE) of the estimate of the AUC and a probability value to indicate the likelihood of statistical significance of the difference between the AUC values of the two modalities compared. The null hypothesis assumed here was that all four modalities were equivalent.

A second analysis also dealt with the readers' responses concerning the lesion location. For this purpose, an LROC program developed by Swensson [Swe96] was used - the same as referred to in [Far99]. This program evaluates one modality at the time and computes both the LROC and the ROC curves, and the related AUC values, along with an estimate of the standard errors. Subsequently, a student *t*-test for paired data was performed, with the goal of ascertaining the statistical significance of the differences between modalities observed across readers.

Comparison with the significance values of the ROC analysis was made possible by converting the  $t$  statistic to a probability value.

## **Results and discussion**

### **Summary of the results reported in [Far99]**

The original aim of the study, as conceived by Dr. Farquhar, was to compare different approaches in reconstruction; in particular, the study addressed four issues by making four pairwise comparisons:

2D acquisition and 2D FBP reconstruction with no attenuation correction versus 3D acquisition and 3D FBP reconstruction again without AC, in order to isolate the effects of 2d and 3D acquisition: the ROC results suggest that the additional burden of reconstructing 3D data are not deemed to be worthwhile.

2D FBP with no AC versus 2D FBP with segmented AC, addressing the relevance of attenuation correction: the additional computational burden of compensating for attenuation does not seem to improve performance in lesion detection, when data are reconstructed by means of the FBP algorithm.

2D FBP with segmented AC versus 2D MAP with MAP-based attenuation correction, evidencing the benefits of an iterative approach when compensating for attenuation: images reconstructed by the former method are shown to have markedly degraded detection performance.

2D FBP without AC versus 2D MAP; this comparison considers the currently most widely used clinical protocol with a supposedly more accurate method, developed with the aim of reducing noise, which is one of the major disturbing factors in the task of lesion detection. Although MAP reconstructed images produce better results than FBP ones at the task of lesion detection, the improvement is not statistically significant: it does not merit the computational burdens due to the lengthy iterative reconstruction approach, to acquire a transmission scan and compute the attenuation correction.

These comparisons with the respective results are sketched in Figure 46.

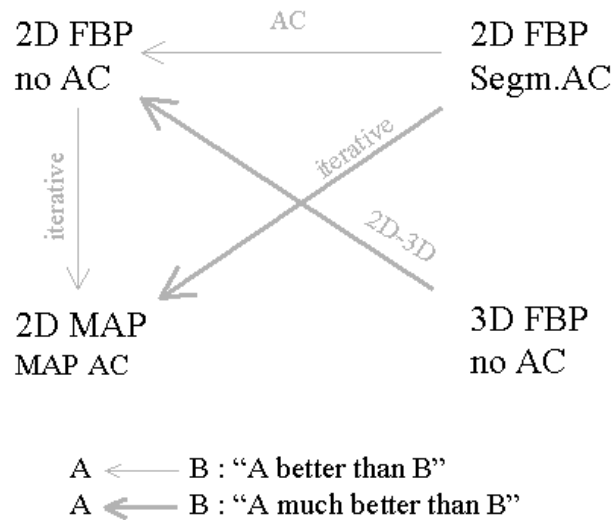


Figure 48: Scheme of the pairwise comparisons of the study and the respective results.

Our main goal here is, rather than to generically compare different reconstruction settings, to study whether the MAP algorithm outperforms the FBP one at the task of lesion detection and if it can thus be taken into consideration as an advantageous replacement of the latter. For this reason, we mainly focus on the comparison between 2D MAP with MAP-attenuation correction and 2D FBP with no attenuation correction, since these were already shown to be the two “top” approaches among the four included in the study. Moreover, this particular implementation of the FBP method is the one most widely used in clinical settings.

## **Results classification**

Before running the ROC and LROC studies, a first rude analysis of the results obtained by the observers was done: it consisted in classifying the answers for each method and for each observer into six groups, depending on both the rate given by the reader and the nature of the image. More specifically, the six groups were:

Normal images, rated from 0 to 2: these give a rough estimate of the TN fraction.

Normal images, rated between 2 and 3: they represent the images for which the answers were not quite certain.

Normal images, with grades from 3 to 5: they can be thought of as an FP fraction.

Likewise, the abnormal images fell into three classes:

Abnormal images with rates between 0 and 2, i.e. negative images for which the reader was not able to find the lesion: they represent an estimate of the FN fraction.

Abnormal images rated from 2 to 3: these are the reconstructions for which the observer was uncertain about the presence of a lesion or not.

Abnormal images graded between 4 and 5: they represent the TP fraction.

The number of images falling into each group was computed for each observer and also for all observers pooled together. The average grades of the “border” classes (TN, FP, FN and TP) as well as the average grades given over the entire normal and, respectively, abnormal sets of images were also calculated. Finally, in the case of abnormal images, we computed the fraction of wrong location estimates for each group. These results are summarized in Table 4 for each single observer and in Table 5 for an average of the results over all observers.

<i>Observer B</i>	<b>Normal images (no lesion)</b>				<b>Abnormal images (with lesion)</b>			
<b>Rating</b>	[0, 2]	(2, 3)	[3, 5]	Average	[0, 2]	(2, 3)	[3, 5]	Average
<b>MAP 2D</b>	32	2	16		12 (10)	0 (0)	38 (6)	
<b>w/ AC</b>	0.62		3.63	1.68	0.46		4.48	3.51
<b>FBP 2D</b>	36	10	4		14 (11)	7 (4)	29 (5)	
<b>no AC</b>	0.77		3.74	1.36	0.62		4.20	2.98
<b>FBP 2D</b>	31	14	5		24 (23)	13 (11)	13 (3)	
<b>segm. AC</b>	0.67		3.66	1.48	0.69		4.00	2.04
<b>FBP 3D</b>	28	15	7		30 (27)	10 (9)	10 (3)	
<b>no AC</b>	0.89		3.57	1.74	0.87		4.26	1.90

<i>Observer P</i>	<b>Normal images (no lesion)</b>				<b>Abnormal images (with lesion)</b>			
<b>Rating</b>	[0, 2]	(2, 3)	[3, 5]	Average	[0, 2]	(2, 3)	[3, 5]	Average
<b>MAP 2D</b>	35	5	10		14 (6)	0 (0)	36 (1)	
<b>w/ AC</b>	0.38		3.75	1.28	0.68		4.79	3.64
<b>FBP 2D</b>	39	7	4		14 (12)	4 (2)	32 (6)	
<b>no AC</b>	0.57		3.58	1.08	0.89		4.20	3.15
<b>FBP 2D</b>	36	13	1		25 (23)	15 (10)	10 (2)	
<b>segm. AC</b>	1.05		3.03	1.42	0.91		3.71	1.94
<b>FBP 3D</b>	28	12	10		30 (27)	7 (6)	13 (7)	
<b>no AC</b>	0.57		3.59	1.60	0.72		3.75	1.75

<i>Observer J</i>	<b>Normal images (no lesion)</b>				<b>Abnormal images (with lesion)</b>			
<b>Rating</b>	[0, 2]	(2, 3)	[3, 5]	Average	[0, 2]	(2, 3)	[3, 5]	Average
<b>MAP 2D</b>	38	1	11		17 (16)	0 (0)	33 (3)	
<b>w/ AC</b>	0.50		3.87	1.28	0.47		4.80	3.33
<b>FBP 2D</b>	38	3	9		26 (26)	0 (0)	24 (4)	
<b>no AC</b>	0.41		4.03	1.20	0.45		4.59	2.44
<b>FBP 2D</b>	34	6	10		33 (31)	3 (3)	14 (5)	
<b>segm. AC</b>	0.81		3.84	1.65	0.69		4.50	1.88
<b>FBP 3D</b>	33	4	13		30 (30)	1 (1)	19 (14)	
<b>no AC</b>	0.70		4.27	1.79	0.63		4.19	2.02

<i>Observer E</i>	<b>Normal images (no lesion)</b>				<b>Abnormal images (with lesion)</b>			
<b>Rating</b>	[0, 2]	(2, 3)	[3, 5]	Average	[0, 2]	(2, 3)	[3, 5]	Average
<b>MAP 2D</b>	20	6	24		5 (5)	2 (1)	43 (6)	
<b>w/ AC</b>	0.82		3.93	2.54	0.57		4.31	3.86
<b>FBP 2D</b>	33	5	12		11 (11)	3 (3)	36( 4)	
<b>no AC</b>	0.99		3.55	1.77	0.60		4.41	3.46
<b>FBP 2D</b>	36	8	6		22 (22)	10 (4)	18 (7)	
<b>segm. AC</b>	1.05		3.38	1.55	1.02		3.91	2.39
<b>FBP 3D</b>	27	7	16		23 (23)	5 (3)	22 (16)	
<b>no AC</b>	1.17		3.66	2.17	0.92		3.89	2.41

Table 4: Classification of the results of each single observer, over a set of 400 images. In each row the first number denotes the number of images classified into that specific class while the second number (below the first one) is the average rating given over that class. The two rightmost columns of each half of the table represent the average rating over the set of normal, respectively, abnormal case. Numbers in brackets denote the number of wrong location estimates over that specific group.

<i>All</i>	<b>Normal images (no lesion)</b>				<b>Abnormal images (with lesion)</b>			
<b>Rating</b>	[0, 2]	(2, 3)	[3, 5]	Average	[0, 2]	(2, 3)	[3, 5]	Average
<b>MAP 2D</b>	125	14	61		48(37)	2( 1)	150(16)	
<b>w/ AC</b>	0.55		3.81	1.69	0.54		4.57	3.58
<b>FBP 2D</b>	146	25	29		65(60)	14( 9)	121(19)	
<b>no AC</b>	0.67		3.73	1.35	0.61		4.34	3.01
<b>FBP 2D</b>	137	41	22		104(99)	41(28)	55(17)	
<b>segm. AC</b>	0.90		3.64	1.53	0.82		4.04	2.06
<b>FBP 3D</b>	116	38	46		113(107)	23(19)	64(40)	
<b>no AC</b>	0.82		3.80	1.83	0.78		4.01	2.02

Table 5: Classification of the results of all four observers pooled together. The total number of responses analyzed is 400 x 4, corresponding to the same set of 400 images evaluated by four different observers.

Although this is only a rough analysis, the overall trend of the study appears clearly and some significant considerations can already be made.

The most interesting observation concerns the sensitivity in MAP reconstructions, i.e. the reliability of this method in recovering abnormalities in scans of ill patients. The number of True Positive is the highest, when compared with the same value referring to other methods; this is true not only for the results of all observers pooled together, but also for each single observer. Also the fraction of correctly located lesions is the highest in MAP reconstructions and the average rating in the interval [4,5] is the highest, which means that all readers were quite confident in evaluating these group of images.

This conclusion about the sensitivity of the MAP approach is further confirmed by the values reported in the second column of the abnormal case: the number of responses that denote uncertainties are extremely low - three observers out of four did not rate any single abnormal image with a grade between 2 and 3, which means that they had little uncertainties when rating MAP reconstruction of abnormal scans. This is almost never the case for the other approaches.

Finally, the left column of the abnormal section, representing an estimate of the False Negatives, has once again by far the lowest values in the case of the iterative approach. It is to be noted that the number of incorrect locations is not significant here, since many readers did not specify any location at all, when they believed an image to be normal. Once again, the average rating is the lowest in the case of the MAP algorithm, which can be interpreted as a more secure and confident attitude of the observers while rating this kind of reconstructions.

The same conclusion can be drawn by comparing the average rating over the entire class of abnormal images: the iterative case reports the highest scores.

Unfortunately, as far as the specificity aspect is concerned, the analysis of the MAP performance does not turn out to be as promising. Here, one would like to have possibly high TN values with low average rating (leftmost column) and low FP values with high average grades (third column). While the average ratings meet these expectations, this is not true for the number of images belonging to the TN and FP classes. In particular, results for the FP fraction diverge from a desirable behavior and denote a weakness of the MAP approach in eliminating suspicions of abnormalities when no lesions are present in the scan. A more low-level analysis on the results collected from the observers has shown that, in some cases, more than one reader (and sometimes even all of them) has pointed to the very same lesion location when evaluating the same TN MAP image and classifying it as FP. An example of such a reconstruction is shown in Figure 49 for the 2D FBP case without AC and in Figure 50 for the MAP case, which was wrongly interpreted by all observers. Similar examples are shown in Figure 51.

The negative trend of MAP with respect to the specificity aspect already showed up in the study performed by Dr. Farquhar, although in a less pronounced way; the reason might be that physicians were more familiar with the physical properties of tumoral nodes and know how to distinguish them from other types of (non cancerous) spots.

Another interesting observation regards a comparison of the 3D mode with the 2D ones: the inferior detection performance of the former seems to result in an improved sensitivity and suggests that a 3D implementation of the MAP algorithm might lead to more sensitive detection results than the currently used 2D version. In [Far98] it is speculated that this improvement of the 3D case results from a decreased image contrast due to unsatisfactory corrections for scattered and random events as well as to reduction in dose and scan time.

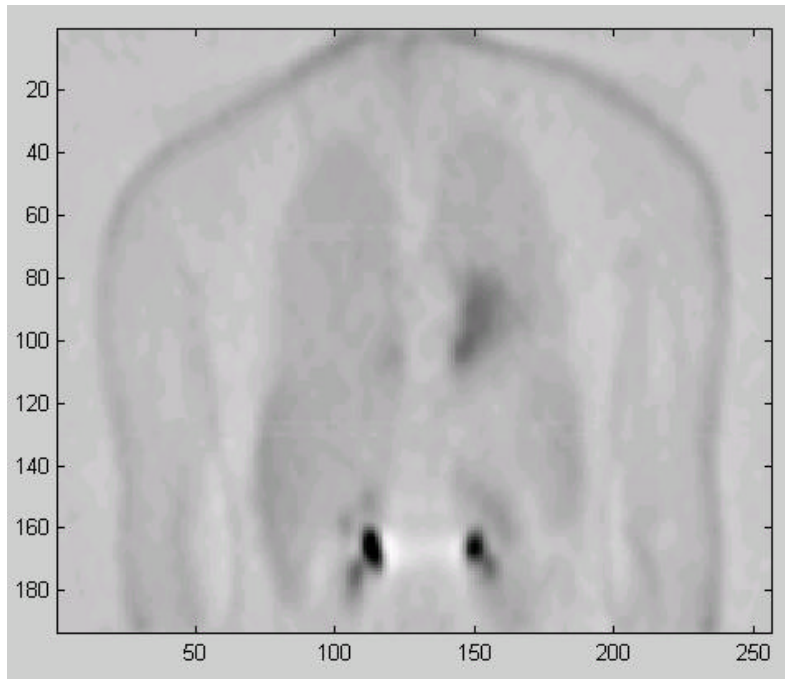


Figure 49: 2D FBP reconstruction without attenuation correction of TN data.

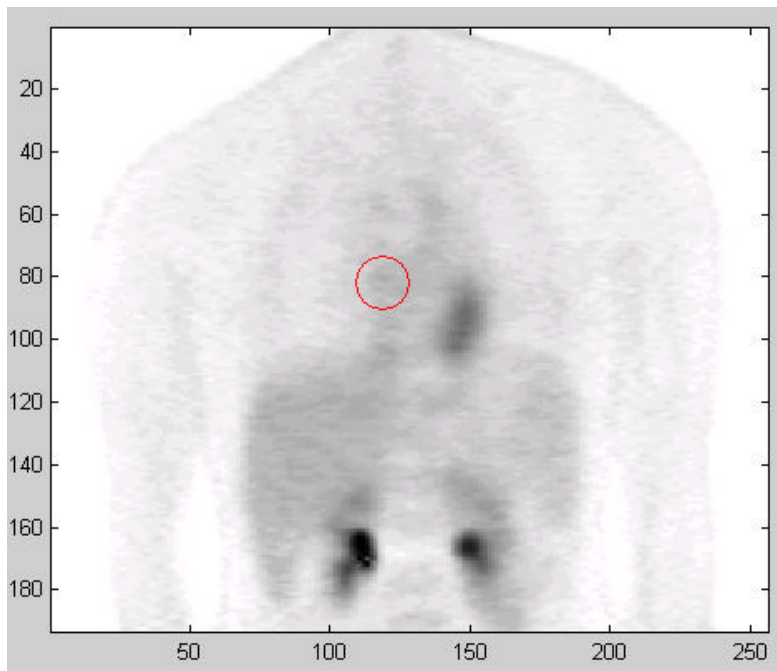


Figure 50: 2D MAP reconstruction of the same TN data of Figure 49. All observers believed this image to be TP and indicated the very same location (red circle) for the suspected lesion.

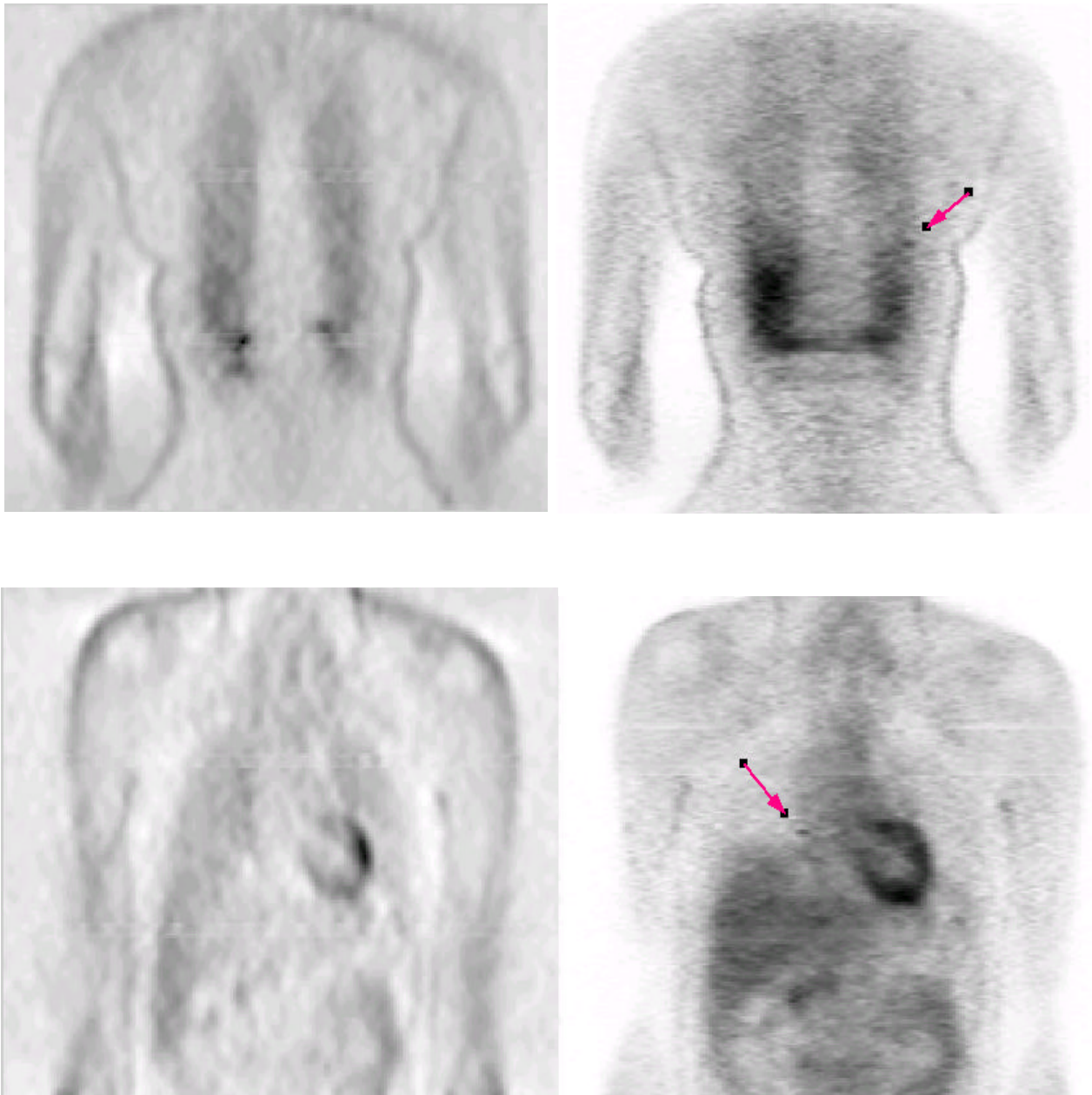


Figure 51: Other examples of TN images. Left: FBP reconstruction. Right: the respective MAP reconstruction, with a pink arrow pointing to the spot that the observers wrongly believed to be a lesion. (The horizontal artifacts at 1/3 and 2/3 of the images correspond to the intersection of the different bed positions).

## **The ROC study**

The results of the study are shown in Table 6.

In summary, the measured improvement using MAP compared to FBP 2D without AC was not found to be statistically significant. For the other comparisons of MAP with FBP, the results were statistically significant with  $p$ -values of less than 0.01.

As already mentioned, we are mainly interested in the comparison between 2D FBP without AC and 2D MAP with MAP attenuation correction. This comparison is somehow twofold because two different issues are involved: the use or not of AC and an iterative vs. a linear approach in reconstruction.

Concerning attenuation correction, we note that in the MAP case detection results might be degraded because emission and transmission data, from which MAP-AC factors are computed, can be slightly misregistered: in fact, transmission data are obtained by pre-injection long before the start of the emission acquisition and during this time patients are likely to move, although they were strapped to the bed.

Despite this possible source of artifacts, the performance of the MAP approach is shown to be slightly better than that of the FBP method without, even if this is not established with statistical significance.

A comparison with the FBP scheme with segmented attenuation correction is also worth. In fact this method, as opposed to the MAP one, is supposed to reduce the random noise in the AC factors, and the standard error due to not accurately chosen attenuation values should be minimized. Thus, its worst performance compared to MAP is to be attributed to noise amplification resulting from applying large AC factors to noisy, low count emission data, rather than to an error in the AC factors. Conversely, the MAP method is proven to nicely minimize noise amplification.

	<b>B</b>	<b>E</b>	<b>P</b>	<b>J</b>	<b>Average</b>
<b>FBP 2D NoAC</b>	<b>.7763</b>	<b>.7665</b>	<b>.8191</b>	<b>.6968</b>	<b>.764675</b>
	.0489	.0519	.0435	.0523	.04915
MAP 2D Map AC	.6367	.9418	.5002	.4283	
FBP 2D seg AC	.0461	.2306	.0165	.0315	
FBP 3D no AC	<u>.0009</u>	<u>.0028</u>	<u>.0001</u>	.0218	
<b>MAP 2D Map AC</b>	<b>.8079</b>	<b>.7716</b>	<b>.8588</b>	<b>.7538</b>	<b>.798025</b>
	.0455	.0474	.0398	.0494	.045528
FBP 2D no AC	.6367	.9418	.5002	.4283	
FBP 2D seg AC	<u>.0125</u>	.1866	<u>.0022</u>	<u>.0031</u>	
<b>FBP 2D seg AC</b>	<b>.6295</b>	<b>.6769</b>	<b>.6507</b>	<b>.5293</b>	<b>.6216</b>
	.0550	.0538	.0551	.0578	.055425
FBP 2D no AC	.0461	.2306	.0165	.0315	
MAP 2D Map AC	<u>.0125</u>	.1866	<u>.0022</u>	<u>.0031</u>	
<b>FBP 3D no AC</b>	<b>.5238</b>	<b>.5334</b>	<b>.5442</b>	<b>.5187</b>	<b>.530025</b>
	.0580	.0581	.0574	.0575	.05775
FBP 2D no AC	<u>.0009</u>	<u>.0028</u>	<u>.0001</u>	.0218	
FBP 2D seg AC	.1859	.0699	.1806	.8967	
MAP 2D Map AC	<u>.0000</u>	<u>.0002</u>	<u>.0000</u>	<u>.0008</u>	

Table 6: ROC results for four “non-trained” human observers. The Area under the fitted binormal ROC curve (**AUC**) is indicated in bold for each of the modalities investigated. Immediately beneath the AUC values are estimates of the standard error. Also shown are the two-sided p-values for each of the inter-modality comparisons. *P*-values which are considered statistically significant are underlined.

A visual inspection of images reconstructed iteratively, compared to those obtained by FBP, shows that there are dramatic differences in the noise patterns and other features of the images that profoundly affect their quality. Despite this observation, ROC results only feebly evidences the superiority of the MAP approach, and it was not possible to establish this improvement with statistical significance.

The use of a larger set of images might help in providing stronger significance or, conversely, a restricted set of data, including only lesions with specific characteristics, might evidence the MAP superiority. It is also possible that the benefit of iterative reconstruction is limited by the effects of attenuation correction, that amplify noise: the profound improvement of MAP compared to FBP with segmented attenuation correction might represent a proof of this speculation.

The not too promising results of the ROC study concerning MAP and FBP with no AC still allow us to draw some conclusions regarding a comparison between a more general class of iterative methods and the pure FBP approach with no AC modelling: on the one hand, MAP represents an improvement over accelerated algorithms such as OS-EM and iterative methods without an accurate system model, as has been shown in objective measures as for instance contrast recovery and noise variance; on the other hand, no improvement has been shown with statistical significance over the FBP method for the task of lesion detection. Hence one can conclude that it is highly unlikely that the general class of simplistic, accelerated algorithms presents any benefit over FBP.

Before concluding it is worth comparing the results of this study with those obtained in [Far99], using radiologists and doctors as observers, who were already familiar with reading FBP reconstructions. Surprisingly, no particular difference appears between the two studies, except for the fact that the AUC values computed for the “non-trained” observers are slightly lower than in the former study. Both cases evidence the superiority of the MAP approach over the different FBP versions, but no statistical significance can be established for the comparison of MAP with 2D FBP without AC, which is the most widely used FBP variant in clinical settings. Also

all AUC values are very similar over the two studies, both for each individual reader and for the average values<sup>21</sup>.

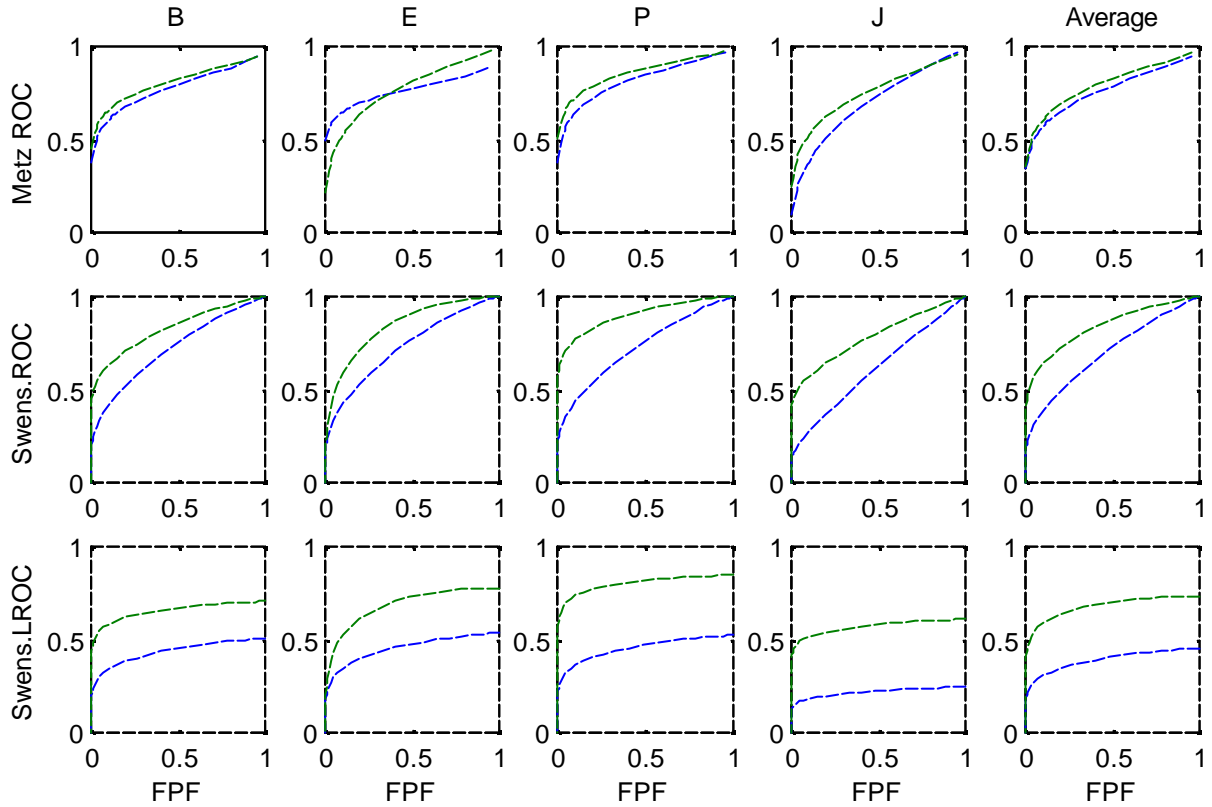


Figure 52: ROC and the LROC curves for MAP (green line) and 2D FBP w/out AC (blue line) for every single observer and for the average over all readers. Two different kinds of ROC curves are presented, that were obtained by computing the AUC values in different a way, as described in the text.

---

<sup>21</sup> In this study no jack-knife analysis of pooled ROC data was performed.

## The LROC study

The results of the LROC study are summarized in Table 4 (AUC values) and Table 8 (localization accuracy, or probability of localization, and statistical error). Figure 52 shows plots of the LROC curves, while Table 9 summarizes the  $p$ -values relative to the comparison of MAP and 2D FBP without AC, both for our study and, as a point of reference, for the study described in [Far99].

LROC (AUC)	<b>B</b>	<b>E</b>	<b>P</b>	<b>J</b>	<b>Average</b>
<b>FBP 2D NoAC</b>	0.4377	0.5361	0.4564	0.2221	0.413075
<b>MAP 2D Map AC</b>	0.6565	0.7776	0.8031	0.5711	0.702075
<b>FBP 2D seg AC</b>	0.1573	0.4129	0.1559	0.1389	0.21625
<b>FBP 3D no AC</b>	0.1072	0.1545	0.1070	0.1265	0.1238

Table 7: AUC values of the LROC study for each single observer, as well as the average AUC values, over all reconstruction modalities.

Probability of loc. Or Loc. accuracy	<b>B</b>	<b>E</b>	<b>P</b>	<b>J</b>	<b>Average</b>
<b>FBP 2D NoAC</b>	0.5078 (0.0663)	0.5361 (0.0650)	0.5239 (0.0660)	0.2504 (0.0601)	0.45455 (0.06435)
<b>MAP 2D Map AC</b>	0.7061 (0.0603)	0.7776 (0.0452)	0.8458 (0.0447)	0.6107 (0.0664)	0.73505 (0.05415)
<b>FBP 2D seg AC</b>	0.1942 (0.0544)	0.4129 (0.0551)	0.1914 (0.0539)	0.1689 (0.0516)	0.24185 (0.05375)
<b>FBP 3D no AC</b>	0.1192 (0.0455)	0.1545 (0.0497)	0.1268 (0.0462)	0.1557 (0.0499)	0.13905 (0.04783)

Table 8: Localization accuracy (or probability of localization) along with SE in brackets.

<i>p</i> -values	<b>B</b>	<b>E</b>	<b>P</b>	<b>J</b>	<b>Average</b>
<b>This study</b>	0.0537	0.0375	0.0072	0.0095	0.0010
<b>[Far99]</b>	0.6416	0.1661	0.2323	0.3312	0.3381

Table 9: *p*-values relative to the comparison of the MAP modality with 2D FBP without AC.

The results of the LROC study are consistent with those of the ROC one discussed above: most importantly, once again MAP is shown to perform better than any FBP variant. However, in contrast to the ROC analysis and the LROC one described in [Far99] and [Far98], here the improvement turns out to be statistically significant<sup>22</sup>. Thus, one can easily infer that the difference in performance between FBP trained and non trained observers is uniquely enclosed in the “localization” aspect.

It is fundamental to investigate what exactly this difference is about and, to do so, a closer look is necessary to the way the ROC and respectively the LROC programs deal with the readers’ responses.

The ROC program developed by Metz et al. [Met84] is based on a binormal curve-fitting routine embedded in a coupled design, that computes two ROC curves for the two modalities being compared. Each of the ROC curve computed represents the fraction of TP answers plotted against the FP fraction of each reconstruction mode, and every curve is thus independent on the number and type of modalities considered in the whole study.

---

<sup>22</sup> *P*-values were only computed in the case of MAP confronted with 2D FBP without AC, because this is the most representative case.

In contrast, the LROC program developed by Swensson [Swe96] computes the (L)ROC values for a single case at the time and the comparisons between different modalities are done in a second phase. Moreover, here the (L)ROC curves represent the fraction of TP answers with correct location relative to a given modality, against the global FP fraction, i.e. the fraction of FP answers relative to all reconstruction modalities, rather than only to the one to which the TP values are referred. The reason for this is that in an LROC study the major focus is the localization aspect, rather than the pure detection; emphasis is given to sensitivity (i.e. correctly locating a lesion on TP images), while conclusions can hardly be drawn with reference to specificity (i.e. discarding the suspicion of a lesion, when no lesion is present in the image).

In summary, results of the LROC study can be interpreted as follows:

*Lesions are easily localized on TP MAP reconstructions, whereas wrong locations are often indicated on TP FBP images.*

This statement is further confirmed by the values of Table 8, relative to the probability of correct localization: while this value is quite high for MAP reconstructions, pointing out the reliability of this method in terms of sensitivity, the localization accuracy of all other methods is almost not acceptable.

However, nothing can be inferred about the performance of the observers on TN images, i.e. the study does not give any feedback concerning the specificity of the test over the different modalities, because the observers' responses relative to TN images are pooled together over all four reconstruction methods. The only way to gain further insight into this aspect is by comparing the ROC results discussed in the previous section with the LROC results of this section, or, alternatively, with ROC values computed in a similar way the LROC ones are obtained, namely, by pooling together the readers' responses relative to TN images: this kind of ROC values

were in fact also provided by the same package developed by Swensson [Swe96] and they are summarized in Table 10.

The big difference among the AUC values of Table 10 as well as the statistical significance established by the LROC study are not observable in the ROC study discussed in the previous section. This means that the improvement of the MAP method in terms of sensitivity pointed out by the LROC study is not sufficient to result in an overall improved detection performance, as shown by the ROC analysis; in other words, the MAP algorithm lacks in specificity and this weakness is serious enough to undermine its overall performance, reducing it to the same level of other, more simplistic algorithms. These conclusions had already been perceived by the first pre-evaluation of the observer results, described at the beginning of this section.

ROC (AUC)	B	E	P	J	Average
<b>FBP 2D NoAC</b>	0.7188 (0.0312)	0.7283 (0.0310)	0.7282 (0.0313)	0.6110 (0.0276)	0.696575 (0.030275)
<b>MAP 2D Map AC</b>	0.8283 (0.0304)	0.8424 (0.0262)	0.9016 (0.0244)	0.7855 (0.0326)	0.83945 (0.0284)
<b>FBP 2D seg AC</b>	0.5786 (0.0233)	0.6320 (0.0237)	0.5780 (0.0231)	0.5695 (0.0225)	0.589525 (0.02315)
<b>FBP 3D no AC</b>	0.5536 (0.0208)	0.5596 (0.0205)	0.5535 (0.0202)	0.5633 (0.0215)	0.5575 (0.02075)

Table 10: AUC values of an ROC study computed by the package developed by Swensson [Swe96]: the observers' responses relative to the TN images are pooled together over all different reconstruction modalities. Also reported are the respective SEs.

## **Conclusion**

The study presented has shown that the MAP algorithm can obtain better results at the task of lesion detection, than the more popular and widely used FBP method. However, the reader bias that we previously suspected in the Farquhar et al. study was probably not a large factor. Rather, it appears that MAP features very good sensitivity qualities with respect to the linear algorithm, but it does not present as promising performances in terms of specificity. This weakness degrades the overall accuracy of the method and it becomes doubtful whether the improvement of the iterative approach pays off the computational burden required. The weakness in specificity clearly points to the direction to take to further optimizing the algorithm in order to have it represent a preferable substitute of the FBP method in clinical settings.

Different variants of the FBP algorithm were considered and, among all comparisons, the 2D version was shown to outperform the 3D: it was conjectured that the advantages of a 3D acquisition can not compensate for other limitations, such as the absence of scatter corrections in the 3D implementation of the reconstruction models.

Nothing similar was proven for MAP, since this method was considered in the purest form, namely, 2D with MAP attenuation correction, and no other variant was examined. A 3D version is worth being studied and scatter correction can also be implemented to it, so that the advantages of a 3D acquisition can be directly addressed and evaluated. Besides, a lower injection dose was used in the 3D case and this might also explain its relatively poor performance. However, various comparative studies of 2D versus 3D PET have shown 3D to be at least competitive with 2D when the optimal dose is used in both studies.

Finally, it is important to note that these results can not be generalized to absolute conclusions, since there were several shortcomings and the validity of the exam is restricted to a specific context: limitations are related to the parameters of the scanner, the acquisition protocols, the type and location of lesion, the particular anatomy considered, the design of the reconstruction models, the visualization and evaluation procedure, and complex combinations of all these factors. For instance, for the detection of lesions in the liver, attenuation correction might be almost unavoidable, and 3D acquisition can be preferable for imaging anatomies where the scatter medium is diminished, such as the head and neck. Iterative reconstruction provides better results when imaging organs for which FBP shows streak artifacts, such as prostate, colon, and other organs adjacent to the bladder. Finally, more complex visualization options, such as the availability of transaxial and sagittal slices, in combination with the coronal ones, can definitely facilitate the overall evaluation procedure.

## Conclusion

In this thesis we have addressed two main issues of tomography: the reconstruction of images from the raw data acquired by the medical device and the quality evaluation of the reconstructions. In particular, we have developed a projection model for a specific SPECT device and we have shown how this can be coupled with several inversion algorithms to obtain quite efficient reconstruction models. Subsequently, we have presented a task oriented approach to assess the quality of the reconstructions, involving both human and computer observers. The studies performed and the results obtained point out the advantages as well as the limits of our analysis and suggest the direction to follow in future work.

Instead of further discussing the possible extensions of this project, I would rather like to take a look back in time: in the next page an article is included<sup>23</sup> that was published in 1896 in the January issue of “Magazine for the Families” and found again in my grandma’s loft in 1989. Those two brief columns describe the basic idea underlying the concept of Medical Imaging and somehow already anticipate the now well-known scientific progress that has been made in this field over the past century. In some way, this article provides confidence and the basic support to believe that research is constantly and fast advancing towards distant and sometimes apparently unreachable goals: the work I have presented in this dissertation is part of this scientific progress and it, hopefully, represents a contribution, although only infinitesimal, to the general framework of Medical Imaging.

---

<sup>23</sup> A translation into English follows.



Lire 5 l'anno - Cent 10 il numero. - Volume XXXIII. - N. 4. - 26 Gennaio 1896. -

FRATELLI TREVES, Editori, Milano.

## *Novità della scienza e dell'industria.*

**La fotografia nell'interno dei corpi.** — In questi giorni è stata annunciata una scoperta delle più sorprendenti fatta dal professore Roentzen dell'Università di Würzburg sul Meno.

Egli stava facendo delle esperienze fotografiche servendosi come fonte luminosa di un tubo di vetro nel quale era stato fatto precedentemente il vuoto e per mezzo di una corrente d'induzione aveva prodotto la luce detta di Crookes. Egli si accorse allora di un fatto meraviglioso: che cioè l'azione di questa sorgente luminosa poteva esercitarsi liberamente attraverso il legno, ma non attraverso ai metalli. Così egli poté fotografare alcuni oggetti di rame, che stavano in una cassetta di legno, perfettamente chiusa, dalla quale appariscono nella fotografia anche i chiodi, mentre non si vede nulla della parte lignea.

Allo stesso modo — ed è ciò sorprendente ancora — la carne è per così dire diafana a quei raggi luminosi, mentre sono opache le ossa: tanto che il prof. Roentzen poté ottenere riprodotta in fotografia lo scheletro della mano, con gli anelli che ne ornavano le dita senza nessuna traccia del contorno carnoso.

Questa scoperta sembra quindi destinata ad apportare una rivoluzione nei dati della scienza e delle esperienze che si riferiscono alla propagazione della luce; ma avrà anche una pratica applicazione come grande aiuto della chirurgia. Con questo processo, sarà agevole riconoscere la natura, l'importanza delle fratture, le ferite delle armi, specie di quelle da sparo. Si conosceranno i tumori. Nell'estrazione delle palle soprattutto, il nuovo metodo di investigazione risparmierà al ferito il metodo attuale così tormentoso, del sondaggio, operato spesso a caso.

## *News on science and industry*<sup>24</sup>

### **Photography inside bodies.**

In these past days, one of the most stunning discovery has been announced, made by Professor Roentzer at the University of Würzburg am Main.

He was performing some photographic experiments using a vacuum filled glass tube as lighting source and an induced current to produce the so called Creckes light, when he realized a wonderful effect: this lightning source would freely act through wood but not through metals. In this way, he was able to photograph some copper items located inside a wooden box that was perfectly sealed and of which one can even see the nails in the photography, but not the wooden part.

In the same way – and this is still also astonishing – flesh is, so to say, diaphanous to those light rays, while bones are opaque to them: to the point that Professor Roentzer was able to obtain a photographic reproduction of the skeleton of his own hand, along with the rings worn on his fingers, but without any trace of the flesh contour.

Therefore, this discovery seems to be destined to bring a revolution in scientific data and in all experiences related to light propagation; but it will also have a practical application as a significant support to surgery. Through this process, it will be easy to Figure out the nature and the importance of fractures, the wounds caused by weapons, especially shooting weapons. Tumors will be known. Most of all, for the extraction of bullets, the new investigation method will avoid the wounded to undergo the current, such painful method of the probe, that is often performed in a random way.

---

<sup>24</sup> This is a translation of the article reported above, that appeared on the January 26<sup>th</sup>, 1896 issue of the *Illustrazione Popolare, Giornale per le famiglie*, Vol.33, No.4, Fratelli Treves Editori, Milano, Italy.

# Appendix

## a. Time complexity and multithreaded computation

Computational complexity is a major issue in the design of reconstruction algorithms.

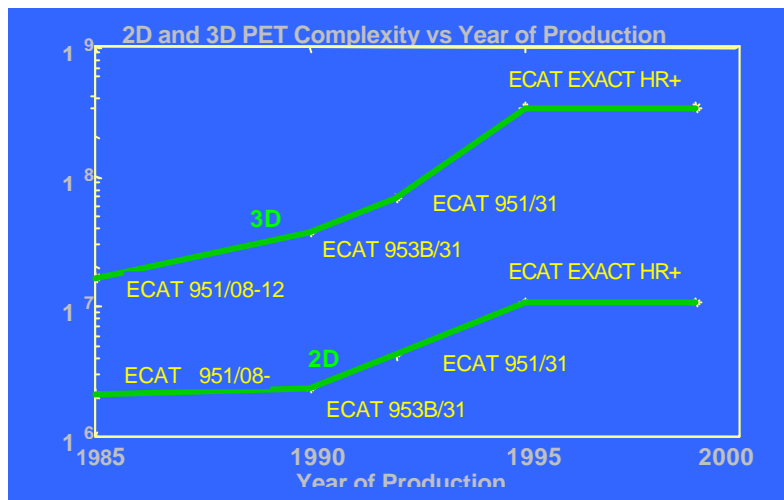


Figure 53: The complexity of 2D and 3D PET devices has an exponential growth.

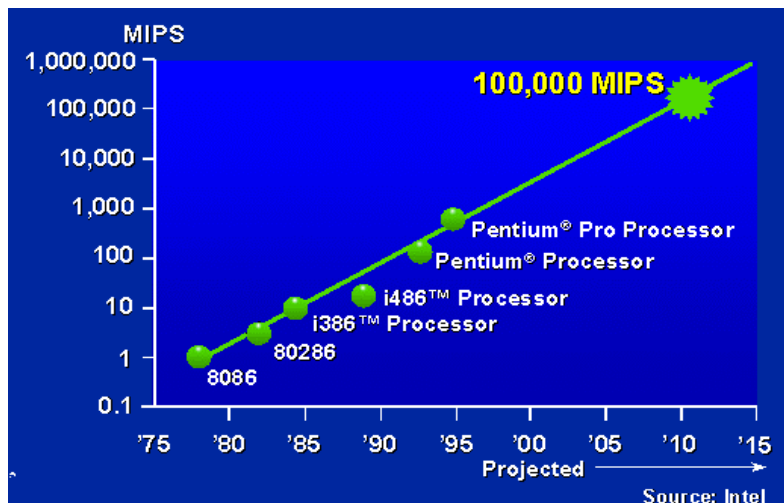


Figure 54: The power of PC processors in terms of MIPS has a linear growth.

If we denote by  $L$  the number of rings of the tomograph,  $M$  the number of detectors per ring and  $N \times N$  the dimension of the reconstructed planes, then the complexity of PET devices is given by  $M^2 \times L \times N$  for a 2D scanner and  $M^2 \times L^2 \times N$  for a 3D one.

As one can see from the plots reported in Figure 53 in semi-logarithmic scale, these values have shown an over-exponential growth over the past decades, resulting from the improvements and advancements made in the technology of PET instrumentation. However, the PC processor performance has “only” shown exponential growth (Figure 54). For this reason, methods to reduce the total computational cost must be sought elsewhere, in particular in the design of the reconstruction algorithms.

In the case of iterative reconstruction schemes, time complexity is a function of the number of iterations times the cost to perform each single iteration. The most time consuming steps at each iteration are forward and back projections, whose complexity depends on the properties of the specific tomographic device and on the acquisition modality. Considering the definitions of PET complexity given above it is easy to show that the total reconstruction cost is:

$$M^2 \times L \times N \times \text{number of iterations in the case of 2D PET}$$

$$M^2 \times L^2 \times N \times \text{number of iterations in the case of 3D PET}$$

Several approaches can be taken in order to reduce the time complexity.

First of all one can optimize the iterative scheme in order to reduce the convergence rate. In the case of CG, for instance, this can be achieved by incorporating appropriate preconditioners as mentioned in section 0. In the case of EM faster convergence is obtained by redesigning the method using the ordered subset approach (section 0).

One should try to optimize the code exploiting the properties of the data (symmetries, sparse matrices, data compression etc.), of the hardware resources (use of cache, registers, avoid disk swapping, etc.), and of the programming language (available additional libraries, optimization options, etc.).

In the implementation of our MAP scheme, we have addressed this problem by multithreading the code (using appropriate C libraries), i.e. by defining separate “threads” that can run in parallel. On a multiprocessor machine the threads can run simultaneously on different processors – typically, the number of threads is chosen to be equal to the number of available processors.

	<b>HR+</b>	<b>MicroPET</b>
<b>Field of View (cm)</b>	58 Ø, 15.5 axial	11.2 Ø, 1.8 axial
<b>Image size</b>	128 x 128 x 32	128 x 128 x 24
<b>Total LORS</b>	$9.9 \times 10^6$	$7.7 \times 10^5$
<b>Full P size</b>	$5 \times 10^{12}$	$2.8 \times 10^{11}$
<b>P<sub>geom</sub> size</b>	42 MB	16 MB
<b>P<sub>blur</sub> size</b>	0.5 MB	0.2 MB
<b>1 iteration, 2D</b>	1:20 (0:36) min	/
<b>1 iteration, 3D</b>	16:00 (4:45) min	2:30 (1:00) min
<b>20 iterations, 2D</b>	6:15 (1:50) min	/
<b>20 iterations, 3D</b>	161 (50) min	22:00 (7:50) min

Table 11: Space complexity of HR+ and MicroPET scanners and run times of 2D and 3D reconstruction, 1 and 20 iterations. Run times are referred to a 400 MHz Pentium II and, in brackets, to a \$20k Dell Poweredge Server with four 400 MHz Xeon Pentium II processors and 1GB of RAM, running a multithreaded code.

As mentioned above, the dominant cost of the reconstruction algorithm is due to forward and backprojection, which involve the product of the large system matrix with an image or, respectively, sinogram vector. This operation can be multithreaded by subdividing the rows or columns of the matrix across different threads. The final result is obtained by combining the output of each thread.

Our studies were performed on the whole body ECAT EXACT HR+ and the small animal microPET scanner and the programs were run on a Windows NT, 400 MHz Pentium II equipped with 1GB memory. Table 11 summarizes the main factors affecting space complexity for both PET scanners and the respective run times of both 2D and 3D MAP reconstructions. The times are reported for a single thread execution and, in brackets, for a multithreaded version of the same program, running on a four processor, 400 MHz Xeon Pentium II: in this latter modality we were able to achieve a speedup over the singlethreaded program by factors in the range of 3.5-3.7 in total computing time. Similar results were also obtained on a Unix (Solaris) platform.

## **b. GUI**

To facilitate the use of the MAP reconstruction program to non experts we have developed a Graphical User Interface from which the user can specify all parameter inputs for the reconstruction of a single image. The interface, developed for the Windows platform, is shown in Figure 55. The parameters are collected into five main groups according to their type: those related to the device (our code currently works on ECAT HR+ and MicroPET data) and acquisition (2D vs 3D modality), the reconstruction algorithm with the fundamental entry being the value of the smoothing parameter, the particular settings for the execution of the program (multithreaded vs. singlethreaded, number of saving rate of the intermediate results computed at each iteration, etc.) and the filenames. Beside the output file name, all other names are related to data that has to be read as input by the program. These include optional files as attenuation, normalization, and scatter, as well as necessary ones, namely, projection matrix, blurring kernels and, of course, the sinogram with the scanned data. Our current implementation of the program is based on the Conjugate Gradient algorithm, but it could easily be extended to other methods such as EM or OSEM.

The configuration, i.e. the set of parameter values as specified into the GUI, can be saved to disk for future use.

By clicking on the <RUN> botton, the GUI writes, and subsequently passes control to a script file that defines all parameters at the OS environment level in order that they can be passed over to DOS executables as standard command line input parameters; the script file also handles the calls of some utilities that convert the data from CTI format into raw binary float format and, finally, calls the reconstruction program.

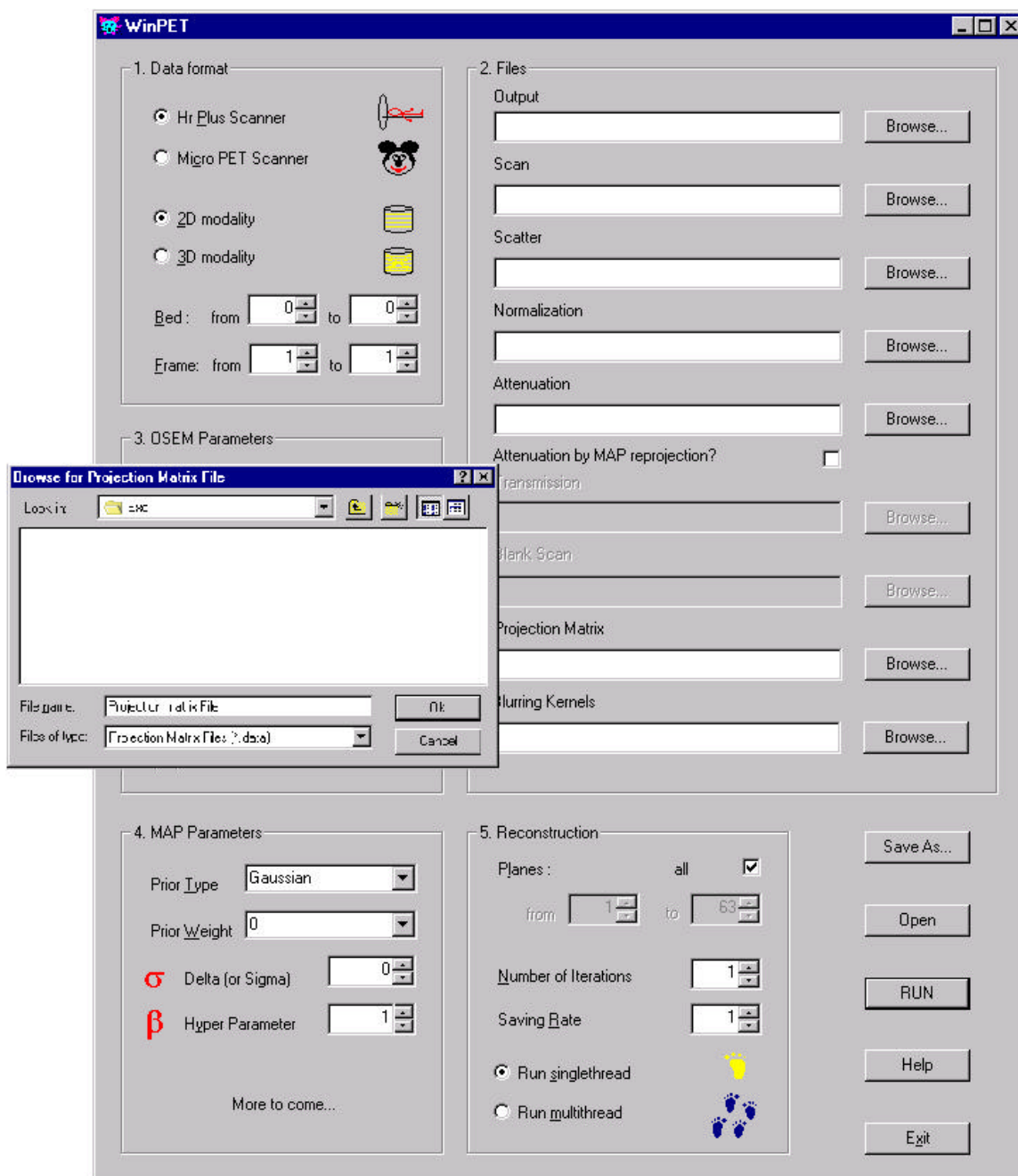


Figure 55: The Graphical User Interface to the MAP reconstruction program, developed for a Windows platform with Microsoft Visual C++.

## References

[Abb95] C.K.Abbey, H.H.Barrett, *Linear Iterative Reconstruction Algorithms: Study of Observer Performance*, Proceedings to the 14<sup>th</sup> International Conference on Information Processing of Medical Imaging, pp. 65-76, Kluwer Academic Publishers, 1995

[Abb96] C.K.Abbey, H.H.Barrett, D.W.Wilson, *Observer Signal-to-Noise Ratios for the ML-EM Algorithm*, SPIE, Vol. 2712, 1996

[Bai94] D.L.Bailey, F.Zito, M.C.Gilardi, A.R.Savi, F.Fazio, T.Jones, *Performance Comparison of a State-of-the-art Neuro-SPECT Scanner and a Dedicated Neuro-PET Scanner*, European Journal of Nuclear Medicine, Vol. 21, pp. 381-387, 1994

[Bal98] D.Baldini, P.Calvini, A.R.Formiconi, *Image Reconstruction with Conjugate Gradient Algorithm and Compensation of the Variable System Response for an Annular SPECT System*, Physica Medica, Vol. 14, pp. 159-173, 1998

[Bar81] H.H.Barrett, W.Swindell, *Radiological Imaging*, Vol. 1, Academic Press, 1981

[Bar90] H.H.Barrett, J.Yao, J.P.Rolland, K.J.Myers, *Model Observers for Assessment of Image Quality*, Proceedings of the National Academy of Sciences, pp. 9758-9765, 1990

[Bar90b] H.H.Barrett, *Objective Assessment of Image Quality: Effects of Quantum Noise and Object Variability*, Journal of the Optical Society of America, Vol. A7, pp. 1266-1278, 1990

[Bar92] H.H.Barrett, T.Gooley, K.Girodias, J.Rolland, T.White, J.Yao, *Linear Discriminants and Image Quality*, Image and Vision Computing, Vol. 10, pp. 451-460, 1992

[Brac67] R.N.Bracewell, A.C.Riddle, *Inversion of Fan-beam Scans in Radio Astronomy*, Astrophysics Journal, Vol. 150, p.427 1967

[Ber89] M.Bertero, *Linear Inverse and Ill-Posed Problems (Advanced Electronics and Electron Physics, vol 75)*, ed. P.W.Hawkes (New York: Academic), pp. 1-120, 1989

[Ber95] M.Bertero, P.Boccacci, F.Maggio, *Regularization Methods in Image Restoration: an Application to HST Images*, International Journal of Image Systems and Technology, Vol. 6, No. 4 pp. 376-386, 1995

[Ber98] M. Bertero, P.Boccacci, *Introduction to Inverse Problems in Imaging*, Bristol: IOP Publishing, 1998

[Bia59] H.Bialy, *Iterative Behandlung Linearer Funktionalgleichungen*, Arch.Ration.Mech.Anal., Vol. 4, pp. 166-176, 1959

[Boc99] P.Boccacci, P.Bonetto, P.Calvini, A.R.Formiconi, *A Simple Model for the Efficient Correction of Collimator Blur in 3D SPECT Imaging*, Inverse Problems, Vol. 15, pp. 907-930, 1999

[Bon00] P.Bonetto, J.Qi, R.M.Leahy, *Covariance Approximation for Fast and Accurate Computation of Channelized Hotelling Observer Statistics*, IEEE Transactions on Nuclear Science, Vol. 47, No. 4, pp. 1567-1572, August 2000

[Bou96] C.A.Bouman, K.Sauer, *A Unified Approach to Statistical Tomography Using Coordinate Descent Optimization*, IEEE Transactions on Image Processing, Vol. 5, No. 3, March 1996

[Bro96] J.Browne, A.R.De Pierro, *A Row-Action Alternative to the EM Algorithm for Maximizing Likelihoods in Emission Tomography*, IEEE Transactions on Medical Imaging, Vol. 15, pp. 687-699, 1996

[Bud77] T.F.Budinger, S.E.Derenzo, G.T.Gullberg, W.L.Greenberg, R.H.Huesman, *Emission Computer Assisted Tomography with Single-Photon and Positron Annihilation Photon emitters*, Journal of Computed Assisted Tomography, Vol. 1, pp. 131-145, 1977

[Bur77] A.E.Burgess, *Comparison of Receiver Operating Characteristic and Forced Choice Observer Performance Measurement Methods*, Medical Physics, Vol. 22, pp. 643-655, 1995

[Bur95a] A.E.Burgess, *Comparison of Receiver Operating Characteristic and Forced Choice Observer Performance Measurement Methods*, Medical Physics, Vol. 22, pp. 643-655, 1995

[Bur95] A.E.Burgess, *Experimental Evaluation of Observer Models for Detection of Signals in Statistically Defined Backgrounds*, Information Processing in Medical Imaging, Kluwer Academic Publishers, pp. 89-100, 1995

[Byr97] C.Byrne, *Convergent Block-Iterative Algorithms for Image Reconstruction from Inconsistent Data*, IEEE Transactions on Image Processing, Vol. 6, pp. 1296-1304, 1997

[Car97] A.Cartabellotta, G.Montalto, A.Notarbartolo, Gruppo Italiano per Medicina Basata sulle Evidenze (GIMBE), *La Medicina Basata sulle Evidenze nella Valutazione dei Tests Diagnostici (Evidence-based Medicine in Evaluating Diagnostic Tests)*, Medic, Vol. 5, pp. 113-119, 1997

[Cha95] M.Chan, G.T.Herman, E.Levitan, *Bayesian Image Reconstruction Using a High-Order Interacting MRF Model*, Proceedings of the 8<sup>th</sup> International Conference on Image Analysis and Processing, pp. 609-614, San Remo, Italy, Springer, 1995

[Cha97] M.T.Chan, R.M.Leahy, E.Ü.Mumcuoglu, S.R.Cherry, J.Czernin, A.Chatziioannou, *Comparing Lesion Detection Performance for PET Image Reconstruction Algorithms: a Case Study*, IEEE Transactions on Nuclear Science, Vol. 44, No. 4, pp. 1558-1563, August 1997

[Cha99] A.Chatziioannou, A.Morre, A.Annala, K.Nguyen, R.Leahy, S.Cherry, *Comparison of 3D MAP and Filtered Back-Projection Algorithms for High Resolution Animal Imaging with MicroPET*, Proceedings of the Meeting on Fully 3D Image Reconstruction, pp. 185-188, June 1999

[Cha00] A.Chatziioannou, A.Morre, A.Annala, K.Nguyen, R.Leahy, S.Cherry, *Comparison of 3D MAP and Filtered Back-Projection Algorithms for High Resolution Animal Imaging with MicroPET*, IEEE Transactions on Medical Imaging, May 2000

[Che91] C.Chen, S.Lee, Z.Cho, *Parallelization of the EM Algorithm for 3D PET Image Reconstruction*, IEEE Transactions on Medical Imaging, Vol. 10, pp. 513-522, 1991

[Cli93] N.H.Clinthorne, T.S.Pan, P.C.Chiao, W L.Rogers, J.A. Stamos, *Preconditioning Methods for Improved Convergence Rates in Iterative Reconstruction*, IEEE Transactions on Medical Imaging, Vol. 12, No. 1, pp. 78-83, March, 1993

[Coa91] K.J.Coakley, *A Cross-Validation Procedure for Stopping the EM Algorithm and Deconvolution of Neutron Depth Profiling Spectra*, IEEE Transactions on Nuclear Science, Vol. 38, No. 1, pp. 9-15, 1991

[Das74] S.Das Gupta, M.D.Perlman, *Power of the Noncentral F-Test: Effect of Additional Variates on Hotelling's  $T^2$ -Test*, Journal of the American Statistical Association, Vol. 69, pp. 174-180, 1974

[Dau92] M.E.Daube-Witherspoon, R.E.Carson, Y.C.Yan, T.K.Yap, *Scatter Correction in ML Reconstruction of PET Data*, Proceedings of IEEE Nuclear Science and Medical Imaging Conference, Orlando, Florida, pp. 945-947, 1992

[Dem77] A.Dempster, N.Laird, D.Rubin, *Maximum Likelihood from Incomplete Data via the EM Algorithm*, Journal of Royal Statistical Society, Series B, Vol. 39, No. 1, pp. 1-38, 1977

[Dew93] N.A.Dewan, N.C.Gupta, L.S.Redepenning, J.J.Phalen, M.P.Frick, *Diagnostic Efficacy of PET-FDG Imaging in Solitary Pulmonary Nodules: Potential Role in Evaluation and Management*, Chest, Vol. 104, pp. 997-1002, 1993

[Duh95] F.G.Duhaylongsod, V.J.Lowe, E.J.Patz, A.L.Vaughn, R.E.Coleman, W.G.Wolfe, *Detection of Primary and Recurrent Lung Cancer by Means of F-18 Fluorodeoxyglucose Positron Emission Tomography (FDG PET)*, Journal of Thoracic and Cardiovascular Surgery, Vol. 110, pp. 130-139, 1995

[Far98] T.H.Farquhar, *Improving Lesion Detection in Whole Body PET*, Ph.D.Dissertation, University of California Los Angeles, 1998

[Far99] T.H.Farquhar, *ROC and Localization ROC Analyses of Lesion Detection in Whole-Body FDG PET: Effects of Acquisition Mode, Attenuation Correction and Reconstruction Algorithm*, Journal of Nuclear Medicine, Vol. 40, No. 12, December 1999

[Fes94] J.A.Fessler, *Penalized Weighted Least Squares Image Reconstruction for PET*, IEEE Transactions on Medical Imaging, Vol. 13, pp. 290-300, 1994

[Fes96a] J.A.Fessler, *Mean and Variance of Implicitly Defined Biased Estimators (Such as Penalized Maximum Likelihood): Applications to Tomography*, IEEE Transactions on Image Processing, Vol. 5, No. 3, March 1996

[Fes96b] J.A.Fessler, W.L.Rogers, *Spatial Resolution Properties of Penalized-Likelihood Image Reconstruction: Space-Invariant Tomographs*, IEEE Transactions on Image Processing, Vol. 5, No. 9, September 1996

[Fes97] J.A.Fessler, E.P.Ficaro, N.H.Clinthorne, K.Lange, *Grouped-coordinate Ascent Algorithms for Penalized-Likelihood Transmission Image Reconstruction*, IEEE Transactions on Medical Imaging, Vol. 16, No. 2, pp. 166-175, 1997

[Fie87] R.D.Fiete, H.H.Barrett, W.E.Smith, K.J.Myers, *The Hotelling Trace Criterion and its Correlation with the Human Observer Performance*, Journal of the Optical Society of America Vol. A4, pp. 945-953, 1987

[Fis36] R.Fisher, *The use of Multiple Measurements in Taxonomic Problems*, Annual Eugenics, Vol. 7, pp. 179-188, 1936.

[For89] A.R.Formiconi, A.Pupi, A.Passerì, *Compensation of Spatial System Response in SPECT with Conjugate Gradient Reconstruction Technique*, Physics in Medicine and Biology, Vol. 34, pp. 69-84, 1977

[For97] A.R.Formiconi, A.Passerì, M.R.Guelfi, M.Masoni, A.Pupi, U.Meldolesi, P.Malfetti, L.Calori, A.Guidazzoli, *World Wide Web Interface for Advanced SPECT Reconstruction Algorithms Implemented on a Remote Massively Parallel Computer*, International Journal of Medical Informatics, Vol. 47, pp. 125-138, 1997

[Fuk89] K.Fukunaga, R.R.Hayes, *Effects of Sample Size in Classifier Design*, IEEE Transactions on Pattern Analysis and Machine Intelligence, Vol. 11, pp. 873-885, 1989

[Gem84] S.Geman, D.Geman, *Stochastic Relaxation, Gibbs Distributions, and the Bayesian Restoration of Images*, IEEE Transactions on Pattern Analysis and Machine Intelligence, Vol. 6, No. 6, pp. 721-741, 1984

[Gem85] S.Geman, D.E.McClure, *Bayesian Image Analysis: An Application to Single Photon Emission Tomography*, Proceedings of the Statistical Computing Section of the American Statistical Association, pp. 12-18, 1985

[Gin93] G.Gindi, M.Lee, A.Rangarajan, I.G.Zubal, *Bayesian Reconstruction of Functional Images Using Anatomical Information as Priors*, IEEE Transactions on Medical Imaging, Vol. 12, No. 4, pp. 670-680, 1993

[Gre81] U.Grenander, *Abstract Inference*, John Wiley and Sons, New York, 1981

[Gre90] P.Green, *Bayesian Reconstructions from Emission Tomography Data Using a Modified EM Algorithm*, IEEE Transactions on Medical Imaging, Vol. 9, No. 1, pp. 84-93, 1990

[Gua94] H.Guan, R.Gordon, *A Projection Access Order for Speedy Convergence of ART (Algebraic Reconstruction Technique): a Multilevel Scheme for Computed Tomography*, Physics in Medicine and Biology, Vol. 39, pp. 2005-2022

[Gul96] G.T.Gullberg, YL.Hsieh, G.T.Zeng, *An SVD Algorithm Using a Natural Pixel Representation of the Attenuated Radon Transform*, IEEE Transactions on Nuclear Science, Vol. 43, No. 1, pp. 295-303, Feb. 1996

[Gup96] N.C.Gupta, J.Maloof, E.Gunel, *Probability of Malignancy in Solitary Pulmonary Nodules Using Fluorine-18-FDG and PET*, Journal of Nuclear Medicine, Vol. 37, pp. 943-948, 1996

[Hag97] R.C.Hagberg, G.M.Segall, P.Stark, T.A.Burdon, M.F.Pompili. *Characterization of Pulmonary Nodules and Mediastinal Staging of Bronchogenic Carcinoma with F-18 Fluorodeoxyglucose Positron Emission Tomography*, European Journal of Cardio Thoracic Surgery, Vol. 12, pp. 92-97, 1997

[Han95] M.Hanke, *Conjugate Gradient Type Methods for Ill-Posed Problems*, 1<sup>st</sup> edition (London: Longman) (copublished in the USA with New York: Wiley), 1995

[Her71] G.T.Herman, A.V.Lakshminarayanan, A.Naparstek, *Convolution Reconstruction Techniques for Divergent Beams*, Computers in Biology and Medicine, Vol. 6, p.259, 1971

[Her77] G.T.Herman, A.Naparstek, *Fast Image Reconstruction for Rapidly Collected Data*, SIAM Journal on Applied Mathematics, Vol. 33, pp. 511-533, 1977

[Her79] G.T.Herman, *Image Reconstruction from Projections – Implementation and applications*, Springer –Verlag, 1979

[Her80] G.T.Herman, *Image Reconstruction from Projections – The Fundamentals of Computerized Tomography*, Academic Press, 1980

[Her91] G.T.Herman, D.Odhner, *Performance Evaluation of an Iterative Image Reconstruction Algorithm for Positron Emission Tomography*, IEEE Transactions on Medical Imaging, Vol. 10, No. 3, September 1991

[Her93] G.T.Herman, L.Meyer, *Algebraic Reconstruction Techniques can be Made Computationally Efficient*, IEEE Transactions on Medical Imaging, Vol. 12, pp. 600-609, 1993

[Hes52] M.R.Hestens, E.Stiefel, *Methods of Conjugate Gradients for Solving Linear Systems*, Journal of Research of the National Bureau of Standards, Vol. 49, No. 6, pp. 409-436, 1952

[Heu94] G.Heuser, I.Mena, C.Thomas, F.Alamos, *Cerebral Blood Flow in Patients Exposed to Neurotoxic Chemicals*, Journal of Nuclear Medicine, Vol. 35(suppl.), p.210, 1994

[Hof90] E.J.Hoffman, P.D.Cutler, W.M.Digby, J.C.Mazziotta, *3D Phantom to Simulate Cerebral Blood Flow and Metabolic Images for PET*, IEEE Transactions on Nuclear Science, Vol. 37, pp. 616-620, 1990

[Hol90] B.L.Holman, P.A.Carvalho, R.E.Zimmerman, K.A.Johnson, S.S.Tumeh, A.P.Smith, S.Genna, *Brain Perfusion SPECT Using an Annular Single Crystal Camera: Initial Clinical Experience*, Journal of Nuclear Medicine, Vol. 31, pp. 1456-1461, 1990

[Hol92] B.L.Holman, B.Garada, K.A.Johnson, J.Mendelson, E.Hallgring, S.K.Teoh, J.L.Worth, B.A.Navia *A Comparison of Brain Perfusion SPECT in Cocaine Abuse and AIDS Dementia Complex*, Journal of Nuclear Medicine, Vol. 33, pp. 1312-1315, July 1992

[Hot31] H.Hotelling, *The Generalization of Student's Ratio*, The Annals of Mathematical Statistics, Vol. 2, pp. 360-378, 1931

[Hsu98] C.H.Hsu, J.Qi, *A Study of Lesion Contrast Recovery for Statistical PET Image Reconstruction with Accurate System Model*, Proceedings SPIE Medical Imaging Conference, San Diego, February, 1998

[Hsu98t] C.H.Hsu, *Bayesian Image Reconstruction Techniques for Positron Emission Tomography: Theory and Applications*, Ph.D. Thesis, University of Southern California, August, 1998

[Hud92] H.M.Hudson, B.F.Hutton, R.S.Larkin, *Accelerated EM Reconstruction using Ordered Subsets*, Journal of Nuclear Medicine, Vol. 33, p.960, 1992

[Hud94] H.M.Hudson, R.S.Larkin, *Accelerated EM Reconstruction using Ordered Subsets of Projection Data*, IEEE Transactions on Medical Imaging, Vol. 13, pp. 601-609, 1994

[Hue77] R.H.Huesman, G.T.Gullberg, W.L.Greenberg, T.F.Budinger, *User's Manual; Donner Algorithms for Reconstruction Tomography*, Lawrence Berkeley Laboratory, University of California, 1977

[Jas84] R.J.Jaszczak, K.L.Greer, C.E.Floyd Jr., C.C.Harris, R.E.Coleman, *Improved SPECT Quantitation Using Compensation for Scattered Photons*, Journal of Nuclear Medicine, Vol. 25, pp. 893-900, 1984

[Joh94] V.Johnson, *A Note on Stopping Rules in EM-ML Reconstructions of ECT Images*, IEEE Transactions on Medical Imaging, Vol. 13, No. 3, pp. 569-571, 1994

[Joh95] C.Johnson, Y.Yan, R.Carson, R.Martino, M.Daube-Witherspoon, *A System for the 3D Reconstruction of Retracted-Septa PET Data Using the EM Algorithm*, IEEE Transactions on Nuclear Science, Vol. 42, No. 4, pp. 1223-1227, 1995

[Kak88] A.C.Kak, M.Slaney, *Principles of Computerized Tomographic Imaging*, IEEE Press, New York, 1988

[Kau87] L.Kaufman, *Implementing and accelerating the EM Algorithm for Positron Emission Tomography*, IEEE Transactions on Medical Imaging, Vol. 6, No. 1, pp. 37-51, 1987

[Kau93] L.Kaufman, *Maximum Likelihood, Least Squares, and Penalized Least Squares for PET*, IEEE Transactions on Nuclear Science, Vol. 36, pp. 964-996, 1993

[Kin97] M.A.King, D.J.de Vries, E.J.Soares, *Comparison of a Channelized Hotelling and Human Observers for Lesion Detection in Hepatic SPECT Imaging*, SPIE, Vol. 3036, pp. 14-20, 1997

[Kne89] K.Knešaurek, M.A.King, S.J.Glick, B.Penney, *Investigations of Causes of Geometric Distortion in 180° and 360° Angular Sampling in SPECT*, Journal of Nuclear Medicine, Vol. 30, pp. 1666-1675, 1989

[Kni96] S.B.Knight, D.Delbeke, J.R.Stewart, M.P.Sandler, *Evaluation of Pulmonary Lesions with FDG-PET: Comparisons of Findings in Patients with and without a History of Prior Malignancy*, Chest, Vol. 109, pp. 982-988, 1996

[Lan51] L.Landweber, *An Iteration Formula for Fredholm Integral Equations of the First Kind*, American Journal of Mathematics, Vol. 73, pp. 615-624, 1951

[Lan84] K.Lange, R.Carson, *EM Reconstruction Algorithms for Emission and Transmission Tomography*, Journal of Computer Assisted Tomography, Vol. 8, No. 2, pp. 306-316, 1984

[Lan87] K.Lange, M.Bahn, R.Little, *A Theoretical Study of some Maximum Likelihood Algorithms for Emission and Transmission Tomography*, IEEE Transactions on Medical Imaging, Vol. 6, No. 2, pp. 106-114, 1987

[Lea91] R.M.Leahy, X.Yan, *Incorporation of Anatomical MR Data for Improved Functional Imaging with PET*, A.Colchester and D.Hawkes, editors, Information Processing in Medical Imaging, pp. 105-120, Wiley-Liss, 1991

[Lea99] R.M.Leahy, J.Qi, A.Chatziioannou, S.Cherry, *Maximizing Image Resolution in Small Animal PET Systems*, Proceedings International Meeting on High Resolution Imaging in Small Animals, Amsterdam, September 1999

[Lea99CT] R.M.Leahy, R.Clackdoyle, *Computed Tomography*, Image and Video Processing Handbook, ed. Al Bovik, 1999

[Lea00] R.M.Leahy, J.Qi, *Statistical Approaches in Quantitative Positron Emission Tomography*, invited review article, Statistics and Computing, Vol. 10, pp. 147-165, 2000

[Lee95] S.J.Lee, A.Rangarajan, G.Gindi, *Bayesian Image Reconstruction in SPECT Using Higher Order Mechanical Models as Priors*, IEEE Transactions on Medical Imaging, Vol. 14, No. 4, pp. 669-680

[Lew86] R.Lewitt, G.Muehlelehner, *Accelerated Iterative Reconstruction for Positron Emission Tomography Based on the EM Algorithm for Maximum Likelihood Estimation*, IEEE Transactions on Medical Imaging, Vol. 5, No. 1, pp. 16-22, 1986

[Li94] J.Li, R.J.Jaszczak, K.L.Greer, R.E.Coleman, *Implementation of an Accelerated Iterative Algorithm for Cone-beam SPECT*, Physics in Medicine and Biology, Vol. 39, pp. 643-653, 1994

[Lla93] J.Llacer, *Results of a Clinical Receiver Operating Characteristic Study Comparing Filtered Backprojection and Maximum Likelihood Estimator Images in FDG PET Studies*, The Journal of Nuclear Medicine, Vol. 34, No. 7, pp. 1198-1203, 1993

[Lue84] D.G.Luenberger, *Linear and Nonlinear Programming*, 2<sup>nd</sup> edition, Reading, MA: Addison-Wesley, 1984

[Man95] S.H.Manglos, G.M.Gagne, A.Krol, F.D.Thomas, R.Narayanaswami, *Transmission Maximum-Likelihood Reconstruction with Ordered Subset for Cone Beam CT*, *Physics in Medicine and Biology*, Vol. 40, pp. 1225-1241, 1995

[Mat96] Committee on the Mathematics and Physics of Emerging Dynamic Biomedical Imaging, *Mathematics and Physics of Emerging Biomedical Imaging*, National Academy of Sciences, 1996

[Met84] C.E.Metz, P.L.Wang, H.B.Kronman, *A New Approach for Testing the Significance of Differences between ROC Curves Measured from Correlated Data*, In F.Deconinck ed., *Information Processing in Medical Imaging*, The Hague, The Netherlands, Martinus Nijhoff, pp. 432-445, 1984

[Met86] C.E.Metz, *ROC Methodology in Radiologic Imaging*, *Investigative Radiology*, Vol. 21, pp. 720-733, 1986

[Met89] C.E.Metz, *Some Practical Issues of Experimental Design and Data Analysis in Radiological ROC Studies*, *Investigative Radiology*, Vol. 24, pp. 234-245, 1989

[Mum92] E.Ü.Mumcuoglu, R.Leahy, S.R.Cherry, *A Statistical Approach to Transmission Image Reconstruction From Ring Source Calibration Measurements in PET*, *Proceedings of IEEE Nuclear Science and Medical Imaging Conference*, Orlando, Florida, pp. 910-912, 1992

[Mum94] E.Ü.Mumcuoglu, R.Leahy, S.R.Cherry, Z.Zhou, *Fast Gradient-Based Methods for Bayesian Reconstruction of Transmission and Emission PET Images*, IEEE Transactions on Medical Imaging, Vol. 13, No. 4, pp. 687-701, December 1994

[Mum96] E.Ü.Mumcuoglu, R.Leahy, S.R.Cherry, *Bayesian Reconstruction of PET Images: Methodology and Performance Analysis*, Physics in Medicine and Biology, Vol. 41, pp. 1777-1807, 1996

[Mye85] K.J.Myers, H.H.Barrett, M.C.Borgstrom, D.D.Patton, G.W.Seeley, *Effects of Noise Correlation on Detectability of Disk Signals in Medical Imaging*, Journal of the Optical Society of America, Vol. A2, pp. 1752-1759, 1985

[Mye87] K.J.Myers, *Addition of a Channel Mechanism to the Ideal-Observer Model*, Journal of the Optical Society of America, Vol. A4, pp. 2447-2457, 1987

[Oll92] J.Ollinger, G.Johns, M.Burney, *Model-Based Scatter Correction in Three Dimensions*, Proceedings of IEEE Nuclear Science Symposium and Medical Imaging Conference, Vol. 2, pp. 1249-1251, Orlando, Florida, 1992

[Pat95] E.J.Patz, V.J.Lowe, P.C.Goodman, J.Herndon, *Thoracic Nodal Staging with PET Imaging with 18FDG in Patients with Bronchogenic Carcinoma*, Chest, Vol. 108, pp. 1617-21, 1995

[Pet77] T.M.Peters, R.M.Lewitt, *Computed Tomography with Fan-beam Geometry*, Journal of Computed Assisted Tomography, Vol. 1, p.429, 1977

[Pia97] M.Piana, M.Bertero, *Projected Landweber Method and Preconditioning*, Inverse Problems, Vol. 13, pp. 441-463, 1997

[Pol91] D.G.Politte, D.L.Snyder, *Corrections for Accidental Coincidences and Attenuation in Maximum Likelihood Image Reconstruction for Positron Emission Tomography*, IEEE Transactions on Medical Imaging, Vol. 10, No. 1, pp. 82-89, March 1991

[Pre94] W.H.Press, S.A.Teukolsky, W.T.Vetterling, B.P.Flannery, *Numerical Recipes in C/FORTRAN*, Cambridge University Press, 1994

[Qi98a] J.Qi, R.M.Leahy, S.R.Cherry, A.Chatziioannou, T.H.Farquhar, *High-Resolution 3D Bayesian Image Reconstruction using the MicroPET Small-animal Scanner*, Physics in Medicine and Biology, Vol. 43, pp. 1001-1013, 1998

[Qi98b] J.Qi, R.M.Leahy, C.Hsu, T.H.Farquhar, S.R.Cherry, *Fully 3D Bayesian Image Reconstruction for the ECAT EXACT HR+*, IEEE Transactions on Nuclear Science, Vol. 45, No. 3, pp. 1096-1103, June 1998

[Qi98c] J.Qi, *Bayesian Image Estimation for Fully 3D PET*, Ph.D.thesis, University of Southern California, 1998

[Qi99a] J.Qi, R.M.Leahy, *A Theoretical Study of the Contrast Recovery and Variance of MAP Reconstructions From PET Data*, IEEE Transactions on Medical Imaging, Vol. 15, No. 4, pp. 293-305, April 1999

[Qi99b] J.Qi, R.M.Leahy, *A Theoretical Study of the Contrast Recovery and Variance of MAP Reconstructions with Applications to the Selection of Smoothing Parameters*, IEEE Transactions on Medical Imaging, Vol. 18, pp. 293-305, 1999

[Qi99f] J.Qi, R.M.Leahy, *Fast Computation of the Covariance of MAP Reconstructions of PET Images*, SPIE, Vol. 3661, No. 1, pp. 344-355, February 1999

[Qi00] J.Qi, R.M.Leahy, *Resolution and Noise Properties of MAP Reconstruction for Fully 3D PET*, IEEE Transactions on Medical Imaging, May 2000

[Ram71] G.N.Ramachandian, A.V.Lakshminarayanan, *Three-dimensional Reconstruction from Radiographs and Electron Micrographs: Application of Convolution instead of Fourier Transform*, Proceedings of the National Academy of Sciences, USA, Vol. 68, p.2236, 1971

[Rad17] J.Radon, *Über die Bestimmung von Funktionen durch ihre Integralwerte langs gewisser Manningsfaltigkeiten*, Berichte Sächsische Akadamie der Wissenschaften, Leipzig, Math.-Phys. Kl., 69, pp. 262-277, 1917. Translation by Parks P.C. in IEEE Transactions on Medical Imaging, MI-Vol. 5, p.170, 1986

[Raj92] N.Rajeevan, K.Rajgopal, G.Krishna, *Vector-extrapolated fast Maximum Likelihood Estimation Algorithms for Emission Tomography*, IEEE Transactions on Medical Imaging, Vol. 11, No. 1, pp. 9-20, 1992

[Rau91] S.J.Raudys, A.K.Jain, *Small Sample Size Effects in Statistical Pattern Recongnition: Recommendations for Practitioners*, IEEE Transactions on Pattern Analysis and Machine Intelligence, Vol. 13, No. 3, pp. 252-264, March 1991

[Rol92] J.P.Rolland, H.H.Barrett, *Effect of Random Background Inhomogeneity on Observer Detection Performance*, Journal of the Optical Society of America, Vol. A9, pp. 649-658, 1992

[Sau93] K.Sauer, C.Bouman, *A Local Update Strategy for Iterative Reconstruction from Projections*, IEEE Transactions on Signal Processing, Vol. 41, No. 2, pp. 534-548, 1993

[Sch94] R.B.Schwartz, A.L.Komaroff, B.M.Garada, M.Gleit, T.Doolittle, D.Bates, R.Vasile, B.Holman, *SPECT Imaging of the Brain: Comparison of Findings in Patients with Chronic Fatigue Syndrome, AIDS Dementia Complex and Major Unipolar Depression*, American Journal of Roentgenology, Vol. 162, pp. 943-951, 1994

[She82] L.Shepp, Y.Vardi, *Maximum Likelihood Reconstruction for Emission Tomography*, IEEE Transactions on Medical Imaging, Vol. 1, No. 2, pp. 113-122, 1982

[Sil90], B.Silverman, M.Jones, J.Wilson, D.Nychka, *A Smoothed EM Approach to Indirect Estimation Problems with Particular Reference to Stereology and Emission Tomography*, Journal of Royal Statistical Society, Ser. B, Vol. 52, No. 2, pp. 271-324, 1990

[Smi92] M.Smith, C.Floyd, R.Jaszczak, E.Coleman, *Three-Dimensional Photon Detection Kernels and their Application to SPECT Reconstruction*, Physics in Medicine and Biology, Vol. 37, pp. 605-622, 1992

[Sol76] *The X-ray Transform*, Journal of Mathematical Analysis and Applications Vol. 56, p.61, 1976

[Sta75] S.J.Starr, C.E.Metz, L.B.Lusted, D.J.Goodenough, *Visual Detection and Localization of Radiographic Images*, Radiology, Vol. 116, pp. 533-538, 1975

[Swe96] R.G.Swensson, *Unified Measurement of Observer Performance in Detecting and Localizing Target Objects on Images*, Medical Physics, Vol. 23, pp. 1709-1725, 1996

[Tik63a] A.N.Tikhonov, *Regularization of incorrectly posed problems*, Soviet Math. Dokl., Vol. 4, pp. 1624-1627, 1963

[Tik63b] A.N.Tikhonov, *Solution of Incorrectly Formulated Problems and the Regularization Method*, Soviet Math.Dokl, Vol. 4, pp. 1035-1038, 1963

[Tik77] A.N.Tikhonov, V.Y.Arsenin, *Solutions of ill-posed problems*, Washington, DC: V.H. Winston & Sons, 1977.

[Tow92] D.W.Townsend, M.Defrise, *Image Reconstruction Methods in Positron Tomography*, Lectures given in the Academic Training Programme on CERN, Physics and Mathematics for Medical Imaging, 1992 93

[Tsui91] B.M.W.Tsui, X.D.Zhao, E.Frey, G.Gullberg, *Comparison between ML-EM and WLS-CG Algorithms for SPECT Image Reconstruction*, IEEE Transactions on Nuclear Science, Vol. 38, pp. 1766-1772, 1991

[Tsui94] B.M.W.Tsui, E.C.Frey, X.Zhao, D.S.Lalush, R.E.Johnston, W.H.McCartney, *The Importance and Implementation of Accurate 3D Compensation Methods for Quantitative SPECT*, Physics in Medicine and Biology, Vol. 39, pp. 509-530, 1994

[Van87] A.van der Sluis, H.A.van der Vorst, *Numerical Solution of Large, Sparse Linear Algebraic Systems Arising from Tomographic Problems*, Seismic Tomography, ed. G.Nolet (Dordrecht: Reidel), pp. 49-83, 1987

[Vek87] E.Veklerov, J.Llacer, *Stopping Rule for the MLE algorithm Based on Statistical Hypothesis Testing*, IEEE Transactions on Medical Imaging, Vol. 6, No. 4, pp. 313-319, 1987

[Wal97] J.W.Wallis and T.R.Miller, *An Optimal Rotator for Iterative Reconstruction*, IEEE Trans.Med.Imaging, Vol. 16, pp. 118-23, 1997

[Wat95] C.C.Watson, D.Newport, M.E.Casey, *A Single Scatter Simulation Technique for Scatter Correction in 3D PET*, International Meeting on Fully Three Dimensional Image Reconstruction in Radiology and Nuclear Medicine, Aix-les Bain, France, 1995

[Yao92] J.Yao, H.H.Barrett, *Predicting Human Performance by a Channelized Hotelling Observer Model*, Mathematical Method in Medical Imaging, SPIE, Vol. 1768, pp. 161-168, 1992

[Yav96] M.Yavuz, J.A.Fessler, *Objective Functions for Tomographic Reconstruction from Randoms-Precorrected PET Scans*, Proceedings of IEEE Nuclear Science and Medical Imaging Conference, Vol. 2, pp. 1067-1071, 1996

[You82] D.C.Youla, H.Webb, *Image Restoration by the Method of Convex Projection: Part1-Theory*, IEEE Transactions on Medical Imaging, Vol. 1, pp. 81-94, 1982

[Zen91] G.L.Zeng, G.T.Gullberg, *Frequency Domain Implementation of the Three-Dimensional Geometric Point Response Function Correction in SPECT Imaging*, Conference Record 1991, Nuclear Science Symposium in Medical Imaging Conference, (Piscataway, NJ: IEEE), pp. 1943-1947

[Zho97] Z.Zhou, R.M.Leahy, J.Qi, *Approximate Maximum Likelihood Hyperparameter Estimation for Gibbs Priors*, IEEE Transactions on Image Processing, Vol. 6, No. 6, pp. 844-861, June 1997